

# Nanoscale Strain Characterisation of Modern Microelectronic Devices

---

A thesis submitted to the faculty of Science, Agriculture and Engineering for the degree of Doctor of Philosophy

Lisa Sanderson

October 2011



**Newcastle**  
University

School of Chemical Engineering and  
Advanced Materials  
Newcastle upon Tyne  
United Kingdom

## **Abstract**

Sources of stress and strain in modern microelectronics can be either beneficial to the electrical performance or detrimental to the mechanical integrity and ultimately lifetime of the device.

Strain engineering is commonplace in state-of-the-art device fabrication as a means to boost performance in the face of device scaling limitation. The strain present in the device is directly related to the improvement factor and as such precise measurements and good understanding are of utmost importance due to the many thermal processing steps that can induce or cause relaxation of the strain. Front-end-of-line (FEOL) strain characterisation is becoming increasingly challenging due to the small volumes of material and nanoscale feature sizes being analysed.

In this work, an extensive survey of strain characterisation techniques was undertaken. Narrow sSOI stripes were profiled using conventional Raman spectroscopy. Unlike with previous studies, it was shown that it is possible to achieve nanoscale measurements using current techniques. This study was supported by ANSYS FE simulation.

The review of the literature briefly investigates the possibility of EBSD as a strain measurement tool. It is possible to calculate not just an absolute strain value as achievable with Raman spectroscopy, but the strain tensor. However, this is a difficult and complex process and not necessary for use in industry. This study proposes the possibility of a more simple method that would provide a good calibration technique to confirm Raman measurements.

SERS and TERS are explored in detail as the most promising techniques when dealing with device scaling. Currently, SERS is a destructive technique not suitable for use in a highly cost driven industry such as semiconductor manufacturing. While it theoretically gives improved surface selectivity over conventional Raman spectroscopy, there is no improvement to the xy spatial resolution. With Si and SiGe samples, this study concludes there is also often no surface selectivity with either technique and the mechanisms behind the enhancement are not understood to the point of being able to implement the techniques in a process line. However, where a non-destructive technique

is desired, outlined in this study is a method of achieving the SERS effect without sacrificing the sample.

Aggressive scaling has forced the dimensions of the interconnecting wires that give the devices functionality to the deep submicron range. Copper, Cu has been introduced as a replacement to the traditionally used aluminium, Al because of its superior electrical and mechanical properties and scalability. However, as these wires begin to approach the dimensions of thin foils, the microtexture of the wires becomes significantly different from their bulk counterparts. This can affect the mechanical integrity of the interconnects and this has an impact on the reliability of the device. Failure mechanisms such as blistering, cracking and peeling caused by stress and strain are not uncommon and traditional methods of characterising residual stress in the thin films is no longer applicable to these narrow wires.

The mechanical properties and microtexture of thin copper films annealed at temperatures comparative to those found in device manufacturing were characterised in some detail. EBSD was used to determine the grain size and structure of the films before nanoindentation confirmed properties such as hardness and elastic modulus. These results pave the way for investigation of strain applied along deep-submicron interconnects to lead to further understanding of what causes failure mechanisms from interconnecting wires.

## **Acknowledgements**

The work of this thesis was carried out at Newcastle University and I owe a great deal of thanks to many people within this institution. I would like to take this opportunity to show my appreciation to those people who helped, encouraged and pushed me along this journey.

I am grateful to my supervisors Steve Bull and Sarah Olsen. To be able to work with someone with the immense technical experience and knowledge that Steve possesses has been an honour. His guidance and support have been second to none for the past four years and for that I am grateful. The encouragement I have received from Sarah from the very beginning of this project has been a great help. Without her, I would have never considered this to be something I could achieve and I will always appreciate what she has done for me.

Aside from my supervisors, there are several academic and non-academic staff members at Newcastle who have helped me along the way. First and foremost I'd like to thank Adrian Oila. He was never too busy to help and has been a great source of knowledge and I appreciate the many hours he sat with me in front of the SEM. Thanks also go out to Pauline Carrick, Rob Dixon and Paul Sterling for the technical support and immense patience they have shown towards me. Wayne Twigger, of Horiba Jobin Yvon has always been only a phone call away to assist with the many technical problems with the Raman microscope. I enjoyed the learning experience of it and I am grateful for the time he put aside to further my understanding.

Finally, I cannot express enough the gratitude I feel towards my parents and Michael. They have always supported me and believed in me. Thank you for never allowing me to give up.

For my Grandad Alf

## Table of Contents

Chapter 1. Introduction .....	1
1.1. Motivation for the Study .....	1
1.2. General Background.....	2
1.3. Strained Silicon Technology .....	4
1.3.1. Benefits of strain in devices .....	7
1.3.2. Introduction to strain measurement in Silicon .....	8
1.4. Copper Interconnects.....	11
1.4.1. Stress and Strain in copper interconnects .....	12
1.4.2. Deposition and Interconnect Patterning .....	13
1.5. Scope of the Thesis.....	15
1.6. Summary .....	16
Chapter 2. Techniques .....	17
2.1. Introduction .....	17
2.2. Background to Raman Spectroscopy.....	17
2.2.1. The Raman Effect .....	19
2.2.2. Raman Scattering .....	20
2.2.3. Rotational and Vibrational Raman Scattering.....	22
2.2.4. Polarizability and selection rules .....	22
2.2.5. Strain Analysis Using Raman Spectroscopy .....	24
2.2.5.1. Stress measurement .....	24
2.2.6. Spatial and Depth Resolution.....	26
2.3. Surface Enhanced Raman Spectroscopy and Tip-Enhanced Raman Spectroscopy .....	27
2.3.1. Surface Enhanced Raman Spectroscopy (SERS).....	28
2.3.2. Tip Enhanced Raman Spectroscopy (TERS).....	28

2.3.3.	The Effect of a metallised tip .....	30
2.3.3.1.	Localised Surface Plasmons .....	31
2.3.3.2.	Electromagnetic Enhancement .....	32
2.3.4.	Tip fabrication .....	35
2.4.	Recent Developments in Raman Spectroscopy .....	37
2.5.	Electron Backscatter Diffraction .....	38
2.5.1.	Background .....	39
2.5.2.	Strain Analysis Using EBSD .....	39
2.6.	Summary .....	41
Chapter 3.	Instrumentation .....	42
3.1.	Introduction .....	42
3.2.	Raman Spectroscopy Instrumentation .....	42
3.2.1.	LabRAM HR800 setup and operation .....	42
3.2.1.	Confocal Microscope .....	44
3.2.2.	Excitation Source and Diffraction Grating .....	45
3.2.3.	TERS setup .....	46
3.3.	Electron Backscatter Diffraction .....	47
3.4.	Summary .....	49
Chapter 4.	Raman Calibration .....	50
4.1.	Introduction .....	50
4.2.	Raman Spectroscopy for Strain Analysis .....	50
4.3.	Silicon Reference Spectrum .....	51
4.3.1.	Si <sub>1-x</sub> Ge <sub>x</sub> Spectrum.....	52
4.4.	Calibration Curve: Theoretical, Experimental and from Literature .....	54
4.4.1.	Theoretical and Literature Calibration Curve .....	56
4.5.	Effect of Heat and Laser Power.....	62
4.6.	Verification of Raman results.....	69

4.6. Summary .....	71
Chapter 5. Strained Silicon on Insulator (sSOI) stripes.....	72
5.1. Introduction .....	72
5.2. Results .....	73
5.2.1. 600 $\mu\text{m}$ sSOI stripes.....	73
5.2.2. 20 $\mu\text{m}$ sSOI Stripes .....	80
5.2.2.1. Visible Laser.....	81
5.2.2.2. UV Laser.....	83
5.3. Summary .....	87
Chapter 6. Surface and Tip Enhanced Raman Spectroscopy.....	88
6.1. Introduction .....	88
6.2. Nanoparticle fabrication.....	89
6.3. Non-destructive SERS.....	90
6.4. SERS experiment.....	91
6.4.1. Silicon .....	92
6.4.2. D02: 12 nm sSi.....	93
6.4.3. D04: 30 nm sSi.....	94
6.4.4. D05: 80 nm sSi.....	95
6.5. Graded Ge .....	97
6.6. TERS .....	99
6.7. Summary .....	103
Chapter 7. Mechanical assessment of copper metallisation at high spatial resolution	
104	
7.1. Introduction .....	104
7.2. EBSD Results .....	106
7.2.1. No Anneal .....	107
7.2.2. 100°C 60 Minute Anneal .....	109

7.2.3.	180°C 30 Second Anneal .....	110
7.2.4.	350°C 60 Second Anneal .....	111
7.2.5.	EBSD Discussion .....	112
7.3.	Nanoindentation Results.....	113
7.3.1.	Nanoindentation Discussion .....	118
7.4.	Summary .....	119
Chapter 8.	Conclusions and future remarks.....	120
Appendix I.	.....	123
References	.....	124

## List of Figures

**Figure 1.1.** Moore's Law depicted in graphical form. Gordon Moore predicted that the number of transistors per chip would double every 18-24 months.

**Figure 1.2.** Typical MOSFET structure, currently being fabricated with a channel length in the order of tens of nanometres. Strained silicon is usually introduced to the channel of the transistor.

**Figure 1.3.** Unit cell of a diamond structure.

**Figure 1.4.** A Homogeneous strain and B Strain relaxation caused by dislocations leading to a lattice mismatch between the SiGe and strained Si cap layer grown epitaxially on top of VS, thus leading to tensile strain.

**Figure 1.5.** Typical peak positions of Si-Si bonds in SiGe and the nearly hidden strained Si cap layer.

**Figure 1.6.** Process flow of a typical Damascene copper deposition procedure.

**Figure 2.1.** Depiction of the Rayleigh (elastic) and Raman (inelastic) Stokes and Anti-Stokes Scattering processes.  $m$  is the lowest vibrational state and the states above are of increasing energy. Photons incident on a sample can interact with it in several ways, they can be scattered elastically, Rayleigh scattering or inelastically, Raman Scattering.  $m$  and  $n$  represent vibrational energy states of the molecule. The virtual states are determined by the frequency of the incident radiation.

**Figure 2.2.** Feynman diagram and energy levels of the Stokes scattering process. Incident photon of frequency  $\omega_i$  interacts with an electron in a molecule changing its energy from ground state to state  $|l\rangle$ . This creates a phonon with frequency  $\omega_j$ . Electron-phonon interaction excites the electron to a state  $|m\rangle$  and a photon of frequency  $\omega_s$  is emitted.

**Figure 2.3.** TERS setup on a  $\epsilon$ -Si/SiGe sample. The laser illuminates the metallised AFM tip creating a large electric field in the area directly underneath the tip apex. This has the effect of creating a surface selective enhancement with a significantly improved spatial resolution.

**Figure 2.4.** Kikuchi bands of A) unstrained and B) strained silicon.

**Figure 3.1.** LabRAM HR800 .

**Figure 3.2.** Schematic of typical LabRAM HR800 set up.

**Figure 3.3.** In depth schematic of the optical path in the LabRAM HR800. The schematic shows the path of both the tuneable visible laser and the argon ion UV laser.

**Figure 3.4.** Depiction of the lens in a confocal microscope.

**Figure 3.5.** Combined AFM/Raman TERS system consisting of LabRAM HR800 coupled with a Park Systems AFM [Horiba Jobin Yvon, 2011]

**Figure 3.6.** Depiction of off-axis coupling where the Raman microscope objective is set at an angle such that there are no effects from the AFM cantilever. The Raman microscope is still in back scattering mode [Horiba Jobin Yvon, 2011]

**Figure 3.7.** Main body of instrument depicting polariser mount. The polariser is used to block any far-field signal ensuring all the collected signal is that which is enhanced due to the presence of the AFM tip.

**Figure 3.8.** Philips XL40 ESEM.

**Figure 3.9.** Schematic showing the principle components of EBSD.

**Figure 4.1.** Schematic of samples used in this investigation. Samples had varying Ge composition, 0 – 30%. Devices were etched from the sample surface prior to measurement .

**Figure 4.2.** Silicon reference spectrum. Single crystal silicon has a characteristic peak of  $520.7\text{ cm}^{-1}$ . However, typical values lie between  $520 - 521\text{ cm}^{-1}$ .

**Figure 4.3.** Depicts the difference in peak position between single crystal silicon and  $\text{Si}_{0.7}\text{Ge}_{0.3}$  as being approximately  $18\text{cm}^{-1}$ . This difference allows an estimation of the Ge content of a sample using the peak position as a reference.

**Figure 4.4.** Typical peaks in a strained silicon sample with the structure depicted in figure 4.1. The strained silicon cap layer manifests itself as a small, difficult to analyse shoulder on the high wave number side of the much higher intensity Si in SiGe peak.

The sample used to obtain the above spectrum is  $\text{Si}_{0.7}\text{Ge}_{0.3}$ . The excitation source is a 457 nm laser at approximately 1.57 mW power.

**Figure 4.5.** Strained Si cap peak position and the Si-Si in SiGe bonds versus Ge Content for 514.5nm (green) laser at 1.1mW power.

**Figure 4.5.** Strained Si cap peak position and the Si-Si in SiGe bonds versus Ge Content for 514.5nm (green) laser at 1.1mW power.

**Figure 4.6.** Strained Si cap peak position and the Si-Si in SiGe bonds versus Ge Content for 457.9nm (blue) laser at 1.57mW power.

**Figure 4.7.** Strained Si cap peak position versus Ge content for 364 nm (UV) laser.

**Figure 4.8.** Theoretical and experimental peak positions for a fully relaxed SiGe sample.

**Figure 4.9.** Raman peak position versus Ge composition comparing NCL experimental data with data found in literature using similar samples of fully relaxed SiGe.

**Figure 4.10.** Data points from Si-Si, Si-Ge and Ge-Ge bonds in relaxed SiGe layers.

**Figure 4.11.** Peak position versus Germanium content for samples with residual strain in the SiGe layer.

**Figure 4.12.** Effect of Ge composition on peak position and intensity.

**Figure 4.13.** Schematic showing the typical penetration depths of some commonly used excitation lines. The blue arrows represent a UV source, with a wavelength of around 364 nm, and a penetration depth of only a few nanometres. A green laser, with wavelength of 514 nm will have a penetration depth of up to a micron, and a red laser of wavelength 633 nm will have the largest penetration depth in Si and Ge of much more than a micron, and up to 3  $\mu\text{m}$  depending on Ge content.

**Figure 4.14.** The intensity of a spectrum is directly affected by the power of the excitation source. Higher powers give a significantly higher intensity, however, can have a detrimental effect on the information gathered. Higher powers will drown out the peaks of much less intense bonds such as those from a strained silicon cap layer. More

power also means more heat, and heat can affect the peak position giving a false value for strain.

**Figure 4.15.** UV (364 nm) laser excitation source, varying powers shows a significant difference in peak position due to the heating affects at the sample surface. The small penetration depth coupled with the lower thermal conductivity of SiGe means that the heat is concentrated over a smaller area and not dissipated as well throughout the sample as the germanium content increases. The peak position shifts to a lower wavenumber as the heat is having the same effect as higher tensile strain in the sample.

**Figure 4.16.** 457 nm exciting laser gives spectra with a difficult to analyse strained Si peak. The different in values only really manifests itself at higher Ge content and it could be argued there is no significant difference between the peak positions measured for either high or low powers.

**Figure 4.17.** 514 nm exciting laser. The different in values only really manifests itself at higher Ge content and it could be argued there is no significant difference between the peak positions measured for either high or low powers.

**Figure 4.18.** 457 nm exciting laser gives spectra with a difficult to analyse strained Si peak. The different in values only really manifests itself at higher Ge content and it could be argued there is no significant difference between the peak positions measured for either high or low powers.

**Figure 4.19.** 514 nm exciting laser gives spectra with a difficult to analyse strained Si peak. The different in values only really manifests itself at higher Ge content and it could be argued there is no significant difference between the peak positions measured for either high or low powers.

**Figure 4.20.** Unstrained Si sample with Kikuchi bands of width  $x_1$ .

**Figure 4.21.** Strained Si sample with Kikuchi bands of width  $x_2$ .

**Figure 5.1.** Schematic depicting the process flow for achieving a silicon on insulator (SOI) wafer. The process for strained SOI is similar and involves bonding a thermally oxidised wafer to a silicon wafer with a strained silicon epitaxial layer.

**Figure 5.2.** Schematic of the initial sample, 600 x 600  $\mu\text{m}$  sSOI stripes of varying widths. Each set of stripes had 300 nm pitch, were 25 nm of equivalent 20% Ge content on 140 nm of buried oxide.

**Figure 5.3.** SEM image of the sSOI stripes. The 25 nm stripes are not shown due to significant damage across the centre of the box. These stripes were still analysed, though are thought to show significant relaxation due to the damage.

**Figure 5.3.** 514 nm laser source, 2.4  $\mu\text{m}$  line scan with 5 nm step size. Power was held at 0.7 mW and exposure time per measurement was 2 seconds.

**Figure 5.4.** Graph depicting strain relaxation as stripe width decreases. Damage on the 25 nm stripes has contributed somewhat to a lower than expected strain, however, the graph still indicates the relaxation isn't linear.

**Figure 5.5.** ANSYS simulations show almost full strain relaxation at the centre of the stripe for all widths.

**Figure 5.6.** ANSYS simulation of 60 nm sSOI stripe.

**Figure 5.7.** Schematic of sSOI stripes with varying widths. A biaxially strained pad is present at each end of the stripes.

**Figure 5.8.** SEM image of 70 nm wide, 20  $\mu\text{m}$  long sSOI stripes with biaxial strained pad at each end.

**Figure 5.9.** 70 nm stripe profile taken using 514 nm laser at 0.7 mW power.

**Figure 5.10.** Stripe profile of 70 nm wide stripe using UV laser held at half power and a 15 second exposure time per measurement along the scan. Scan step size was 5 nm.

**Figure 5.11.** LabSpec screenshot of each spectrum overlaid. At the high wavenumber side of the spectrum there is little variation, however, there is a significant width variation at the low wavenumber side caused by the sSOI stripe.

**Figure 5.12.** LabSpec screenshot of the widest spectrum overlaid on an unstrained Si spectrum. The high wavenumber side of the spectra are identical. The difference in width on the low wavenumber side is down to the presence of a peak from the sSOI stripe.

**Figure 5.13.** LabSpec screenshot of the difference spectrum obtained from subtracting the Si spectrum from the wider sSOI spectrum.

**Figure 5.14.** Profile of the 70 nm sSOI stripe. The UV laser was held at maximum power with a long exposure time to ensure maximum intensity from the  $\epsilon$ -Si and hence the most accurate strain values are obtained.

**Figure 6.1.** SEM analysis of gold nanoparticles. The particles are contained within the raised areas, however, the SEM image could not be resolved enough to focus on individual particles or clumps of particles. TEM would be required for this analysis.

**Figure 6.2.** EDAX spectrum confirms the presence of small quantities of Au.

**Figure 6.3.** Thin C-growth SRB: D02: 12 nm strained Si; D04: 30 nm strained Si; D05: 80 nm strained Si provided by Sematech.

**Figure 6.4.** Plain silicon spectra taken from a sample coated in Au nanoparticles compared with a sample without. The consistent, reproducible enhancement with the presence of Au NPs shows an increase in amplitude of  $\sim 260\%$ . The formation and location of the NPs seemed to make little difference to whether an enhancement was achieved.

**Figure 6.5.** Sample D02 was a 4-layer  $\text{Si}_{0.8}\text{Ge}_{0.2}$  virtual substrate with a fully strained 12 nm  $\epsilon$ -Si cap layer. Samples were provided by Sematech. While there is no overall enhancement to the signal amplitude in this case, it can be argued that the small  $\epsilon$ -Si peak manifests itself as a more obvious peak rather than a shoulder. However, this spectrum was not reproducible on every measurement.

**Figure 6.6.** Sample D03 was a 4-layer  $\text{Si}_{0.8}\text{Ge}_{0.2}$  virtual substrate with a 30 nm  $\epsilon$ -Si cap layer. Samples were provided by Sematech. Once again, there is no overall enhancement to the signal amplitude. The relative intensities of the  $\epsilon$ -Si peak to the Si in SiGe and Si peaks shows that there was a small ( $\sim 5\%$ ) enhancement of this peak, indicating that with a slightly thicker cap layer, surface selectivity is beginning to become apparent.

**Figure 6.7.** Sample D05 was a 4-layer  $\text{Si}_{0.8}\text{Ge}_{0.2}$  virtual substrate with the thickest  $\epsilon$ -Si cap layer of the samples at 80 nm. Samples were provided by Sematech. As per the previous samples, there is no overall enhancement to the signal amplitude. The relative

intensities of the  $\epsilon$ -Si peak to the Si in SiGe and Si peaks show a much more apparent surface selectivity. While it was possible to achieve an enhancement with this sample, it was not always reproducible, however, it was much more so than with the previous samples.

**Figure 6.8.** A LabSpec screen shot of a spectrum taken using the D05 sample described previously shows it is possible to get total surface selectivity using this SERS technique. Most spectra, however, were much more like that shown in figure 6.7. A slight peak shift in the Si and Si in SiGe peaks was noted.

**Figure 6.9.** A LabSpec screenshot of the 10% Ge spectrum shows a relatively obvious  $\epsilon$ -Si peak when compared to the conventional Raman spectroscopy spectrum.

**Figure 6.10.** A LabSpec screenshot of the 30% Ge shows a definite  $\epsilon$ -Si peak instead of the small shoulder usually observed with conventional Raman spectroscopy.

**Figure 6.11.** The initial TERS spectrum taken with the set up described in chapter 3 using a sample provided by Imperial College. An enhancement from the thick SiGe virtual substrate is noted, however, there is no apparent surface selectivity.

**Figure 6.12.** Plain silicon, near-field comparison with far-field. As with SERS it is significantly easier to reproduce this enhancement using a single crystal sample as opposed to the multi-layer SiGe samples.

**Figure 6.13.** A LabSpec screenshot showing a comparison of spectra between near-field, far-field spectra and with a depolarised sample.

**Figure 7.1.** Copper is a highly isotropic material. This diagram shows the change in elastic modulus with a change in crystallographic orientation.

**Figure 7.2.** TEM image of 100 nm wide Cu interconnects. The grain structure in these narrow interconnects where grain size is often much wider than the width of the wire is approaching what is known as a bamboo structure.

**Figure 7.3.** Cu film as deposited with no anneal. A series of four  $5\ \mu\text{m} \times 5\ \mu\text{m}$  EBSD maps were taken and show a mix of large and small grain size characteristic of an as deposited sample.

**Figure 7.4.** Inverse pole figure showing the crystallographic orientation of the Cu grains on the sample with no anneal.

**Figure 7.5.** Cu film annealed at 100°C for 60 minutes. A series of four 5 µm x 5 µm EBSD maps were taken and showing some larger grains beginning to grow.

**Figure 7.6.** Inverse pole figure showing the crystallographic orientation of the Cu grains on the sample annealed at 100°C for 60 minutes.

**Figure 7.7.** Cu film annealed at 180°C for 30 seconds. A series of four 5 µm x 5 µm EBSD maps were taken and showing larger grain sizes.

**Figure 7.8.** Inverse pole figure showing the crystallographic orientation of the Cu grains on the sample annealed at 180°C for 30 seconds.

**Figure 7.9.** Cu film annealed at 350°C for 60 seconds. A series of four 5 µm x 5 µm EBSD maps were taken and showing some recrystallisation is beginning to occur.

**Figure 7.10.** Inverse pole figure showing the crystallographic orientation of the Cu grains on the sample annealed at 350°C for 60 seconds.

**Figure 7.11.** (111) grains grow at the expense of fine-grained material for low temperature anneals. The anneal at 350°C generates some recrystallisation with a higher percentage of fine grains and a strong (111) texture.

**Figure 7.12.** Schematic of a Berkovich tip.

**Figure 7.13.** Multicycling load versus time experimental set up for a load/partial-unload cycle .

**Figure 7.14.** Single cycle load versus time experimental set up.

**Figure 7.15.** Single versus multicycling data. At contact depths between approximately 60 – 100 nm, multicycling data agrees with single cycle, implying this is the optimum depth for reliable data.

**Figure 7.16.** Contact depth vs. pile up width for the sample with no anneal. Pile up width increases linearly with contact depth, this behaviour was observed with all four samples.

**Figure 7.17.** Theoretical calculations of Young's modulus at different crystallographic orientations on single crystal, bulk silicon.

**Figure 7.18.** Elastic modulus vs. contact depth. The no anneal sample shows (110) behaviour, 180°C and 100°C are exhibiting (100) type behaviour and 350°C exhibits (111) behaviour. This data largely agrees with the EBSD data.

**Figure 7.19.** Hardness vs. contact depth. 100°C annealed sample displays a higher than expected hardness value likely due to the indent being carried out on a small grain. The hardness values at high contact depths converge due to the effect from pile up.

## List of Tables

**Table 4.1.** Theoretical strain values for  $\text{Si}_{1-x}\text{Ge}_x$  where x is 0 – 100 %.

**Table 4.2.** Effect of Germanium content on laser penetration depth.

**Table 7.1.** Crystallographic orientation of the sample with no anneal

**Table 7.2.** Crystallographic orientation of the sample annealed at 100°C for 60 minutes.

**Table 7.3.** Crystallographic orientation of the sample annealed at 180°C for 30 seconds.

**Table 7.4.** Crystallographic orientation of the sample annealed at 350°C for 60 seconds.

The orientation results from the final map are omitted due to the significant drift seen.

## **List of symbols and abbreviations**

AFM	Atomic force microscopy/microscope
BEOL	Back-end-of-line
CCD	Charge coupled device
CVD	Chemical vapour deposition
EBSD	Electron backscatter diffraction
EBSP	Electron backscatter pattern
EDX	Energy dispersive x-ray analysis
ESEM	Environmental scanning electron microscopy/microscope
FCC	Face centred cubic
FDTD	Finite difference time domain
FE	Finite element
FEGSEM	Field emission gun scanning electron microscopy/microscope
FEOL	Front-end-of-line
FTIR	Fourier transform infrared spectroscopy
IC	Integrated circuit
IPF	Inverse pole figure
LSP	Local surface plasmon
MBE	Molecular beam epitaxy
MOSFET	Metal oxide semiconductor field effect transistor
NA	Numerical aperture
NIR	Near-infrared
NP	Nanoparticle

PVD	Physical vapour deposition
RAFM	Raman atomic force microscope/microscopy
RIE	Reactive ion etching
SEM	Scanning electron microscope
SERS	Surface-enhanced Raman spectroscopy/scattering
SiGe	Silicon germanium
SIMS	Secondary ion mass spectroscopy
SPP	Surface plasmon polariton
SPR	Surface plasmon resonance
sSOI	Strained silicon on insulator
STM	Scanning tunnelling microscope/microscopy
TEM	Transmission electron microscope/microscopy
TERS	Tip-enhanced Raman spectroscopy/scattering
ULSI	Ultra large scale integration
UV TERS	Ultraviolet tip-enhanced Raman spectroscopy
VLSI	Very large scale integration
VS	Virtual substrate
XRD	X-ray diffraction
a	Lattice constant
d	Laser spot diameter
E	Young's modulus
$E_0$	Applied electric field

$E_{p/q}$	Energy states
$E_r$	Electric field at distance $r$
$f_m$	Lattice mismatch parameter
$h$	Planck's constant
$h_c$	Critical thickness
$K$	Refractive index
$m$	Electron mass
$m$	Vibrational energy state
$n$	Electron density number
$n$	Vibrational energy state
$p, q, s$	Phonon deformation potentials
$P$	Dipole moment
$S_{ij}$	Elastic constant
$\alpha$	Polarizability
$\alpha$	Absorption coefficient
$\Delta\omega$	Raman frequency
$\varepsilon$	Strain
$\varepsilon_0$	Dielectric constant
$\theta$	Angle of applied electric field
$\nu$	Frequency
$\nu$	Poisson's ratio
$\nu_L$	Frequency of incident radiation

$\sigma$	Strain
$\omega_r$	Frequency of scattered radiation
$\omega_0$	Frequency of incident radiation
$\omega_p$	Plasma frequency
$\omega_{sp}$	Surface plasma frequency

# **Chapter 1. Introduction**

## **1.1. Motivation for the Study**

Several years of aggressive device scaling in the semiconductor industry has come about due to the desire to realise Moore's Law for as long as possible [Intel Corporation, 2008]. Moore's Law states that the number of transistors per chip will double every 18-24 months. In recent years, in order to uphold or improve the cost per die unit area, it has been necessary to make devices smaller [Moore, 1965]. The current gate length for state of the art devices is in the order of tens of nanometres [Intel Corporation, 2011, ITRS, 2011]. State of the art devices carry with them several new challenges. Smaller devices have given rise to new materials being introduced and several characteristics, both electrical and of the materials themselves, require understanding and close monitoring throughout the fabrication process to ensure device performance and reliability are maintained. Consistent and precise characterisation is required in order to gain an improved understanding of devices and interactions within various layers of the device.

It is widely accepted that the properties of materials can alter at the nanoscale [Masuda-Jundo, 2009]. It is imperative to have a full understanding of materials used throughout the device fabrication process before such devices go to full-scale production. Nanoscale materials have many benefits over their bulk material counterparts, however, will also present several new challenges. Material and surface scientists interested in deep sub-micron characteristics have a range of tools available to them including TEM, XRD, SEM, EBSD, FTIR, AFM and Raman spectroscopy. Many of these techniques are destructive in nature. Such techniques are unsuitable for use within a production line in the semiconductor industry, and would only be used as a failure analysis tool. In a highly cost driven environment such as a semiconductor fabrication facility, any additional monitoring or measurement techniques must not create additional costs and needs to be quick and simple to implement.

Much of this project is concerned with the additional sources of stress and strain in modern microelectronic devices. Copper, Cu and strained silicon,  $\epsilon$ -Si are now extensively used in the semiconductor industry. Previously, devices have been fabricated on silicon substrates with aluminium, Al as an interconnect material [ITRS,

2011]. However, since devices have been further scaled, these newer materials have proven to improve device performance while showing good scalability [Vereecken, 2005].

In modern microelectronics there are many sources of stress and strain. Some strain is beneficial to their operation while some is detrimental. Recent semiconductor processing has seen the introduction of  $\epsilon$ -Si in devices, where strain can be introduced either globally i.e. throughout the whole substrate, or locally i.e. either process induced strain or substrate patterning techniques such as with strained silicon on insulator (sSOI) stripes [Reiche, 2008]. In this case, strain is beneficial due to its effect on the charge carrier transport mechanisms [Collins, 2003, Olsen, 2005]. The metallisation that forms the device interconnects giving them functionality is also subject to various stresses and strains caused by deposition, microstructure, thermal processing and load. Here, these stresses potentially have an unfavourable effect on the lifetime of the devices. During processing there are problems from metallisation buckling or peeling, delaminating or blistering. Post-processing comes reliability issues such as cracking, effectively short circuiting the device leading to early failure [Wolf, 2000, Wilson, 2009]. In either case, beneficial or detrimental, a full understanding of the stresses and strains involved is vital in today's competitive semiconductor industry, which means effective characterisation and measurement tools must be employed.

Front-end-of-line (FEOL) and back-end-of-line (BEOL) processing will be referred to. FEOL is everything from wafer fabrication to passivation layers. BEOL is everything from the first passivation layer to metallisation and packaging. In this instance, strained silicon technology will be referred to as FEOL and copper metallisation is BEOL. This thesis will survey currently available techniques as well as new techniques still in their infancy for applications within the semiconductor industry. Through a combination of experimental work and simulations, the capabilities and limitations of these techniques as industrial applications will be explored in some detail.

## **1.2. General Background**

Gordon Moore, the founder of the Intel Corporation predicted in 1965 that the number of transistors on a chip would double every 18-24 months [Intel Corporation, 2008]. This is now termed Moore's law and predicts that the performance of an integrated

circuit would double every couple of years, depicted in figure 1.1. Moore discussed not just the transistor density achievable but about the density of transistors per chip at the lowest possible cost. As more transistors per chip are realised, the cost per transistor falls, however, the risk of a chip not working due to defect is also increased, hence the importance of keeping costs to a minimum. It is this cost density that has driven the aggressive scaling of devices [Moore, 1965]. Aside from transistor density increasing at an almost exponential rate, the cost and speed of integrated circuits can be shown to follow a similar pattern [Intel Corporation, 2008].

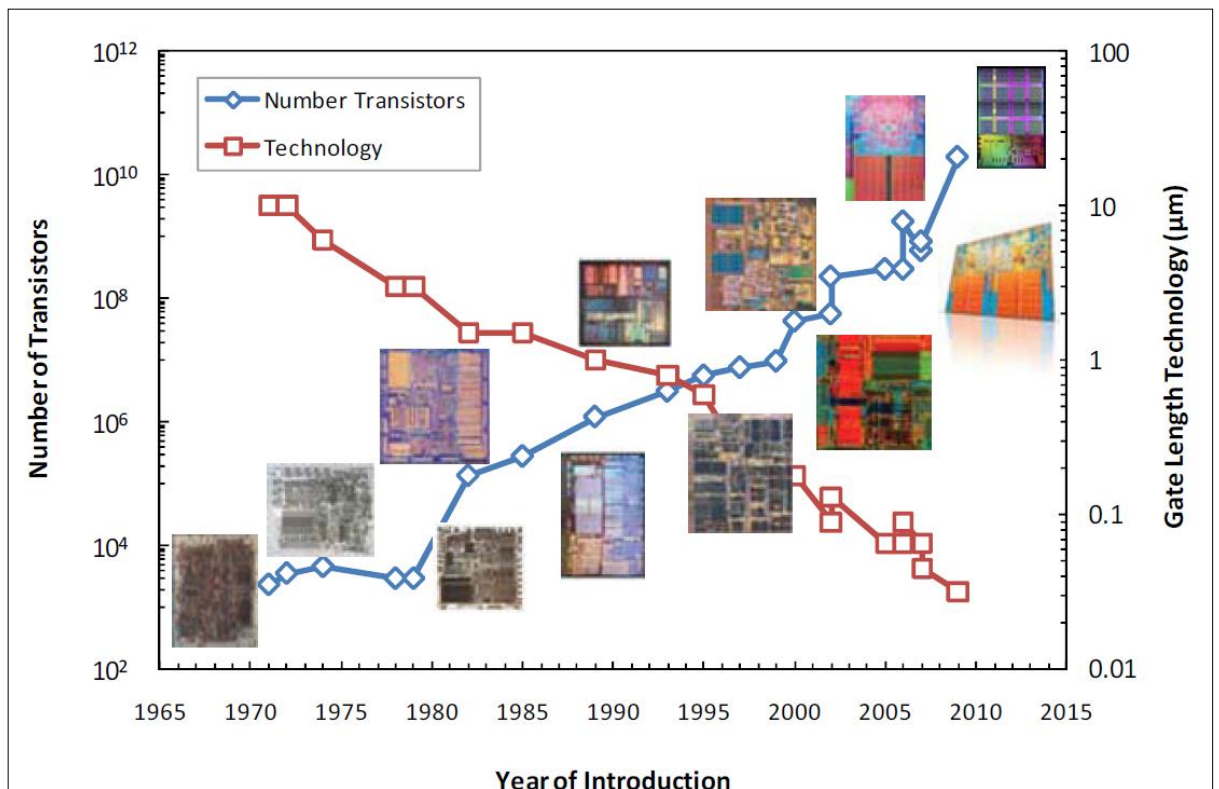


**Figure 1.1. Moore’s Law depicted in graphical form. Gordon Moore predicted that the number of transistors per chip would double every 18-24 months [Wilson, 2009, replotted from Intel Corporation]**

Moore’s Law has held true for decades but the time has come now when device scaling is becoming increasingly difficult [Thompson, 2003]. Device scaling has led to the introduction of new materials to the fabrication process to keep devices improving. FEOL has seen the introduction of  $\epsilon$ -Si technology, BEOL now uses Cu as an interconnect material.

### 1.3. Strained Silicon Technology

While both silicon and germanium are semiconducting materials, silicon is used more commonly due to its abundance and superior electrical properties. The development of a germanium transistor in 1948 led to a large market for Ge in the 1950s through to the 1970s, at which point silicon began to be more widely used in microelectronics.

The first silicon germanium, SiGe alloys were accomplished in the 1950s [Teal, 1975]. Strain in semiconductor materials began to receive attention throughout the 1970s [Brantley, 1973], though  $\epsilon$ -Si/SiGe, technology has been researched extensively since the late 1980s as it provides means to improve device performance in the face of device scaling limitations [Jain, 2003]. Strained silicon is a layer of silicon grown epitaxially on a silicon germanium ( $\text{Si}_{1-x}\text{Ge}_x$ ) virtual substrate, making use of the lattice mismatch between the two. This technique introduces a strained layer into the channel region of metal oxide semiconductor field effect transistors (MOSFET) structures which leads to, most notably, significantly higher mobility. Figure 1.2 shows a typical MOSFET structure. As devices continue to scale down, strain engineering is becoming more important and with it metrology techniques to monitor strain in the device are just as important. The amount of strain in the channel is related to the germanium content and this has a direct effect on the performance improvement. Therefore, it is vital to be able to accurately measure the strain and germanium content.

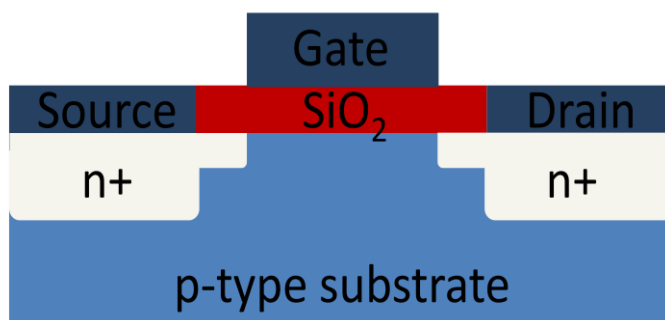


**Figure 1.2. Typical MOSFET structure, currently being fabricated with a channel length in the order of tens of nanometres. Strained silicon is usually introduced to the channel of the transistor.**

Strained Si plays a very important role as a performance enhancer as it becomes more difficult to scale devices laterally. As well as difficulties faced with scaling devices, it is challenging at these sub-100 nm scale to maintain several of the important electrical parameters such as drive current due to degradation of mobility [Reiche, 2010]. An increase in doping to counter short-channel effects degrades carrier mobility further. Extensive work has been done in the area of  $\epsilon$ -Si and it is becoming increasingly more

integral in semiconductor device manufacturing [Jain, 2003]. It has been shown to provide the performance enhancement required by counteracting some of the problems seen with standard Si substrates. This section gives a basic outline of how strain is achieved and what benefits this has on device performance. Current measurement techniques are introduced before being reviewed further in chapter 2.

Both silicon and germanium are group IV elements with a highly ordered crystalline structure and are next to each other in the periodic table. Silicon's atomic number is 14, the electrons per shell are 2, 8, 4 and electron configuration is  $3s^2, 3p^2$ . The atomic number of germanium is 32, the electrons per shell are 2, 8, 18, 4 and the electron configuration is  $3d^{10}, 4s^2, 4p^2$ . The two elements are chemically compatible, when mixed, they will form an alloy  $Si_xGe_{1-x}$  where  $x$  is 0 – 1. Both are face centred cubic elements (FCC). Within the cubic unit cell, atoms are located at all corners and centres of all cube faces. The crystal structure of both is as that of diamond [Ashcroft, 1988].

The distance between the atoms in a crystal, the lattice constant of the two materials is different, with germanium having a higher lattice constant than silicon. Figure 1.3 shows the basic unit cell of a diamond structure. The numbers represent the height of the atom as a fraction of the cell dimension [Kittel, 2005].

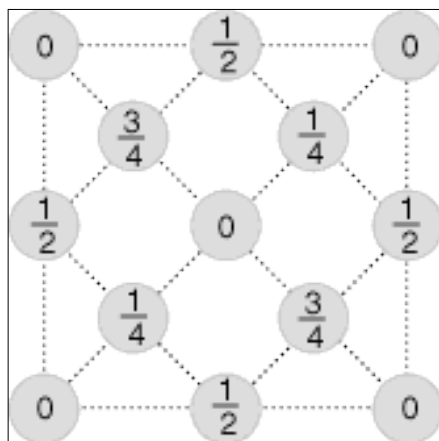


**Figure 1.3. Unit cell of a diamond structure [Kittel, 2005]**

There is a 4.2% lattice mismatch between silicon and germanium. A good approximation to the relation between the two can be shown by Vegard's law [Dismukes, 1964].

$$a(x)Si_{1-x}Ge_x = (1 - x)a_{Si} + xa_{Ge} \quad (1.1)$$

Where  $a_{Si} = 0.543$  and  $a_{Ge} = 0.566$  [Ashcroft, 1988]

Clearly, there is also a lattice mismatch between the Si substrate and the Si<sub>1-x</sub>Ge<sub>x</sub> strain relaxed ‘virtual substrate’ (VS), that is the layer between the underlying Si substrate and the ε-Si cap layer. It is this mismatch in lattice parameters which is integral to the formation of strain in the strained silicon structures.

Si<sub>1-x</sub>Ge<sub>x</sub> is grown epitaxially on a silicon substrate causing the Si<sub>1-x</sub>Ge<sub>x</sub> compressive strain in the virtual substrate, VS. If the VS is thin, this strain is coherent and the Si<sub>1-x</sub>Ge<sub>x</sub> epilayer is pseudomorphic i.e. it takes on the same crystal form as silicon as depicted in figure 1.4 A. The VS is compressed laterally and extended vertically. This is known as homogeneous or misfit strain.

If the germanium content increases in the Si<sub>1-x</sub>Ge<sub>x</sub> layer, the lattice mismatch increases. In this case, or if the VS is very thick, misfit dislocations occur which lead to strain relaxation. If the Si<sub>1-x</sub>Ge<sub>x</sub> layer is fully relaxed, then the crystal structure will be have the lattice parameter described in equation 1.1. This is shown in figure 1.4 B.

Strain relaxation will begin to occur above a certain thickness of the VS. This thickness directly depends on the germanium content in the substrate and is known as the critical thickness,  $h_c$ . Strain relaxation begins to occur due to the formation of dislocations [LeGoues, 1989]. The critical thickness is related to the lattice mismatch mentioned above. This mismatch is described by a mismatch parameter  $f_m(x)$  [Cammarata, 1989];

$$f_m(x) = \frac{a_x - a_{\text{substrate}}}{a_{\text{substrate}}} \quad (1.2)$$

Where  $a_x$  is the lattice parameter of the relaxed Si<sub>1-x</sub>Ge<sub>x</sub>. Combining equations 1.1 and 1.2 gives;

$$f_m(x) = 0.042x \quad (1.3)$$

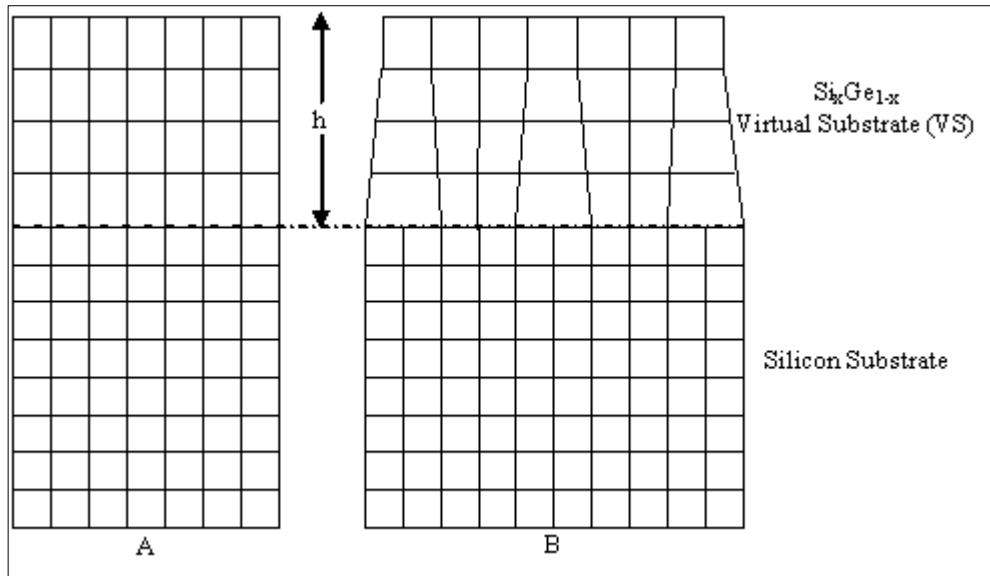


**Figure 1.4. A Homogeneous strain and B Strain relaxation caused by dislocations leading to a lattice mismatch between the SiGe and strained Si cap layer grown epitaxially on top of VS, thus leading to tensile strain.**

Dislocations and hence relaxation occur above the critical thickness described above. This is the same process for the strained silicon cap layer usually grown on the relaxed SiGe VS. However, the strain in the cap layer is critical to the improved device performance and so this thickness has to be precisely controlled to ensure no relaxation occurs.

### 1.3.1. Benefits of strain in devices

The International Technology Roadmap for Semiconductors (ITRS) [ITRS, 2011] predicted some years ago that silicon would begin to encounter scaling problems as it approached the 45 nm node due to the limits of mobility and gate leakage current [Telford, 2004]. Larger technology nodes can already partly rely on engineered substrates [Thompson, 2006] and theoretically, silicon could be reaching the end of its useful lifetime  $\epsilon$ -Si provides a means to delay this inevitable outcome. The use of strain as a performance enhancer has been known for in excess of 50 years [Mistry, 2004]. In devices, a  $\text{Si}_{1-x}\text{Ge}_x$  layer is usually grown epitaxially on single crystal Si substrate. A  $\epsilon$ -Si layer is then grown on top of the SiGe layer. The SiGe layer is grown to a thickness that ensures it is fully relaxed. Because of the larger lattice parameter of the relaxed SiGe VS compared to the Si cap layer, tensile strain is introduced. Other methods of creating a  $\epsilon$ -Si layer include sSOI, strained silicon on insulator. Ultimately, the effect is the same, a tensile strained layer of silicon, however, sSOI eliminates the SiGe VS making a less complex process and a thinner layer. The method and fabrication

techniques are discussed later in the thesis. The  $\epsilon$ -Si layer is used as the channel in a MOSFET structure. Strain introduced to the channel of the device is referred to as global strain and has been shown to improve device performance by more than 100% [O'Neill, 2006].

The improved performance comes about due to improved carrier transport of both holes and electrons. Modifications are induced in the valence and conduction energy bands which reduces intervalley scattering and increases carrier mobility [O'Neill, 2006]. Essentially, silicon atoms are further apart reducing atomic forces between them. It is these atomic forces that interfere with the movement of electrons, and so reducing them leads to better charge carrier mobility, and ultimately better performance of the transistors at lower energy consumption.

Biaxial tensile strain is controlled by altering the germanium content in the channel. This strain can be very precisely controlled. However, even though precise amounts of strain can be engineered in devices, several process steps, usually thermal, though also thin film deposition or oxide growth etc, can either induce or relax strain in the structures [De Wolf, 2003]. The effect of including a  $\epsilon$ -Si/SiGe stack has a large effect on the electrical parameters of the device. Features such as the band offset at the Si/SiGe interface due to smaller SiGe bandgap and dopant diffusivity in SiGe means device characteristics often need re-centred and material quality is paramount in ultra-large scale integration (ULSI) manufacturing [Rim, 2002]. These challenges force a trade-off between the need to alter characteristics and the improved mobility  $\epsilon$ -Si technology brings and continues to be integral to device design and fabrication.

### **1.3.2. Introduction to strain measurement in Silicon**

Measuring bulk silicon remains a relatively simple task, however, generally speaking, only an average strain value is acquired. Ideally, measurements of the strain gradient along the whole of the channel should be taken, as the strain at the source is different to that in the centre of the channel. In order to fully understand why the introduction of strain improves device performance, these differences also need to be understood. Strain can be either induced or relaxed by various process steps [De Wolf, 1996, Olsen, 2005]. It is important to know at any stage in the process that strain is being upheld in a device as this value affects the performance [Himcinschi, 2006].

Raman spectroscopy provides a quick, efficient and non-destructive method of measuring the strain in the devices mentioned above [Dietrich, 1993]. Raman scattering (explained in some detail in chapter 2) is inelastic light scattering. An incident beam of directional, coherent radiation of a specific wavelength i.e. a laser, shone at a sample surface will be predominantly reflected at the same wavelength. This is known as Rayleigh scattering. However, approximately one in every  $10^7$  photons scattered will have a different wavelength and polarization [Tobin, 1971]. Raman scattering is a measurement of the change of frequency of an incident photon when scattered by the sample.

When measuring strain, a measurement of the peak position due to silicon bonds in the  $\text{Si}_{1-x}\text{Ge}_x$  substrate peak and the strained silicon cap layer peak is taken and compared with the characteristic peak seen from silicon. The position of the Si in SiGe peak gives an indication of the germanium content in the sample and the  $\epsilon$ -Si cap layer peak can be analysed to gain a value of strain present. The ability to measure such characteristics in situ is vital. Due to its non-destructive nature, it provides an ideal measurement solution for monitoring strain throughout a manufacturing process flow.

In modern Raman spectroscopy, it is possible to focus the laser spot size down to approximately a micron. This means a spatial resolution of the same order is achievable. Devices are getting smaller to continue with the demands of Moore's law. Currently, the most modern devices commercially available have a channel length of only 45 nm. The laser spot size determines the x-y spatial resolution. Due to the large difference in device size compared to the laser spot size, it is currently only possible to measure an average strain.

Another problem faced with Raman spectroscopy, is where in the device is actually being measured. It is the strained silicon cap layer in the channel region that is the main area of interest. The cap layer is usually only 5-10 nm thick yet the penetration depth (z resolution) is often in the order of microns. With a green laser (514 nm), this is reduced to about half a micron. Even so, this is significantly larger than the desired penetration depth. UV Raman Spectroscopy overcomes the problem of penetration depth. Using Raman Spectroscopy with a 365 nm wavelength laser gives the required penetration depth of about 10-15 nm [Dietrich, 1999, Dombrowski, 1999].

Finally, Raman spectra are becoming more difficult to obtain. The intensity of the Raman scattering depends strongly on the volume of material being probed, in other words how much material is available to scatter the incident light. Smaller sample sizes mean fewer molecules from which light can scatter. Since Raman scattering accounts for only a very small amount of the total scattering, this intensity decreases quite rapidly with decreasing sample size. As devices decrease in size, the low intensity of the Raman signal from the strained Si cap layer can often be overshadowed by the signal from the underlying  $\text{Si}_{1-x}\text{Ge}_x$  virtual substrate. This causes peak overlap, which is difficult to analyse. This peak overlap is demonstrated in figure 1.5 where the strained silicon peak manifests itself as a small bump on the high wavenumber side of the Si in SiGe peak.

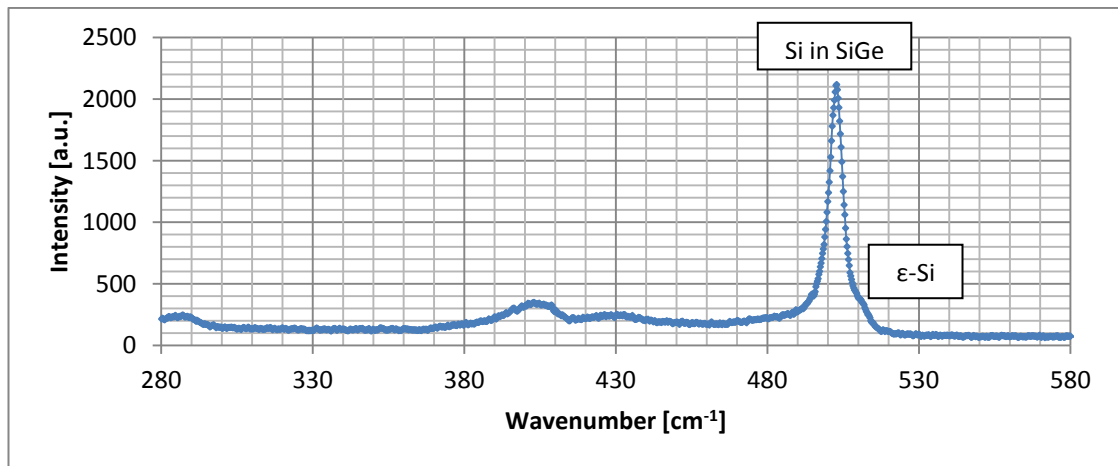


**Figure 1.5. Typical peak positions of Si-Si bonds in SiGe and the nearly hidden strained Si cap layer.**

Potentially powerful solutions to the aforementioned issues are surface enhanced Raman spectroscopy (SERS) and tip enhanced Raman spectroscopy (TERS). This involves coupling Raman spectroscopy with a metalized atomic force microscope (AFM) tip, described in some detail in chapter 2. In doing this, there is an enhancement in signal caused by the tip, which is confined to the area in the immediate vicinity of the tip apex, improving both the obtainable signal and the spatial resolution. SERS is a destructive technique and as such is currently not suitable in the highly cost-driven semiconductor industry. Despite current widespread research in the area of TERS, the effect remains not yet fully understood.

The most common method of measuring strain in such devices remains Raman spectroscopy. However, there are other methods available. For both economic and practical reasons, it is far preferable to measure the strain in a non-destructive manner. This way, as little or no sample preparation is required, the actual strain in the device is

being measured. Transmission electron microscope (TEM) based methods involve a lot of sample preparation. Most importantly, the device needs to be cleaved which may induce strain relaxation. Therefore, the results obtained will not give a true indication as to the nature of the device parameters. Destructive methods such as this are less cost effective as devices need to be sacrificed in order to measure the strain therefore they are not as attractive.

TERS is currently being widely investigated as a strain sensor for SiGe devices [Hecker, 2007, Saito, 2008]. There are, however, several mechanisms of this method which are still not fully understood. One of the main issues currently being researched is the reproducibility of good quality, robust tips. The challenges faced in fabrication of a TERS tip will be outlined in chapter 2. It is hoped that TERS will become a widespread application for the measurement of strain in the semiconductor industry, however, it will be shown that this is still a long way off.

The spatial resolution is limited not by the laser spot size but by the diameter of the tip apex in TERS. Semiconductor devices are currently being fabricated with a gate length of 45 nm. The most recently reported spatial resolution achievable with TERS is 25 nm [Saito, 2008]. Clearly, this is significantly better than the micron scale currently achievable with conventional Raman Spectroscopy meaning that more detailed information on the strain in a localised area can be achieved. For the purposes of an industrial tool, this resolution is sufficient. Ideally, to achieve the best possible x-y spatial resolution, a small tip apex that still provides the desired enhancement needs to be developed.

#### **1.4. Copper Interconnects**

As microelectronics technology has progressed, the demand placed on the materials used to fabricate devices, particularly the interconnect material used to give the transistors functionality has also increased. As previously described, as the number of transistors per chip increases, in order to keep the costs per transistor to a minimum, the chips have been scaled aggressively. Smaller chips leads to narrower interconnecting wires and a new set of stresses and strains that need to be characterised and understood.

Traditionally aluminium, Al, has been used as the interconnect material due to its low cost, relatively low electrical resistivity ( $28.2 \text{ n}\Omega\text{m}^{-1}$ ) and good conductivity [Zhao,

1997]. A very thin layer of native oxide, 2 – 3 nm, provides good protection for the interconnects during the many thermal processing steps involved in device fabrication. Aluminium is easy to deposit as a bulk layer and can be etched very easily to leave the interconnect pattern. ULSI means that interconnect dimensions are now deep submicron, so it stands to reason that the current density in the interconnects is now much greater than it was previously. There are inherent problems due to the low melting point of Al, and this can lead to degradation of the wires due to electromigration. Stress effects and voiding exacerbate this problem and are an outstanding cause of circuit failure.

In the first instance, electrical properties must be considered for alternative interconnect materials. Gold, silver and copper all have lower a lower resistivity than Al, however, gold and silver are costly materials, therefore copper, Cu, with an electrical resistivity of  $16.78 \text{ n}\Omega\text{m}^{-1}$  is used as an alternative to Al. Along with lower electrical resistivity, Cu has a higher melting point. It is thought that Cu functions as efficiently as Al with roughly half the cross sectional dimensions allowing the possibility of further device scaling without intensifying existing problems. Much research has been done into Cu interconnects indicating they have superior performance and reliability when compared to Al.

Copper was first used as a replacement to aluminium in 1997 at IBM where they began using electrochemical plating as a deposition method [Edelstein, 1997, Heidenreich, 1998]. This method is still widely used today. Meanwhile, Motorola and other companies developed a physical vapour deposition, PVD method of depositing copper interconnects. Electrochemical plating is good at filling challenging features such as those with a high aspect ratio and has shown good scalability down to dimensions seen in modern microelectronics.

#### **1.4.1. Stress and Strain in copper interconnects**

Although it is thought that Cu exhibits less failure mechanisms due to stress and electromigration, it is not without its problems. Cu has different mechanical properties to Al, and then again when considering the nanoscale where the interconnects begin to resemble a foil than a wire, there are many further sources of stresses to consider. The Young's modulus of Cu is 110 – 128 GPa, whereas with aluminium it is 70 GPa. It is thought that the effects from stress voiding are significantly improved in Cu. However,

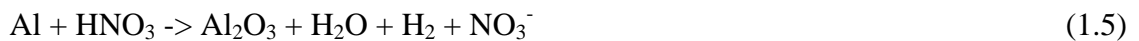
considering Hooke's law, equation 1.4, it is clear that for the same strain, there will be a larger stress present in Cu.

$$E = \frac{\sigma}{\varepsilon} \quad (1.4)$$

Where E is the Young's modulus.

#### 1.4.2. Deposition and Interconnect Patterning

Al is typically deposited as a blanket layer in a sputter chamber then patterned with photo resist which acts to block the etchant, leaving just the pattern of the interconnects post etch. Typically, wet etching is used to etch Al. An example of wet etchants used is acetic, phosphoric and nitric acid. Here, the aluminium is oxidised by the nitric acid, which is then dissolved by the phosphoric acid. The etch is driven by the concentration of phosphoric acid.



The above formulas are relatively straight forward. The chemistry involved in wet etching copper is much more complex as well as requiring a significantly higher process temperature. This has an overall effect on the thermal budget of the devices, as well as potentially introducing unwanted stress and strain effects. Aside from thermal effects, wet etching is highly isotropic and as such the patterned metal remaining post etch is subject to a few problems. There is often an issue with necking of the metal tracks or bridging leading to short circuits and device failure. Wet etching does not bring the precision that comes with dry etching; hence it is unsuitable for the narrow features involved in state of the art devices.

Reactive Ion Etching (RIE) or plasma metal etching is used to etch devices where wet etching is not appropriate, for example when more precision is required. 'Dry' plasma etching is an anisotropic process and so the etch is much more controlled and sharper features are achieved. To plasma etch Al, chlorine and hydrogen bromide are used. It is possible to use plasma etching to achieve the device sizes seen in state of the art microelectronics, however, it is not an option for Cu interconnects. Cu has a lack of volatile compounds making a dry etch process impossible [Shwartz, 2006].

A new deposition and etch process was developed by IBM in the early 1990s [Wilson, 2009]. The process, termed Damascene is illustrated below in figure 1.6. With this process, trenches forming the interconnect network are pre-etched and copper is deposited into these trenches. This allows for much more difficult features to be fabricated with precision.

An etch stop is required material is deposited on the silicon substrate to form the bottom of the trench that will ultimately form the via or interconnect. The etch stop acts as a barrier to the etch chemicals which are highly selective towards the material they are removing, and so only a very thin layer of etch stop material is required. On top of this layer, the dielectric is deposited. This is a much thicker layer into which the trenches for the interconnects are etched. Following photo resist patterning, the trench and via network is plasma etched and the resist stripped ready for Cu deposition, forming the interconnects.

A disadvantage of using Cu as an interconnect material is how quickly it diffuses into silicon. As such, a sidewall barrier needs to be deposited into the trenches prior to the copper deposition. There are several steps to create a single interconnect or via layer and typically modern ICs have 3 or 4 tiers to the interconnect structure. The interaction of each material forming an individual layer as well as the dimensions of the trenches themselves all have an effect on stress in the interconnect system. The dimensions of the interconnects greatly affect the microtexture formed due to the Cu layer being thinner and narrower. It is these stresses which can cause the problems mentioned earlier such as peeling, cracking, blistering etc.

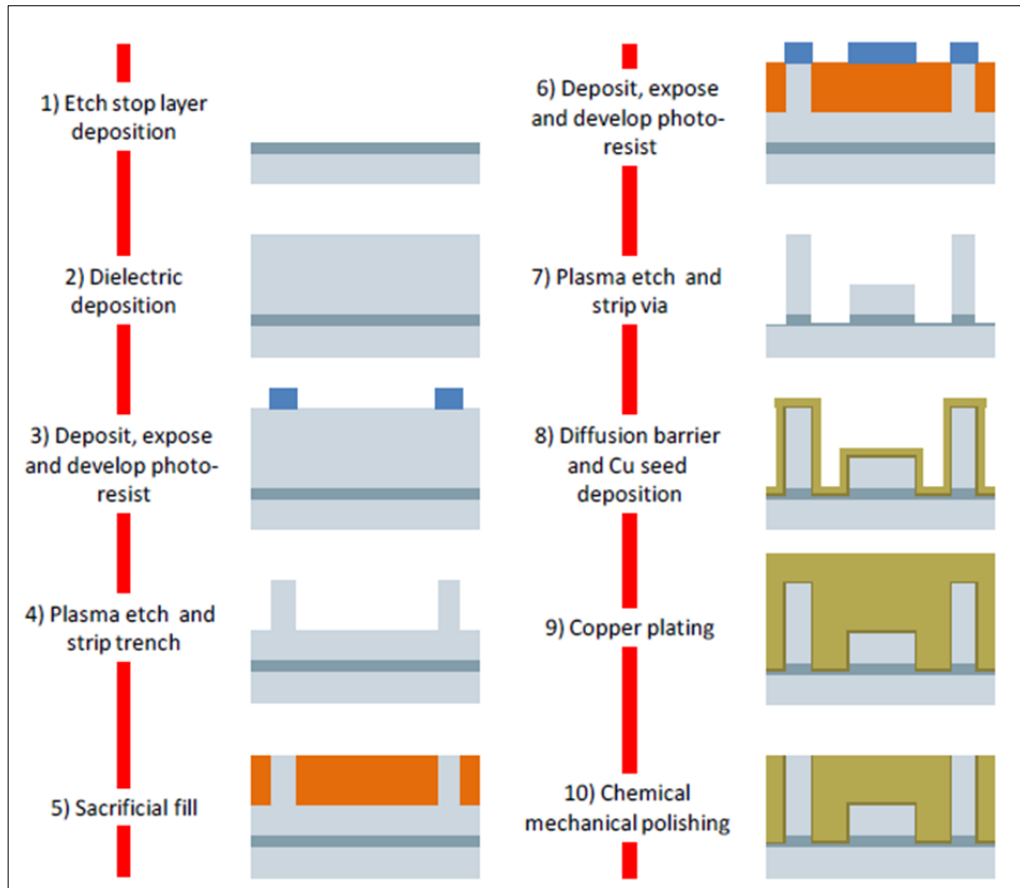


Figure 1.6. Process flow of a typical Damascene copper deposition procedure [Wilson, 2009].

### 1.5. Scope of the Thesis

This chapter has given a background to microelectronics and the semiconductor industry, expanding on the topics mentioned in the motivation for this study. How stress and strain relates to the materials used in this investigation has been discussed and the techniques used to characterise the materials were briefly introduced.

In Chapter 2 a survey of the literature will further illustrate these techniques and what they are currently capable of achieving. Where the existing work fits into the work of this thesis is considered here. Chapter 3 will focus on the methods executed throughout the project followed by a series of results chapters outlining what is attainable from the techniques and equipment currently available to industry and materials and surface scientists.

Chapter 4 is a comprehensive calibration chapter highlighting the importance of machine set up. In this chapter, Raman spectroscopy is discussed in some detail and the potential sources of variation in output are described. Chapter 5 uses conventional

Raman spectroscopy to investigate whether uniaxial strain can be achieved in sSOI stripes if the stripe is narrow enough to allow full strain relaxation in one direction. This chapter shows that the spatial resolution of conventional Raman spectroscopy can be pushed beyond that which is currently reported. Chapter 6 discusses SERS and TERS as a potential high spatial resolution replacement for conventional Raman spectroscopy strain measurements and maps. The limitations of the techniques are outlined in detail. Moving on to BEOL, chapter 7 provides an in depth discussion of using EBSD and nanoindentation as complementary techniques to assess the mechanical properties of very thin Cu films which represent those that would be used to form vias and interconnects in actual devices.

Finally, chapter 8 sees a discussion of the results and some conclusions are drawn on the suitability for the usage of these techniques in industry. This is followed some final remarks detailing what future work can be undertaken following up from this thesis.

## **1.6. Summary**

As devices reduce greatly in size, material and electrical properties need to be characterised and often monitored throughout the fabrication process. Current techniques are often incapable of characterisation at the scale of state of the art devices or due to their destructive nature, are not suitable for the highly cost driven semiconductor industry. The study of nanoscale materials is difficult, industrial applications will often take average measurements over much larger scales. Once materials and techniques are fully understood and a system becomes just a monitoring process, it is not always necessary to know anything else. Often, current techniques can be pushed further than their current application suggests.

This thesis aims to provide a comprehensive survey of current and new techniques and their application and suitability with the semiconductor industry. It is important that measurement techniques adopted in industry are able to be completed in-situ, are non-destructive, quick, simple to implement and do not add further costs to the process. Techniques are assessed with these factors taken into account.

## **Chapter 2. Techniques**

### **2.1. Introduction**

Raman Spectroscopy forms the basis for the bulk of the work executed throughout this thesis. Since its discovery, the technique has grown to include many applications ranging from biological or chemical processes to art and archaeology analysis. Its widespread application is in the main due to the precise nature of the technique, picking up incredibly small changes to a system or process that would go otherwise undetected. However, the attraction to this technique comes also from its non-destructive nature. These reasons are what make it such an excellent choice for determining strain in a semiconductor device. The theory of the technique and its ability to characterise strain are covered in this chapter.

Raman Spectroscopy does have its limitations. While the method is perfect for semiconducting materials, not all materials are Raman active and so the technique cannot be employed when dealing with metals such as the copper interconnects considered in this project. What makes a material Raman active is discussed within the theory of the technique. The problems arising from spatial and depth resolution are considered briefly before discussing recent developments to the technique, SERS and TERS that aim to overcome some of the limitations associated with the technique.

Finally, EBSD is introduced as a potential strain measurement technique and the difficulties associated with this. In the introduction, the ease of use a measurement technique to be applied in industry is emphasised. As a strain analysis tool, it is shown that this method is currently relatively complex. However, EBSD as a microtexture analysis tool is very powerful and aids greatly in the growing understanding of the very thin Cu films used in interconnects. Therefore, there is some discussion of the technique.

### **2.2. Background to Raman Spectroscopy**

In 1921, Sir C. V. Raman began a series of experiments on the scattering of light by transparent materials [Krishnan, 1971]. Raman's group at Calcutta initially set out to explain Rayleigh's well known theory of light scattering and states his inspiration for the work as the hope that;

“laboratory studies would furnish a solid experimental basis for the explanation of such natural phenomena as the colour of the sea and the colour of the ice in the glaciers.”

[Raman, 1929]

In work spanning from 1921 to 1929, through these experiments, he was able to accomplish much more than he originally set out to achieve. Experimental evidence in 1922 and 1923 showed the presence of an extra effect. Initially observed in purified water, alcohol, ice and optical glass amongst other samples, there was clear evidence that the expected light scattering was accompanied by a radiation of altered wavelength. The detection of this secondary radiation led to the ability to discover important information on the structure of materials. This secondary radiation, however, was of a much weaker intensity.

Significant to Raman’s research [Tobin, 1971] was an independent study that seemed to establish the presence of this effect, though in the X-Ray region rather than visible light at about the same time. Arthur H Compton published work in March and November 1923 detailing this investigation [Compton, 1923]. His work demonstrated that the spectrum of the primary X-ray beam is broken into two separate lines; an unmodified line i.e. one with the same wavelength as the incident beam and a modified line, with wavelength greater than the primary spectrum line. Initially, this effect was put down to ‘general fluorescent radiation’ [Compton, 1923] until spectroscopic studies showed the true effect of the altered frequencies i.e. that there is the additional line showing a decrease in energy – an increased wavelength – of the incident X-ray beam upon interaction with matter.

The difficulty in explaining this phenomenon did not go unnoticed and further investigation in 1924 and 1925 was undertaken. Attempts to make a spectroscopic study of the effect were carried out relatively unsuccessfully using sunlight and coloured glass filters as the excitation radiation. Due to the weakness of this second scattered radiation, it was almost impossible to photograph the spectrum. It wasn’t until the end of 1927 that the group were successful in their attempts.

In 1928, the discovery was announced at the meeting of the South Indian Science Association at Bangalore. The subject was also addressed in a letter to Nature [Raman, 1928] informing of this ‘new type of light scattering’.

The effect had been shown to theoretically exist in 1923 by a group led by Smekal. Around the same time as Raman's discovery, Landsberg and Mandelstam observed the effect in quartz [Woodward, 1967].

In the following few years, there was much work completed on this light scattering phenomena on a host of different sample types. So much so that by the 1940s there was well in excess of 2000 published works on the subject [Glockler, 1943].

### **2.2.1. The Raman Effect**

Light photons incident upon a sample will interact with it in some way. They may be reflected, absorbed or scattered. When the incident radiation is absorbed and then reradiated, this is known as fluorescence. Radiation that is scattered at exactly the same frequency as the exciting radiation is known as Rayleigh scattering. Rayleigh scattering can occur with any material. The Raman effect arises when a photon, which is incident on a material, interacts with its electric dipole and the light reflected is a different wavelength and polarisation to the incident [Horiba Jobin Yvon, 2007]. Raman demonstrated this effect through extensive experimentation and showed that a beam of monochromatic light of a certain frequency when incident on a on a sample will give rise to a spectrum of scattered light. The spectrum shows, in addition to Rayleigh scattering, a pattern of shifted frequencies. He was able to show that these shifted frequencies are independent of the frequency of the exciting radiation and are characteristic of the sample type [Krishnan, 1971].

Raman scattering is inelastic scattering where the reflected radiation has a different wavelength from that of the incident radiation. The difference in these two wavelengths is measured. The whole process of Raman scattering takes place in about  $10^{-12}$  s [Tobin, 1971]. Raman scattering occurs with a change of vibrational, rotational or electronic energy of a molecule [Kaiser Optical Systems Inc., 2007] and not all materials are Raman active.

Raman Spectroscopy was originally developed as a tool for use in chemical analysis. Specific information can be acquired allowing accurate characterisation of the various bonds in the material being characterised. This provides a means to identify samples or very subtle changes within a sample, for example, to monitor changes within a chemical process line. It wasn't until the 1970s that Raman Spectroscopy was discovered to be

useful as a strain characterisation technique. Key work from Anastassakis *et al* in 1970 discusses the effect uniaxial stress in silicon has on its Raman spectra [Anastassakis, 1970]. Experiments were able to show that uniaxial stress applied to silicon caused a shift in Raman peaks which were linear to the applied stress.

### 2.2.2. Raman Scattering

When a beam of monochromatic light is incident on a given sample, most of this light will be reflected at exactly the same frequency. This phenomenon is known as Rayleigh scattering, which is an elastic light scattering process. However, one in approximately  $10^7$  photons will be scattered at a different frequency [Kaiser Optical Systems Inc., 2007, Tobin, 1971]. This is known as Raman Scattering and is an inelastic scattering process.

Smekal worked with quantum theory to show this effect was possible theoretically in 1923 [Tobin, 1971], but it had never been observed, mainly due to the small probability of its occurrence. He showed that through the conservation of energy law, an inelastic collision with a molecule in the energy state  $E_p$  by a photon of light of frequency  $\nu$  then;

$$h\nu + E_p = h\nu' + E_q \quad (2.1)$$

where  $E_q$  is the energy state of the molecule after the interaction and  $h\nu'$  is the energy of the scattered photon [Glockler, 1943].

Alternatively, the effect can be described as follows. The incident radiation is made up of photons with a frequency of  $\omega_0$ , a small number of these photons are scattered at an altered frequency  $\omega_r$ . The frequency difference,  $\Delta\omega = \omega_r - \omega_0$  is the Raman frequency and a set of these numbers makes up a Raman spectra.  $\Delta\omega$  can have either a positive or a negative value. The Raman scattered photons are usually at a lower frequency – longer wavelength – than the incident radiation. The numbers that make up Raman spectra are the differences between the incident, exciting and the reflected, shifted frequencies. The shape and position of the peaks of Raman spectra are independent of the frequency of the exciting radiation. The intensity, however, is strongly dependent on the frequency and power of this radiation [Tobin, 1971]. Or;

$$\begin{aligned} & \text{Molecule(normal)} + \text{Radiation} = \\ & \text{Molecule(excited)} + \text{Radiation(degraded frequency)} \quad [\text{Raman, 1929}] \end{aligned}$$

Raman scattering can be split into two distinct lines; Stokes and anti-Stokes scattering. The scattering effects are depicted in figure 2.1. Where  $\Delta\omega < \omega_0$  this is known as Stokes scattering and, as previously mentioned, forms the bulk of the Raman scattered radiation. The reason for this is that most molecules in the sample in ambient conditions are at their lowest energy or vibrational state,  $m$ . Very few of the molecules are at a heightened energy state,  $n$ . When this is the case, anti-Stokes scattering occurs where the photon is scattered with a higher energy and  $\Delta\omega > \omega_0$ . Virtual states, as the name suggests are not real energy states but are instead created when the incident photon interacts with a molecule. Their energy is determined by the frequency of the incident radiation [Smith, 2005].

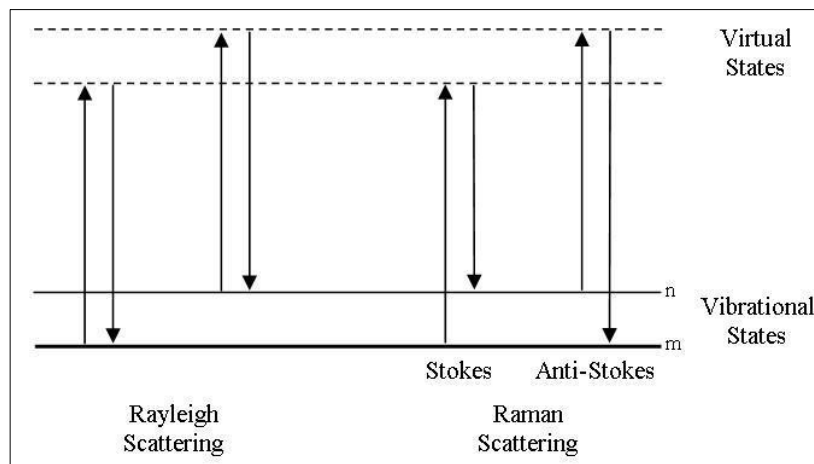


**Figure 2.1. Depiction of the Rayleigh (elastic) and Raman (inelastic) Stokes and Anti-Stokes Scattering processes.  $m$  is the lowest vibrational state and the states above are of increasing energy. Photons incident on a sample can interact with it in several ways, they can be scattered elastically, Rayleigh scattering or inelastically, Raman Scattering.  $m$  and  $n$  represent vibrational energy states of the molecule. The virtual states are determined by the frequency of the incident radiation.**

Such virtual states are energy states that are lower in energy than a real electronic transition. The de-excitation occurs almost immediately and with it, there is a change in vibrational energy. This vibrational energy is usually dissipated as heat [Kaiser Optical Systems Inc., 2007].

Figure 2.2 shows the Feynman diagram and associated energy levels of the dominant Stokes scattering process. The diagram is explained as an incident photon of frequency  $\omega_i$  interacts with an electron in the sample, changing the electron's energy from ground state,  $|0\rangle$  to a state  $|l\rangle$ , creating a phonon with frequency  $\omega_j$ . Electron-phonon interaction excites the electron to a state  $|m\rangle$  and a photon of frequency  $\omega_s$  is emitted.

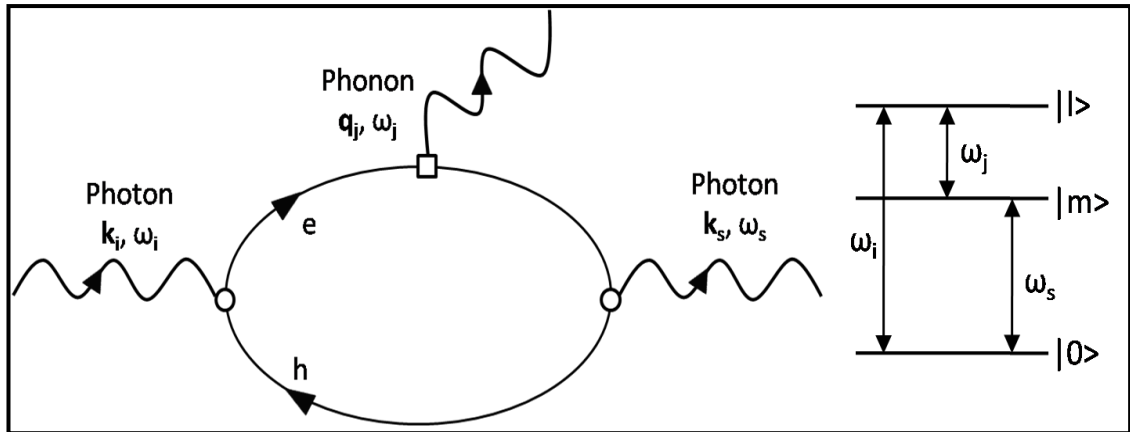


Figure 2.2. Feynman diagram and energy levels of the Stokes scattering process. Incident photon of frequency  $\omega_i$  interacts with an electron in a molecule changing its energy from ground state to state  $|l\rangle$ . This creates a phonon with frequency  $\omega_j$ . Electron-phonon interaction excites the electron to a state  $|m\rangle$  and a photon of frequency  $\omega_s$  is emitted. [De Wolf, 1996]

### 2.2.3. Rotational and Vibrational Raman Scattering

The pattern of shifted frequencies in a Raman spectrum arise from the rotational and vibrational states of the molecule or crystal being examined, however, Raman Spectroscopy can be thought of as a vibrational spectroscopy. Scattered photons arising from the rotation of molecules are significantly weaker than those from the vibrations of molecules as these frequencies are of an order of magnitude smaller than their vibrational counterpart [Krishnan, 1971]. Such weak signals are difficult to analyse.

Comparatively, molecular vibrations will manifest themselves as distinct lines and bands altered by large frequency shifts from the exciting radiation. Measuring this shift or peak will give the vibrational frequencies of the molecules [Tobin, 1971].

The case is similar in a crystal lattice. The crystal lattice structures employed in the field of semiconductors are strongly Raman active and as such, small changes in the structure, such as those caused by strain can be picked up to a high accuracy. Vibrations in crystals as with molecules will manifest themselves on a spectrum as distinctive lines or peaks, which have been significantly shifted from the incident radiation. The measured shift gives the vibrational frequency of the crystal [Krishnan, 1971].

### 2.2.4. Polarizability and selection rules

The key features of polarizability and what makes a sample Raman active can be described using electromagnetic field descriptions [Kaiser Optical Systems Inc., 2007].

A dipole moment, P induced in the molecule by the incident photon can be expressed as

$$\bar{P} = \alpha \bar{E} \quad (2.2)$$

Where  $\alpha$  is the polarizability of the molecule. This equation is too simplistic in that it assumes the polarization has the same direction relative to the incident field [Tobin, 1971]. The polarizability is actually a tensor expressed as [Smith, 2005];

$$\begin{bmatrix} P_x \\ P_y \\ P_z \end{bmatrix} = \begin{bmatrix} \alpha_{xx} & \alpha_{xy} & \alpha_{xz} \\ \alpha_{yx} & \alpha_{yy} & \alpha_{yz} \\ \alpha_{zx} & \alpha_{zy} & \alpha_{zz} \end{bmatrix} \begin{bmatrix} E_x \\ E_y \\ E_z \end{bmatrix} \quad (2.3)$$

The first subscript refers to the direction of polarizability of the sample, the second to the incident radiation.

The polarizability of a molecule refers to the ease at which the electron cloud surrounding it can be distorted i.e. polarized. Raman scattering will occur when there is a change in the vibration, which brings about a change in the polarizability,  $\alpha$ . This is described by [Kaiser Optical Systems, 2007];

$$\frac{\partial \alpha}{\partial Q}$$

Where Q is the normal coordinate of vibration [De Wolf, 1996]. Clearly, for a sample to be Raman active, there must be a change in polarizability. If this is not the case, the induced dipole will scatter the light elastically, Rayleigh scattering.

So, for a material to be Raman active, the selection rule can be stated as;

$$\frac{\partial \alpha}{\partial Q} \neq 0 \quad (2.4)$$

This is most apparent for centrosymmetric molecules and thus Raman Spectroscopy can give complimentary information to that observed from other forms of vibrational spectroscopy such as infrared spectroscopy. This is because such symmetric vibrations cause the greatest change in polarization and therefore the greatest scattering, which contrasts infrared spectroscopy where asymmetric vibrations cause the greatest absorption and hence are more intense [Smith, 2005].

### 2.2.5. Strain Analysis Using Raman Spectroscopy

In 1970 a key piece of work showed Raman Spectroscopy as a reliable and efficient stress sensor for silicon [Anastassakis, 1970]. The global strain present in a  $\epsilon$ -Si device depends primarily on the germanium content. However, there are other factors to induce strain in a structure such as process induced local strain and strain relaxation from thermal steps [De Wolf, 1996]. The attractiveness of Raman spectroscopy over other strain characterisation techniques is its non-destructive nature. This method can be used to monitor such changes in the manufacturing process in situ, in particular after a thermal step. The signal collected contains information from a volume probed by the laser. This volume is determined from the size of the spot size and penetration depth of the exciting laser. Currently, with UV Raman spectroscopy, the laser spot size can be focused to approximately half a micron and the penetration depth is a few nm giving the best quality information from the surface of the sample [Dombrowski, 2001]. Devices with a feature size of about the same size as the laser spot can be very accurately measured.

#### 2.2.5.1. Stress measurement

Raman spectroscopy does not directly give information about strain and instead gives information about the vibrational modes of the crystal lattice. This vibrational mode is directly related to strain or germanium composition. This relationship is demonstrated below.

Stress and strain are related by Hooke's law;

$$E = \frac{\sigma}{\epsilon} \quad (2.5)$$

Where  $\sigma$  is the stress in the sample,  $\epsilon$  is the strain. E is the Young's modulus, a modulus of elasticity that describes the materials tendency to be elastically deformed.

From Hooke's law, the uniaxial stress along the [100] direction of a Si/SiGe sample can be calculated.

$$\epsilon_{11} = S_{11}\sigma \quad (2.6a)$$

$$\epsilon_{22} = S_{12}\sigma \quad (2.6b)$$

$$\epsilon_{33} = S_{12}\sigma \quad (2.6c)$$

$S_{ij}$  are the elastic constants.

De Wolf [De Wolf, 1996] shows that the following equations can be adopted to calculate stress from the associated shift in peak position:

$$\Delta\omega_1 = \frac{\lambda_1}{2\omega_0} = \frac{1}{2\omega_0} (pS_{11} + 2qS_{12})\sigma \quad (2.7)$$

$$\Delta\omega_2 = \frac{\lambda_2}{2\omega_0} = \frac{1}{2\omega_0} [pS_{12} + q(S_{11} + S_{12})]\sigma \quad (2.8)$$

$$\Delta\omega_3 = \frac{\lambda_3}{2\omega_0} = \frac{1}{2\omega_0} [pS_{12} + q(S_{11} + S_{12})]\sigma \quad (2.9)$$

The phonon deformation potentials, p, q and r, and the elasticity constants,  $S_{ij}$  can be found in literature but there is some discrepancy over values [Dobrosz, 2006]. The values chosen in this investigation are as follows, chosen due to being more widely adopted [Anastassakis, 1970]

$$S_{11} = 7.68 \times 10^{-2} \text{ Pa}^{-1}; \quad S_{12} = -2.1410 \times 10^{-12} \text{ Pa}^{-1}; \quad S_{11} = 12.7 \times 10^{-12} \text{ Pa}^{-1}$$

$$p = -1.43\omega_{02}; \quad q = -1.89\omega_{02}; \quad r = -0.59\omega_{02}$$

Therefore, uniaxial stress is calculated by [De Wolf, 1996];

$$\Delta\omega_3 (\text{cm}^{-1}) = -2 \times 10^{-9} \sigma (\text{Pa}) \quad (2.10)$$

In the case of biaxial stress

$$\Delta\omega_3 = \frac{1}{2\omega_0} [pS_{12} + q(S_{11} + S_{12})](\sigma_{xx} + \sigma_{yy}) \quad (2.11)$$

$$\Delta\omega_3 (\text{cm}^{-1}) = -4 \times 10^{-9} \left( \frac{\sigma_{xx} + \sigma_{yy}}{2} \right) (\text{Pa}) \quad (2.12)$$

The strain value is calculated by;

$$\varepsilon = \frac{520.7 - \omega}{4.569 \times 169} \quad (2.13)$$

Where  $520.7 \text{ cm}^{-1}$  is the peak position of unstrained silicon,  $\omega$  is the peak position of the strained silicon. 169 GPa is the Young's modulus of [100] silicon at  $0^\circ$  and  $90^\circ$  and 4.569 is a constant derived from the equations above from the papers of Anastassakis, 1970 and De Wolf, 1996.

### 2.2.6. Spatial and Depth Resolution

The volume of material probed by the laser is dependent on the wavelength of the laser used, the type of material being analysed and to a lesser extent, the power of the laser. This will determine the laser spot diameter and the penetration depth of the laser.

The importance of the technique's resolution is clear when looking at the dimensions of the devices being characterised. Generally, only the top few nanometres in a sample are of interest and the x-y dimensions are in the range of tens of nanometres. The laser spot size can be determined by a simple calculation but is typically 0.50 – 1  $\mu\text{m}$ .

$$d = \frac{1.22\lambda}{NA} \quad (2.14)$$

Where  $d$  is the laser spot diameter,  $\lambda$  is the laser wavelength and NA is the numerical aperture of the objective in use. The x-y spatial resolution is limited to the laser spot size. With conventional Raman Spectroscopy and using a UV laser, 364 nm, the achievable resolution is just under half a micron. The power profile of the laser spot is Gaussian, hence most of the signal is collected from the centre of the spot. With careful measurements and deconvolution of the obtained signal, this resolution can be improved somewhat but there is a question over the accuracy of the results. Refer to chapter 5 for further discussion of this method. The spatial resolution of conventional Raman spectroscopy is the main limitation of this technique for nanoscale strain characterisation and the key motivation for development of techniques that improve the resolution.

The germanium content in the SiGe alloy will significantly alter the penetration depth into the sample as discussed in chapter 4. Generally, the area of interest is the strained silicon cap layer [Dobrosz, 2006]. If a laser with its wavelength in the visible region is used as a radiation source, the peak from the strained layer is overshadowed by the information gained from the other layers, making the strained layer peak difficult to analyse, or often, even see. Consequently, it is often better to use a UV laser as the radiation source for probing just the first few nanometres. UV-Raman is a relatively new development in Raman Spectroscopy with a lot of the research using this particular wavelength being completed in the late 1990s [Dombrowski, 1999]. UV was an attractive option for characterising silicon for two reasons. Firstly, the reduced penetration depth discussed but also the resonance effect from this particular excitation

wavelength. Resonance Raman scattering occurs when the frequency of the exciting radiation is close to the frequency of an electronic transition of the sample material. Large signal enhancements are possible, up to the order of  $10^6$  [Smith, 2005]. Silicon/SiGe spectra from UV-Raman only gives information from the top layer of the sample, so information from the underlying layers is lost. If this information is required, then a laser in the visible region should be chosen.

If the silicon being probed is a small isolated structure, such as in the case of strained silicon on insulator (sSOI) stripes, then information from the underlying silicon will still be present on the spectrum. This will manifest itself as a broad silicon peak with the information from the stripe represented as shoulder on the low wavenumber side of the peak. In this case, the spectrum can still be difficult to analyse.

Developments in this field to help overcome these limitations have been researched for decades. Relevant developments include Surface Enhanced Raman Spectroscopy (SERS) and Tip Enhanced Raman Spectroscopy (TERS).

### **2.3. Surface Enhanced Raman Spectroscopy and Tip-Enhanced Raman Spectroscopy**

Raman Spectroscopy is good for probing very small volumes of material and gaining sensitive information about the material's structure. However, spatial resolution and signal intensity are still major limitations when nanoscale devices and materials are under consideration. While these limitations can be overcome to some extent, refer to chapter 5, the method is difficult and time consuming. Research groups have been working for several years to develop related techniques to overcome sensitivity and spatial resolution problems.

Surface enhanced Raman spectroscopy (SERS) and tip enhanced Raman spectroscopy (TERS) are currently the focus of research for many groups in all applications of the technique. Even more than 30 years after surface enhanced Raman scattering was first observed, there is still much debate in literature on the exact mechanisms behind the enhancements seen with these two methods. Groups focussing solely on TERS for improved semiconductor characterisation are few as, while it can be relatively simple to gain an enhanced signal and even single molecule detection from several chemicals or other structures [Gouadec, 2007], with semiconductors it is somewhat more difficult.

### **2.3.1. Surface Enhanced Raman Spectroscopy (SERS)**

Surface enhanced Raman scattering was observed in 1974 by Fleischmann *et al* [Fleischmann, 1974, Tian, 2002]. While the exact mechanisms behind the enhancement are still open to debate, it is widely accepted that there are two components to this enhancement.

One component from a near field electromagnetic enhancement and a component related to chemical enhancement [Pettinger, 2004]. This chemical enhancement factor is related to a localised resonance Raman enhancement [Kneipp, 1997]. SERS enhancement factors of  $10^8 - 10^{14}$  have been reported [Anderson, 2000].

SERS involves adsorbing metal ‘island films’ onto the sample surface which is made up of typically, gold or silver nanoparticles of the order of 20 – 40 nm [Hayazawa, 2005]. Theoretically, in the case of a strained silicon cap layer, this allows high selectivity to the strained layer as opposed to the often overwhelming signal from the underlying silicon and SiGe layers. However, this method isn’t particularly attractive for the semiconductor industry. The presence of the metal island film usually makes this a destructive technique that cannot be easily carried out in situ.

SERS was a precursor to the development of tip enhanced Raman scattering, the mechanisms of which are similar. Because of the similarity, the enhancement components are discussed in more detail below.

### **2.3.2. Tip Enhanced Raman Spectroscopy (TERS)**

The SERS effect can be localised to the area in the immediate vicinity of a metallised tip apex. The metal tip functions as a small particle to excite SERS without the use of a metal film. This local surface enhancement is termed tip enhanced Raman spectroscopy (TERS). This allows Raman imaging at the nanometre scale [Hartschuh, 2003].

The metal tip commonly comprises of an Atomic Force Microscope (AFM) tip coated with a suitable metal such as those mentioned above. Early work using a SNOM Raman set up and achieving a 150 nm resolution [Webster, 1998] was followed up with work by M. S. Anderson in 2000 shows a Raman system coupled with an AFM termed RAFM or Raman Atomic Force Microscopy. He demonstrated the potential to use an

AFM tip to provide spatially selective enhancement of a Raman signal using the SERS effect [Anderson, 2000].

The AFM was developed in the 1980s as a surface analytical tool for insulators capable of atomic resolution [Binnig, 1986]. There are three main modes to AFM termed tapping mode, contact mode and non-contact mode. Contact mode only will be considered in this brief explanation.

The sample surface is scanned with a sharp tip at the end of a cantilever. The tip is illuminated by a laser. The cantilever bends due to forces between the sample surface and the tip. The deflected laser light is measured by a detector. Contact mode gives large forces leading to results that are more reliable and is currently the main option for use with TERS. However, when characterisation films that are nanometres thick, there is a chance that these forces will damage the film and so non-contact TERS would be preferable.

The size of the metal particles coating the tip strongly affects the size of the enhancement [Hayazawa, 2000]. In literature, the suggested values for the size of these grains can range from 10 nm to about 200 nm [Anderson, 2002, Christiansen, 2007]. The particles must be much smaller than the incident wavelength and the metal chosen must have the properties allowing them to generate surface plasmons. The actual optimum size depends on the type of metal used to coat the tip and the material of the underlying cantilever substrate [Yeo, 2006]. The size of grain it is possible to achieve also depends on the type of metal used along with the coating technique.

Figure 2.3 shows the laser illuminating the metal tip. The incident photons are absorbed into the metal particles through the collective oscillations of electrons on the surface (plasmons) [Anderson, 2000]. This creates a large electromagnetic field at the tip apex and limits the spatial resolution to the diameter of the tip. For this to be effective, the sample should ideally be polarised to block any of the far field signal. The importance of this is discussed in chapter 6.

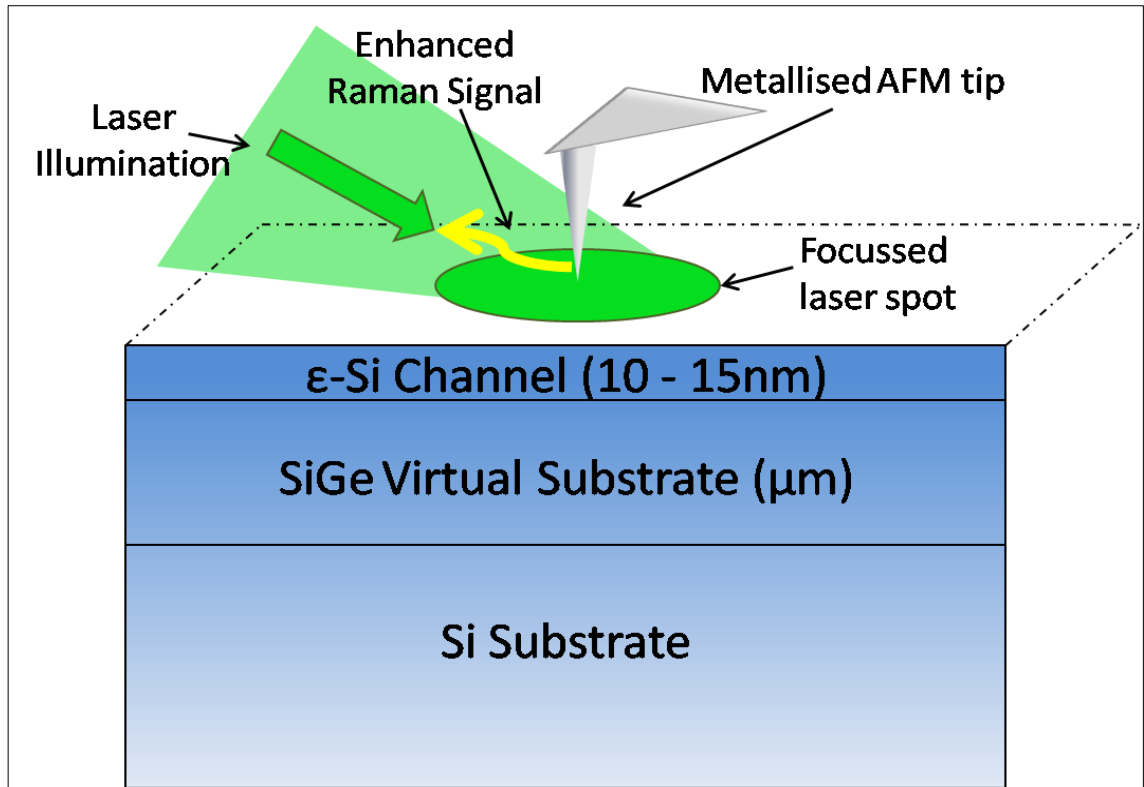


**Figure 2.3.** TERS setup on a  $\epsilon$ -Si/SiGe sample. The laser illuminates the metallised AFM tip creating a large electric field in the area directly underneath the tip apex. This has the effect of creating a surface selective enhancement with a significantly improved spatial resolution.

Among the groups actively working on Si/SiGe TERS are Saito *et al* [Saito, 2008, Tarun, 2008] and Georgi *et al* [Georgi, 2007]. Both groups report using silver coated tips with a 488 nm exciting wavelength. Saito reports a 25nm spatial resolution whilst Georgi states a 60% improvement in signal.

### 2.3.3. The Effect of a metallised tip

The following sections are concerned with how the optical and electromagnetic properties of nanoscale sized metal particles on AFM tips give rise to an electromagnetic enhancement. One of the biggest challenges faced in TERS development is the creation of a reliable, robust tip that gives repeatable results. Several manufacturers fabricate tips for use with TERS and these are widely commercially available. However, there is some debate over which method produces the best quality tip [Bonaccorso, 2007, Christiansen, 2007]. It is thought that the enhancement comes not just from the metal nanoparticle, but as much from the gap between adjacent nanoparticles [Smith, 2005]. Ordered arrays of nanoparticles need to be understood and characterised [Leff, 1995, Alexandrov, 2005] and the findings considered when developing a robust TERS tip. Therefore, each tip produced needs to be identical and

this can be very difficult to realise. Methods of fabricating tips and the challenges faced are outlined here, as well as the theory behind what causes the enhancement.

### 2.3.3.1. *Localised Surface Plasmons*

The electromagnetic response of a metal is different to that of a dielectric due to its different electronic nature. Electrons in a dielectric are bound to their respective atoms, and hence they are non-conductive. However, electrons in a metal are relatively free and can sometimes behave like a plasma [Helseth, 2005]. This phenomenon has been known for several decades [Agdur, 1964].

The electron density in a metal oscillates with a frequency known as the plasma frequency. Bulk metals can be characterised by this as follows [Pendry, 1996];

$$\omega_p = \sqrt{\frac{ne^2}{m\epsilon_0}} \quad (2.15)$$

Where  $\omega_p$  is the plasma frequency,  $n$  is the electron density number, ( $n_{Au} = 5.9 \times 10^{28} \text{ m}^{-3}$ ;  $n_{Ag} = 5.86 \times 10^{28} \text{ m}^{-3}$ ;  $n_{Cu} = 8.47 \times 10^{28} \text{ m}^{-3}$  [Ashcroft, 1988]) and  $m$  is the electron mass =  $9.11 \times 10^{-31} \text{ kg}$

Similarly, smooth metal surfaces are covered with the conduction electrons, held in the lattice structure by the positive charge from the metal centres. The electron density extends a certain distance away from the surface. The electrons are relatively free to move laterally along the metal surface. When light interacts with the surface electron, they start to oscillate collectively. Such collective oscillations are known as surface plasmons [Smith, 2005]. When a surface plasmon combines with a photon, this known as a surface plasmon polariton (SPP) [Zayats, 2003].

There is a frequency (or a very small range of frequencies) at which this oscillation will allow the most efficient scattering or absorption of the incident beam of light. This frequency is known as the plasmon resonance frequency. As expected, it differs with the type of metal being considered. Silver and gold have a surface plasmon resonance (SPR) frequency in the visible range and so are suitable for use with near Infrared (NIR) and visible laser systems.

The surface plasmon frequency is related to the bulk frequency by the following equation.

$$\omega_{sp} = \frac{\omega_p}{\sqrt{\varepsilon_0 + 1}} \quad (2.16)$$

$\varepsilon_0$  here is the dielectric constant of the surrounding media, in the case of air (at 1 atmosphere), this is 1.00059 so the equation simplifies to:

$$\omega_{sp} = \omega_p / \sqrt{2} \quad (2.17)$$

The surface plasma frequency is the solution Maxwell's equations. Several authors have published work showing a method known as Finite Difference Time Domain (FDTD) method which solves Maxwell's equations to show the interactions between surface plasmons and the incident radiation [Demming, 2005, Micic, 2003, Milner, 2001].

Silver and gold nanoparticles resonate in the visible region of the electromagnetic spectrum. However, if the frequency of the surface plasmons was to be calculated for most bulk metals using the equations above then the result will be in the UV region of the spectrum. Presumably, at the nanoscale, metal particles exhibit rather unique characteristics when compared to bulk metals.

So far, only a smooth metal surface has been considered. Additionally, on structures such as metal particles or roughened metal surfaces, there are localized surface plasma excitations known as local surface plasmons (LSP). Localized surface plasmons are restricted to curved metal structures on the nanoscale, with their frequencies highly dependent on the size and shape of the structure [Hutter, 2004]. These localised surface plasmons are integral in the enhancement seen by SERS. The range of frequencies in which such modes exist is limited by the plasma frequency of the bulk material. Whilst LSPs can be resonantly excited by light of an appropriate wavelength/frequency irrespective of the excitation light wavevector, SPPs can only be excited if the frequency and wavevector of the excitation light match that of the SPP [Zayats, 2003].

### **2.3.3.2. *Electromagnetic Enhancement***

It is widely accepted that, of the two signal enhancement factors, the main contributing factor is the electromagnetic enhancement [Christiansen, 2007, Pettinger, 2004]. The

field enhancement occurs due to the oscillation of local surface plasmons near the tip apex.

At the nanoscale, metal particles are known to demonstrate resonant behaviour at optical wavelengths. This behaviour is critical in the near field enhancement of Raman signals in both SERS and TERS.

Whilst the approximation below is very basic and does not take into account surface roughness, a sphere model can be used to describe the electromagnetic effect, and hence the enhancement caused by the particles. The field at the surface of a curved metal object subjected to the applied electric field from the excitation laser can be described by [Smith, 2005];

$$E_r = E_0 \cos\theta + g \left(\frac{a^3}{r^3}\right) E_0 \cos\theta \quad (2.18)$$

Where;

$$g = \left(\frac{\varepsilon_1(\nu_L) - \varepsilon_0}{\varepsilon_1(\nu_L) + 2\varepsilon_0}\right) \quad (2.19)$$

$E_r$  and  $E_0$  are the total electric field at a distance  $r$  from the sphere surface and the applied electric field respectively.

$a$  is the radius of the sphere

$\theta$  is the angle relative to the direction of electric field

$g$  is a constant associated with the dielectric constants of the metal and the surrounding medium

$\nu_L$  is the frequency of the incident radiation

When  $g$  is at a maximum,  $\varepsilon_0$  is usually close to one (the value of the dielectric constant of air is 1.00059 at 1 atmosphere pressure). Therefore,  $\varepsilon_1$  must be equal to -2 to create a maximum.

The dielectric permittivity of a metal is complex and therefore metals can both scatter or absorb incident radiation. The real part of the dielectric constant is associated with scattering while the complex is associated with absorption. The ratio between the two

depends strongly on the type of metal. Silver is a good at scattering light and is one of the reasons why it is favourable in SERS and TERS [Smith, 2005].

If we consider SERS, it can be seen that the greatest enhancement occurs, not from an isolated particle but from the points between adjacent particles or small clusters of particles. Enhancement can be observed from single, isolated particles [Klar, 1998] but it is the interactions between particles that cause the largest observed enhancements.

For the purposes of this work, one of the most important factors is the plasmon resonance frequency as this dictates which laser frequency can be used with the set up. The spatial resolution is controlled by the laser spot size, and has been shown to be greatly improved by the introduction of the metal tip already discussed. However, the depth resolution is predominantly controlled by the wavelength of the exciting laser. The localised surface plasmons also have a role in the depth resolution. The electric field enhancement,  $E_r \propto \frac{1}{r^3}$ . The further from the tip, the weaker the effect from the electromagnetic enhancement. This is because the TERS effect is surface selective. The plasmons will enhance the signal a certain distance from the tip apex which may be significantly smaller than the penetration depth of the exciting laser.

Silver and gold are currently the most common metals for both SERS and TERS. However, the resonance frequency of tips formed from these metals falls in the visible or NIR regions of the spectrum meaning they scatter the light from lasers with much longer wavelengths and consequently, much larger penetration depths most efficiently.

UV-TERS needs much consideration and is not something that can easily be achieved. To date, few people claim to have achieved UV TERS measurements of strained silicon. Poborchii *et al* claimed to have obtained an enhanced Raman signal from a silicon sample using a silver topped quartz AFM probe illuminated with a 364 nm laser light [Poborchii, 2005]. The same group have recently reported aluminium as being a suitable material for tip coating. Their results showed little enhancement, however.

The reason behind so little work in this area is likely to be due to the difficulties in getting standard silver or gold etched wires or coated AFM tips to resonate in the UV region. Several groups have claimed it is possible to 'tune' the resonance frequency of a coated dielectric tip. For example, in 2007 Cui *et al* showed that simply by increasing the refractive index of the underlying dielectric tip can significantly red shift the excited

localised plasmon modes [Cui, 2007]. Separately, work has been done on the optical properties of metal-dielectric multilayers. Wang *et al* in 2006 examine the optical properties of such multilayers in the UV region as little work has been done in this area [Wang, 2006]. Tachibana *et al* report on the optical properties of metal-dielectric multilayers [Tachibana, 2003]. Here, they find that the plasma resonance frequency is dependent on layer thickness and the dielectric constant of the material used with the resonance frequency decreasing with an decrease in film thickness or an increase of dielectric constant.

It has previously been mentioned that bulk metals have a plasma frequency in the UV region whilst the localized surface plasmons from metal nanoparticles cause the resonance frequency to shift to the visible/NIR region. This major obstacle needs to be overcome if UV TERS is going to be realised. The surface plasmon interactions between the metal and its surrounding media are detailed above. If a dielectric is now added to the metal surface, a new set of interactions occur at the interface between the metal film and dielectric, depending on the thickness of both the metal and the underlying dielectric substrate.

#### **2.3.4. Tip fabrication**

One of the biggest problems currently faced in the research of TERS is developing a method of creating robust tips that have both the required enhancing factor and the method produces tips consistently and reliably [Bek, 2011].

Methods for fabricating STM/AFM tips have been understood for some time. There is still, however, some difficulty in fabricating a tip which gives a repeatable enhancement. Although most metals have the ability to generate surface plasmons, it is noble metals such as gold, silver and copper that demonstrate the greatest enhancements. Other factors to be considered are the curvature of the tip apex and the aspect ratio.

There are several suggested methods for tip fabrication. For example, Christiansen *et al* have developed a unique method of using gold-capped silicon nanowires grown by vapour-liquid-solid growth. Bin Ren *et al* prefer to use the more common electrochemical etching process [Becker, 2008, Christiansen, 2007, Ren, 2004]. It is also possible to coat the tip using methods such as sputter coating or thermal

evaporation [Saito, 2008]. Each method generates its own yield of tips, which show a suitably sharp apex with the correct radius of curvature. It is important to note that the typical yield published may not be on tips that have been tested but simply those which show the correct geometries when characterised.

The work of S. H. Christiansen *et al* discusses gold-topped silicon nanowires with diameters in the range 50 – 200 nm grown by vapour-liquid-solid growth mechanism. Refer to Christiansen, 2007 for details. The silicon nanowire is welded to an AFM tip using a complex nano-manipulation setup in a SEM. At the time of going to print, the research group had proven the technique's SERS capabilities but not TERS. However, the group are now working on thinner nanowires to improve spatial resolution.

Another consideration is the arrangement of nanoparticles or nanostructures on the tip and the effect this has on the TERS enhancement. In 2000, Brown *et al* propose a method of controlling nanoparticle size and shape by reducing a gold solution onto preformed nanoparticles [Brown, 2000]. Later, Millstone *et al.* report on the fabrication of Au nanoprisms [Millstone, 2005]. The nanoprisms are prepared using seed spherical nanoparticles in an aqueous solution and a mix of spherical and triangular structures are produced with good size control. This size control is important in the fabrication of reproducible tips, however, currently the findings show that only Au is stable and other metals do not yield the same.

With the focus on reproducibility of tips, Shevchenko *et al* look at self ordering nanoparticles [Shevchenko, 2006]. This paper does not look specifically at nanoparticles capable of creating a TERS enhancement, however, shows that highly ordered arrays of nanoparticles are achievable.

As with AFM, STM and other tip assisted methods, the tip material and its geometry will differ depending on the sample and the type of information required from the measurement. Those authors publishing higher tip yields than one might expect are often measuring the Raman spectrum from a carbon nanotube, or organic materials [Hartschuh, 2003]. Both of these samples are highly Raman active and therefore it will be easier to see an enhancement that you would not necessarily see from, say strained silicon. The number of research groups focussing directly on using TERS for Si/SiGe measurements is quite small [Georgi, 2007].

## 2.4. Recent Developments in Raman Spectroscopy

This section has discussed the background and theory to Raman Spectroscopy and related techniques as a method for nanoscale strain characterisation in semiconductors. It has shown that while chemical molecular characterisation using TERS can be a relatively simple task, the task of measuring strain in a strained silicon device is somewhat more difficult.

It is clear from the literature that there are several applications of TERS that do not face the same challenges and limitations of nanoscale strain characterisation. The majority of literature available relating to TERS and silicon is published between 2000 and 2007. More recent publications are much less common, with few since 2009. This is virtue of the fact the technique has proven much more difficult to perfect than could have been predicted. In part, this could be down to a lack of detailed research on what provides the enhancement and what a robust, reliable tip should consist of. Most importantly, publications do not cite reasons for results not being repeatable. Chapter 6 contains further discussion on this point.

The groups focussed on obtaining TERS data from  $\epsilon$ -Si/SiGe stacks or Ge include Hanafusa *et al* [Hanafusa, 2011]. They report on simultaneous TERS and AFM measurements on a  $\epsilon$ -Si cap layer on a SiGe buffer. Here, the results show a slight enhancement of the  $\epsilon$ -Si cap layer, but still show a large peak from the underlying Si substrate showing that surface selectivity has not been achieved.

There are groups focussing specifically on tip fabrication. However, the problem is that what makes a tip suitable for one application does not necessarily make it suitable for others. Already discussed is that it is somewhat easier to get a TERS enhancement from structures such as carbon nanotubes or several chemicals than from a  $\epsilon$ -Si structure. With more sensitive materials as a sample, the need for tips to be reproducible becomes even more paramount. Berweger *et al* discuss selection rules in TERS and highlight the importance and difficulties faced with reproducible tip fabrication with a well defined plasmon resonance [Berweger, 2009].

A few recent publications focus more the setup of TERS equipment and tip optimisation. For example, Merlen *et al* in 2009 [Merlen, 2009] discuss in detail the experimental set up of their system and show repeatable results on a silicon sample. It is

worth noting, however, that enhancement on silicon is easier to achieve than from a  $\epsilon$ -Si/SiGe stack. Depolarization effects on the obtained signal are reviewed in this paper. Also in 2009, Poborchii *et al* completed further study into the possibility of UV TERS [Poborchii, 2009]. Theoretical analysis and SERS experimentation confirm the suitability of Al as an appropriate metal for a TERS tip coating. Only weak enhancements were achieved, however, this is a promising step forward due to the surface selectivity of UV.

The next section will introduce electron backscatter diffraction (EBSD) as a strain characterisation technique. This method uses an electron beam as its radiation source so already has the advantage of the ability to characterise metals. The electron beam has a smaller diameter of an order of magnitude smaller than that of the laser used for Raman Spectroscopy and so has a much-improved spatial resolution, typically sub-100 nm. However, the sensitivity to small changes in material composition, i.e. germanium content, using this technique is significantly poorer than Raman Spectroscopy. The following section will illustrate EBSD to be an excellent calibration tool for Raman Spectroscopy based techniques. For the analysis of the microtexture of copper interconnects, however, EBSD is a very useful technique.

## **2.5. Electron Backscatter Diffraction**

Electron backscatter diffraction (EBSD) a well documented technique that is used extensively as a tool for crystallographic and microstructure and microtexture analysis such as phase and strain identification [Randle, 2008]. The process is done by analysis of Kikuchi patterns that are specific to the material being analysed and are affected by parameters such as grain orientation and strain. EBSD is an extension of the scanning electron microscope (SEM) and has a high spatial resolution making it suitable for analysis of very small specimens. It has the advantage of being non-destructive with no sample preparation necessary. The SEM is capable of taking large samples and spatial resolution is improving with the introduction of new technology such as field emission gun SEMs (FEGSEM). However, for some smaller and for semiconducting samples, the signal obtained can be problematic as the signal to noise ratio worsens to the extent of not gaining a reliable pattern. The background and development of EBSD will be covered in this section as well as how it can be used as a high spatial resolution strain

sensor in both semiconductors, specifically  $\epsilon$ -Si/SiGe as well as copper interconnects used in modern microelectronics.

### **2.5.1. Background**

Around the same period of time as Raman's discovery of inelastic light scattering, the first pattern from 'reflected' electrons was also observed. In the 1930s, patterns were observed from single crystal samples [Randle, 2008] and these patterns were branded Kikuchi bands. The patterns are made up of a series of lines formed by diffracted electrons associated with Bragg diffraction from one side of a single set of lattice planes.

From then, EBSD has continually been developed further and these developments are briefly discussed here. It wasn't until the 1950s that EBSD took a major step forward due to the invention of equipment capable recording patterns in the form of a hard copy on cut film [Alam, 1954].

The Scanning Electron Microscope, on which EBSD is based, was emerging as a major characterisation tool and the attachment of a video camera to the SEM in the 1970s allowed the first electron backscatter patterns (EBSPs) to be recorded. Further development in the 1980s allowed EBSD to be used as a microtexture analysis tool [Randle, 2008] by allowing the user to identify zone axes on the sample and allowing software to calculate grain orientation. By the 1990s, automated indexing was common place and EBSD was a dominant tool in the area of microtexture analysis.

### **2.5.2. Strain Analysis Using EBSD**

For elastic strain determination such as the strain present in the devices, the pattern the Kikuchi bands form are used. Images of these Kikuchi bands are shown in figures 2.4 a and b below. The differences in the angles between the bands is measured for strained and unstrained silicon. Because the strain is so low, the difference is difficult to see.

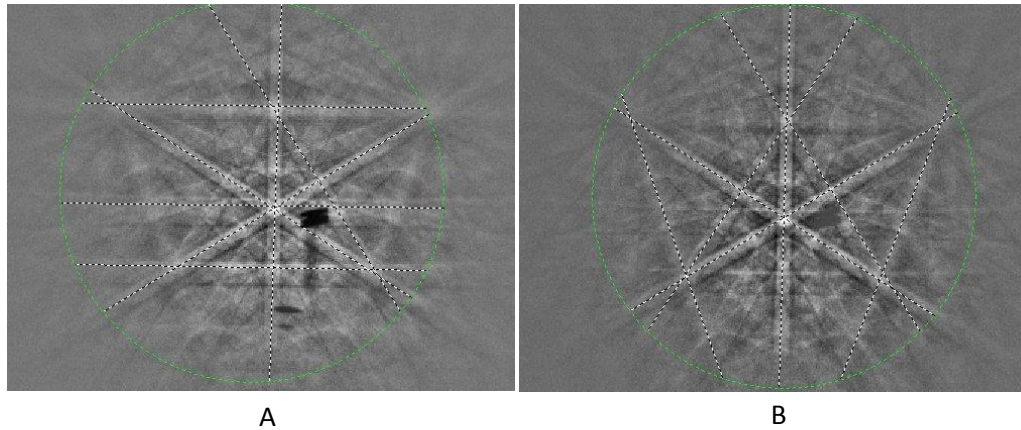


**Figure 2.4. Kikuchi bands of A) unstrained and B) strained silicon**

A Kikuchi pattern consists of pairs of pairs of parallel lines called Kikuchi bands. Each band has a distinct width and corresponds to a crystallographic plane [Randle, 2008]. In the case of constant elastically  $\epsilon$ -Si, the Kikuchi bands are modified somewhat. A tensile strain would cause an increase in interplanar spacing and the Bragg angle would decrease. This would lead to a decrease in Kikuchi bandwidth [Keller, 2004]. The method of determining strain by EBSD has an uncertainty of about 0.2%. Non uniform strain such as that which may be observed along the length of the transistor channel would manifest itself as an increase in band width and a loss of pattern sharpness. For this reason, currently only an average strain can be measured as with conventional Raman Spectroscopy.

Work by Angus Wilkinson [Wilkinson, 2006] provides a thorough and effective method of using EBSD to measure the strain tensor of a strained silicon sample. This was followed up by Kacher *et al* in 2009 [Kacher, 2009] as simulations. As discussed earlier in this chapter, Raman spectroscopy does not measure strain, but gives information about the vibrational modes of the crystal lattice which can then be converted to a strain value. In this way, much information about the strain tensor is lost, however, for an industrial setting, the information gained is perfectly adequate. The method proposed by Wilkinson *et al* is highly accurate, however, it is complex and somewhat difficult to achieve. Where simplicity and speed of measurement are important, the Wilkinson method is currently not suitable as an industrial measurement technique.

Using imaging software to measure the relative widths of the bands and calculating a percentage value for strain similar to that measured with Raman spectroscopy is a much more simple technique that gives results adequate for the semiconductor industry. Another possibility to give an order of magnitude greater accuracy would be to use a

similar technique using the higher-order Laue zone (HOLZ) ring, depicted by the green outline in figure 2.4. This technique was proposed by Langer [Langer, 2007] and more detail can be found in the referenced paper. Although this method is an attractive one as it is more straight forward and requires no sample preparation, it still requires a great deal of effort to achieve a result. Consequently, it is not currently worth pursuing as a replacement to Raman spectroscopy but provides a good means to calibrate Raman results.

## **2.6. Summary**

This chapter has detailed current techniques and the challenges faced with them. While TERS remains a promising new technique to replace conventional Raman spectroscopy [Hayazawa, 2004], the problems with creating a robust and reliable tip mean this is likely to still be some way off. EBSD is theoretically an alternative to Raman spectroscopy, it is non-destructive, can be done in situ and can be shown to give comparable results, however, its use in an industrial setting seems unlikely for strain measurement at present. EBSD is a powerful tool for microtexture analysis of crystalline structures, and it is this use that will help give an understanding of BEOL processing.

The next chapter outlines the instrumentation employed throughout the investigations in this thesis.

## Chapter 3. Instrumentation

### 3.1. Introduction

The previous chapter looked in some detail at the techniques adopted throughout this thesis and their current applications in science and technology. The set ups of these techniques will be outlined in this section along with an overview of machine configuration and basic operation.

### 3.2. Raman Spectroscopy Instrumentation

A LabRAM HR800, figure 3.1, from the company Horiba Jobin Yvon was adopted throughout this investigation. This system is an integrated spectrometer and confocal microscope. It briefly comprises of the laser source, a diffraction grating/spectral analyser, confocal microscope and a detection system.



**Figure 3.1. LabRAM HR800 [Horiba Jobin Yvon, 2008]**

A Horiba Jobin Yvon LabRam HR 800 with two laser lines was used, a tuneable argon laser in the visible spectrum and an argon UV line. The visible is capable of 514 nm (green), 488 nm (blue) and 457 nm (purple) outputs. The UV laser output is 364 nm. The laser used depends on the sample being examined and largely on the penetration depth required. For microelectronic material characterisation, i.e. silicon or strained silicon (SiGe), UV is best because it has a resonant effect with the sample, thus increasing the signal and improving the signal to noise ratio.

#### 3.2.1. LabRAM HR800 setup and operation

The LabRam HR800 is shown in figure 3.1. A schematic of a typical set up is shown in figure 3.2 and the optical path of the UV and visible lasers is shown in figure 3.3.

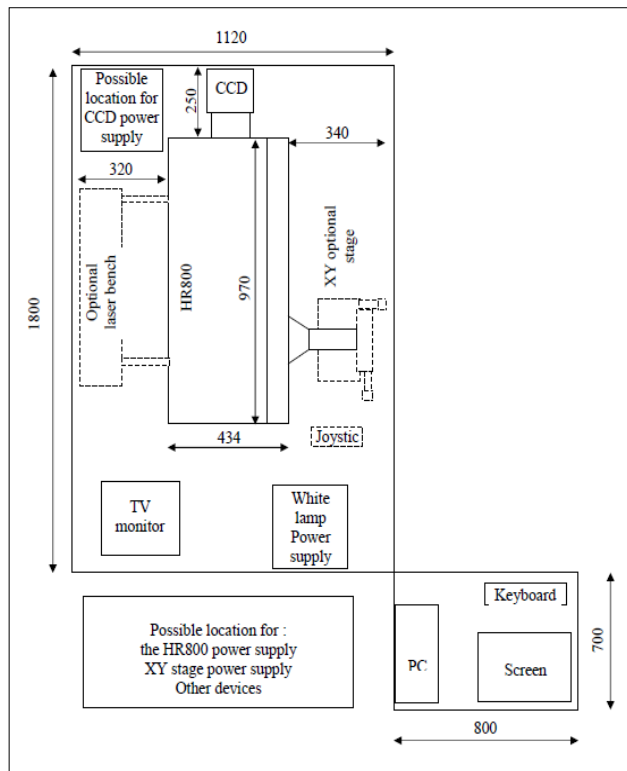


**Figure 3.2. Schematic of typical LabRAM HR800 set up**

The system is calibrated with a high quality single crystal Si sample. Si has a strong characteristic Raman peak at  $520\text{ cm}^{-1}$  and so is ideal for calibration. The sample is placed on the stage and focused using the optical microscope and typically, the 100 x magnification objective. Once the sample is illuminated by the laser, the reflected photons are collected through the same objective lens as the equipment is set up in backscattering configuration. There is a sensitive CCD detector to collect the signal that can then be analysed through the LabSpec software.

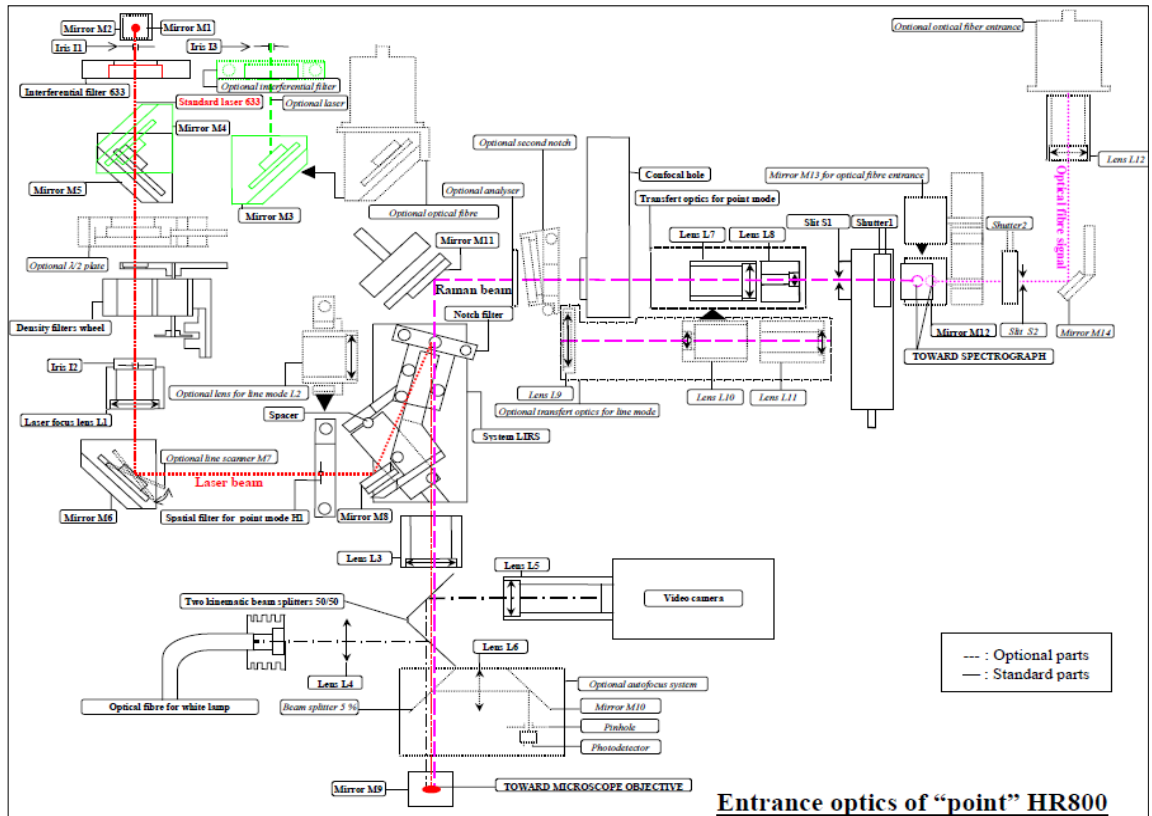


**Figure 3.3.** In depth schematic of the optical path in the LabRAM HR800. The schematic shows the path of both the tuneable visible laser and the argon ion UV laser [Horiba Jobin Yvon, 2011]

The individual components of the Raman microscope are discussed below.

### 3.2.1. Confocal Microscope

The confocal microscope is an integral part of the LabRAM HR800 system. A confocal microscope is simply a set of two lenses where the light from the focal point of one lens is focused onto the focal point of the other, shown by the solid line in figure 3.4. The pinhole allows light from this line through and the screen blocks most of the light from any other point, depicted by a dashed line. This means that the image from any point other than that allowed by the pinhole will be severely attenuated [Semwogerere, 2005, Sheppard, 1997].

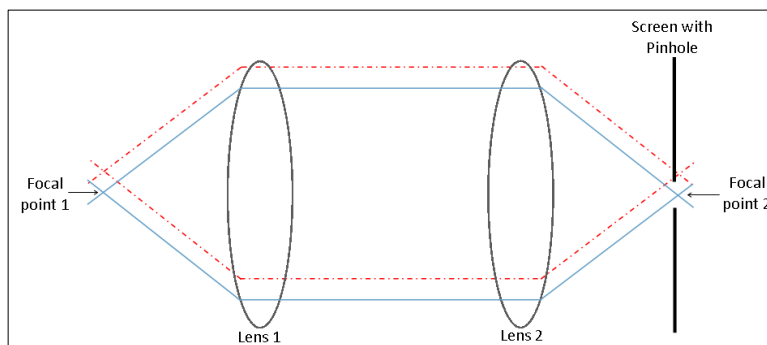


**Figure 3.4.** Depiction of the lens in a confocal microscope

### 3.2.2. Excitation Source and Diffraction Grating

The Raman scattered light is affected by the size/type of sample and the intensity of the exciting light. The latter of these factors is controlled by the nature of the exciting source. Different sources will give different characteristics.

Using a laser as a source has been a popular choice since 1960 [Tobin, 1971]. Advances in laser technology means that improvements in the results obtained from Raman spectroscopy increased rapidly. New challenges in the modern day have arisen from other limitations such as the scale of the sample to be measured. The laser is the most ideal source to date due to its characteristics. The spot size of the laser can be reduced to less than  $0.5\mu\text{m}$  which improves the spatial resolution. It is also a highly directional, intense monochromatic light source. The HR800 has several laser excitations to choose from. There is an external argon ion laser which is a tuneable laser source that uses ionised gas as the lasing medium. The argon in a sealed cavity forms a plasma. The high current density and the energy level transitions generate a large amount of heat which is water cooled. A full description of ion lasers is given by Bridges *et al* [Bridges, 1971]. Changing the excitation wavelength, i.e. tuning the laser to a different frequency, requires changing the notch filter as these are specific to one wavelength. Notch filters are briefly described below.

A diffraction grating is an optical device which consists of closely spaced, ruled, parallel narrow slits or grooves which diffract light to produce a spectrum. There are typically several thousand per cm. The HR800 is equipped with two gratings, 2400 and 3000. The low density grating is capable of complete spectral coverage in one measurement while the high density grating has a much higher spectral resolution with the ability to detect very small changes in the sample material.

As Raman radiation is already so weak, the system must be free of any stray light. Stray light can be caused by leakage through system housing, light entering through entrance slits that does not come from the sample and reflection at the surface of optics.

Optical filters are in place to prevent the laser light from overshadowing the reflected Raman light. There are notch filters in place between the sample and the spectrometer. A notch filter is also known as a band-stop filter that severely attenuates light of a specific wavelength, or small range of wavelengths to very low levels. In Raman

spectroscopy, these notch filters block the Rayleigh scattered light and ensure a clear Stokes scattered signal is collected [Puppels, 1990].

### 3.2.3. TERS setup

Figure 3.5 below shows the TERS set up employed at Newcastle consisting of the HR800 combined with a Park Systems AFM. It is possible to change the laser path from the Raman microscope to illuminate the AFM cantilever using an off axis configuration as illustrated in figure 3.6.



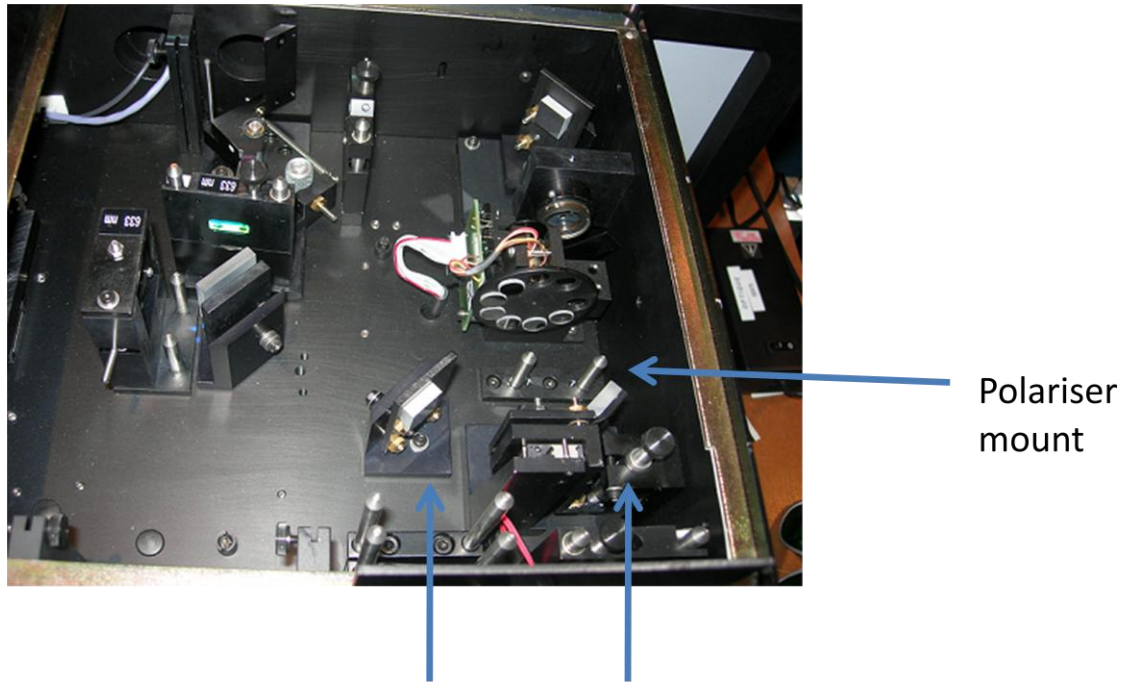
**Figure 3.5. Combined AFM/Raman TERS system consisting of LabRAM HR800 coupled with a Park Systems AFM [Horiba Jobin Yvon, 2011]**

While the system is still in back scattering mode, the off-axis coupling sets the Raman microscope objective to an angle such that there is no shadowing effect from the AFM cantilever and is the best configuration where large sample are to be analysed, however. having the objective at such an angle weakens the Raman signal collected.



**Figure 3.6. Depiction of off-axis coupling where the Raman microscope objective is set at an angle such that there are no effects from the AFM cantilever. The Raman microscope is still in back scattering mode [Horiba Jobin Yvon, 2011]**

On initially setting up the system, with the AFM tip away from the sample surface, the Raman microscope is set up to achieve the largest possible far-field intensity. Once this is achieved, a polariser inserted into the main body of the machine, as shown in figure 3.7, effectively blocks this far-field signal.



Rear of the instrument, laser entrance

**Figure 3.7.** Main body of instrument depicting polariser mount. The polariser is used to block any far-field signal ensuring all the collected signal is that which is enhanced due to the presence of the AFM tip.

When the AFM tip is brought close to the sample surface, having blocked the far-field signal, the resultant spectra are entirely from the region directly underneath the tip apex, with no contribution to intensity from the far-field.

### 3.3. Electron Backscatter Diffraction

EBSD was carried out in a FEI XL-30 ESEM FEG (Field Emission Gun) equipped with EBSD hardware and software from HKL Technologies shown in figure 3.8. EBSD is a SEM based technique that utilises the electron gun with tungsten filament and optical column capable of tuning the electron beam to a fine spot in the order of nanometres. In SEM operation, the electron beam is scanned in a raster pattern across the region of interest on the sample surface to create a high resolution image.



**Figure 3.8. FEI XL-40 ESEM**

For EBSD operation, extra software and hardware is required. The principle components of the EBSD set up are shown in figure 3.9.

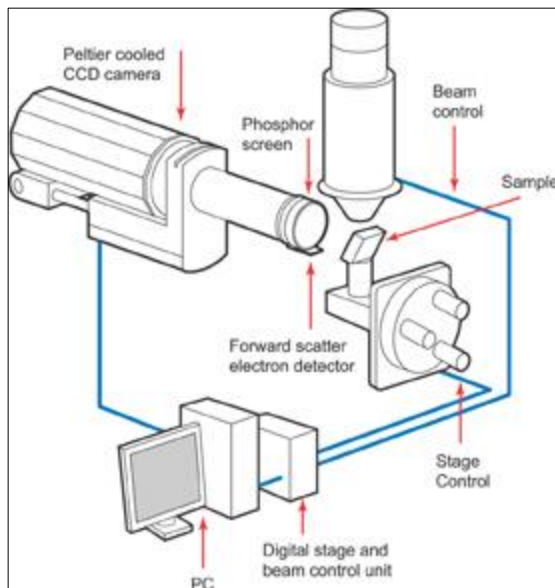


**Figure 3.9. Schematic showing the principle components of EBSD**

The sample is mounted on the stage and tilted at a high angle, approximately  $70^\circ$ , so that the angle between the beam is small ensuring maximum signal intensity. The working distance between the sample and beam is also small at 20 – 25 mm.

During operation, the phosphor screen is fluoresced by electrons diffracted from the sample. This forms a diffraction pattern on the screen. The image of the EBSP is acquired from the sensitive CCD camera that interfaces with the software on the PC. This allows for automated image analysis.

Calibration is important in EBSD as crystalline, cubic materials may look very similar and for the purposes of grain orientation, it is essential that the software knows which material it is analysing. Calibration is undertaken every time a new measurement is taken. The main parameter looked at is mean angular deviation, MAD. Once an EBSD has been obtained, Kikuchi bands are fitted and compared against the known Bragg angles. The deviation between the known angles and the fitted angles should be as small as possible and always less than  $0.5^\circ$  for the greatest accuracy.

### **3.4. Summary**

The two main techniques adopted throughout this thesis are described in this chapter. The Raman microscope is a LabRAM HR800 from Horiba Jobin Yvon. It has two laser lines, a tuneable visible laser and a UV laser. EBSD takes place in a Philips XL40 ESEM.

Chapter 4 focuses on the importance of calibration of a Raman microscope and details many of the main sources of variation and the effect they can have on the data collected.

## **Chapter 4. Raman Calibration**

### **4.1. Introduction**

When characterising at the submicron or nanoscale, it is difficult to be certain of what is being measured. Calibration, therefore, is of paramount importance in order to minimise impact from external factors affecting the data gathered [Rath, 2003]. For example, Raman spectroscopy uses lasers in the visible or near visible region of the spectrum, with the smallest laser spot size being in the order of half a micron; it is already difficult to be certain of the precise region of measurement. Couple this with the fact that every machine will vary depending on lab conditions, temperature, electrical noise etc, it becomes clear that careful and regular calibration is required for purposes of repeatability and reproducibility.

Strain calculations from Raman measurements vary greatly in literature. Empirical calculations based on the equipment available are paramount for the reasons cited above. A comparison of these curves is outlined below.

Calibration is equally important in other measurement techniques employed throughout this thesis, i.e. EBSD and nanoindentation. However, the calibration of these techniques is less complex and is covered in their respective results chapters.

### **4.2. Raman Spectroscopy for Strain Analysis**

The samples used in the following sections were Si/SiGe structures as per figure 4.1 with varied Ge composition, 0 – 30%. The layers were deposited using ultra low pressure chemical vapour deposition (CVD) in modified molecular beam epitaxy (MBE) with a deposition temperature of 650°C (Strained Si - 600°C) [Dobrosz, 2006]. The devices were etched from the surface prior to measurement. The measurements were taken on the LabRAM HR800 system from Horiba Jobin Yvon (HJY) described in chapter 3. For the purposes of the reference spectra below, the system was set up as follows:

- 514.5 nm laser power: 1.1 mW
- 457.9 nm laser power: 1.57 mW
- Aperture: 300  $\mu\text{m}$
- Slit: 100  $\mu\text{m}$
- Acquisition Time: 6 s

- Accumulation Number: 3
- Grating: 2400

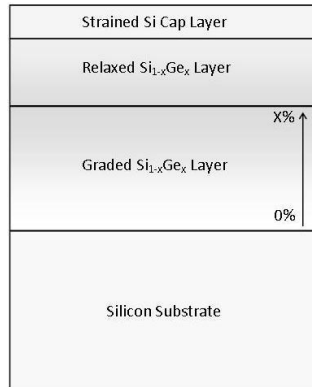


**Figure 4.1. Schematic of samples used in this investigation. Samples had varying Ge composition, 0 – 30%. Devices were etched from the sample surface prior to measurement [Dobrosz, 2006]**

### 4.3. Silicon Reference Spectrum

Failure to calibrate correctly will result in inaccurate data gathered, hence the already difficult to analyse SiGe spectrum may be incorrect leading to erroneous values of strain. A good quality single crystal silicon sample was used for the calibration.

Silicon (100) has a characteristic peak between 520 and 521  $\text{cm}^{-1}$  [De Wolf, 1996]. The peak position of any sample can be affected by several factors. The temperature of the room in which the sample was measured and hence the temperature of the sample itself has been shown to have a significant effect on the peak position with an increase in temperature at the sample surface of only 1°C can shift the peak by as much as 0.025  $\text{cm}^{-1}$  [De Wolf, 1999]. Temperature at the sample surface is also affected by the energy and power of the excitation source. Regular calibration ensures that problems are quickly detected and the best quality data is acquired where the sources of variation are minimised. Figure 4.2 shows a typical peak from single crystal silicon.

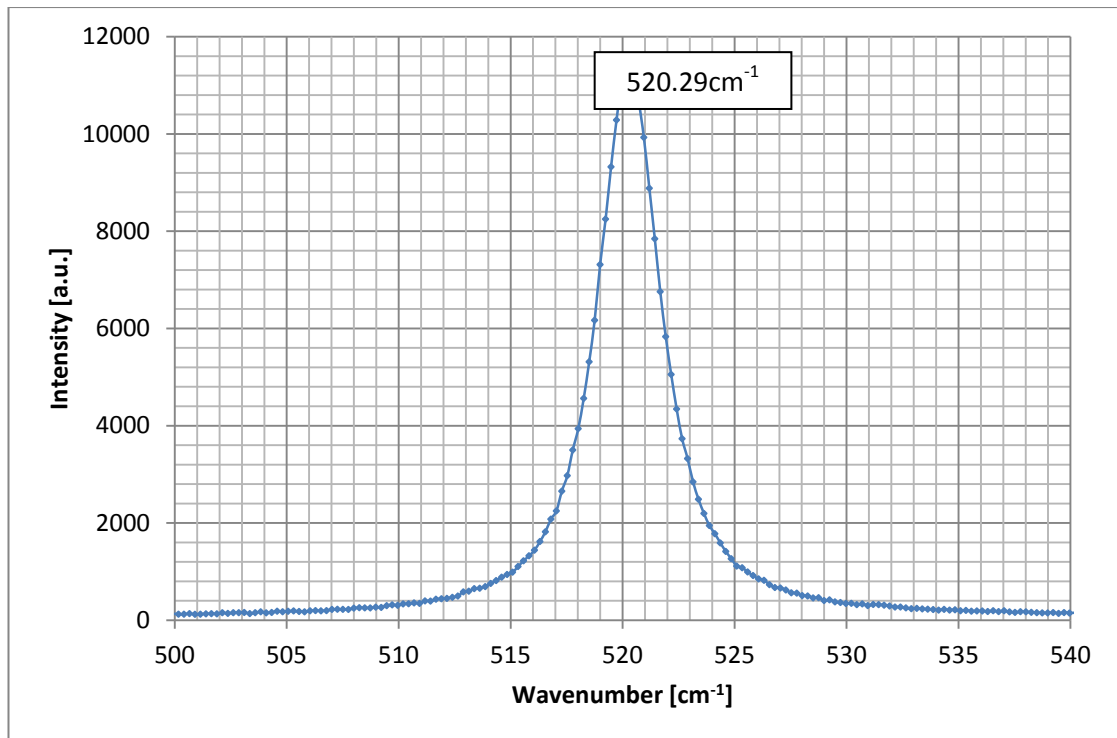


**Figure 4.2. Silicon reference spectrum. Single crystal silicon has a characteristic peak of  $520.7 \text{ cm}^{-1}$ . However, typical values lie between  $520 - 521 \text{ cm}^{-1}$  [De Wolf, 1996].**

#### **4.3.1. $\text{Si}_{1-x}\text{Ge}_x$ Spectrum**

An increase in germanium content leads to an increase in strain in the strained silicon cap layer of the device. This also causes a shift in the peak position from the silicon bonds in the silicon germanium. Figure 4.3 shows the difference in peak position between Si and  $\text{Si}_{0.7}\text{Ge}_{0.3}$  to be approximately  $18 \text{ cm}^{-1}$ . This significant difference allows a reasonably accurate estimate of the Germanium content in a sample based on its peak position using a calibration curve, discussed later in this chapter.

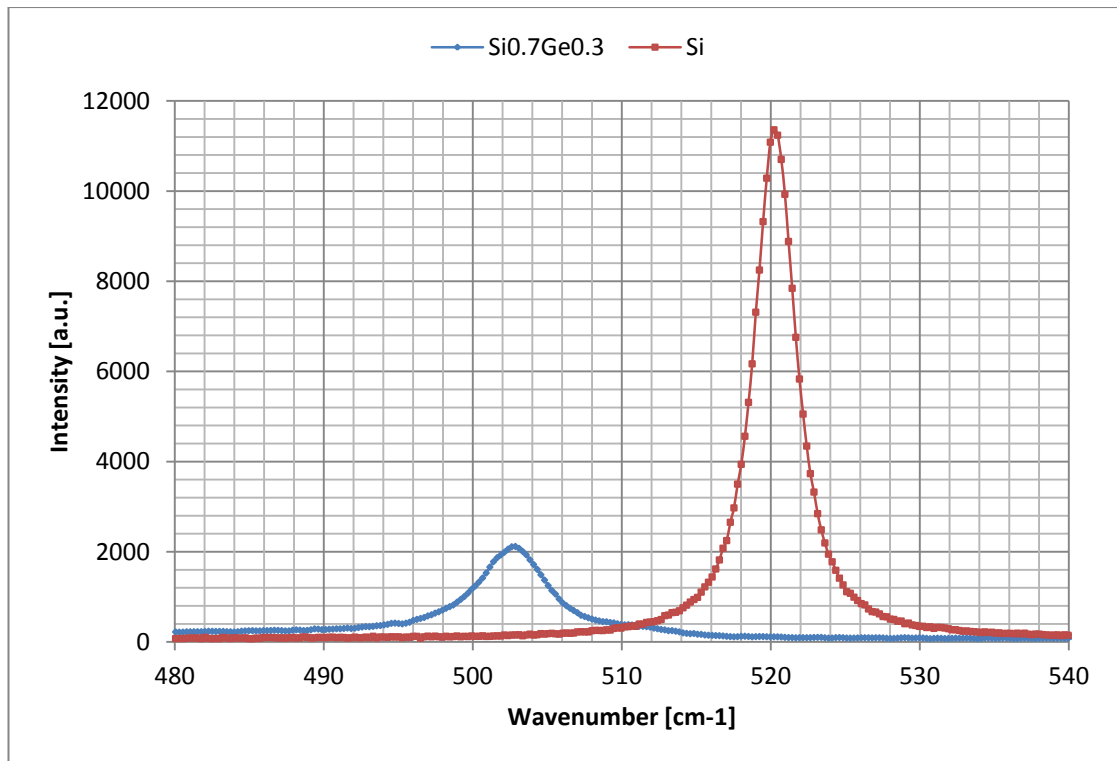


**Figure 4.3.** Depicts the difference in peak position between single crystal silicon and  $\text{Si}_{0.7}\text{Ge}_{0.3}$  as being approximately  $18\text{cm}^{-1}$ . This difference allows an estimation of the Ge content of a sample using the peak position as a reference.

The spectrum in figure 4.4 was taken using a 457.9 nm excitation laser at 25% power, ~1.57 mW.

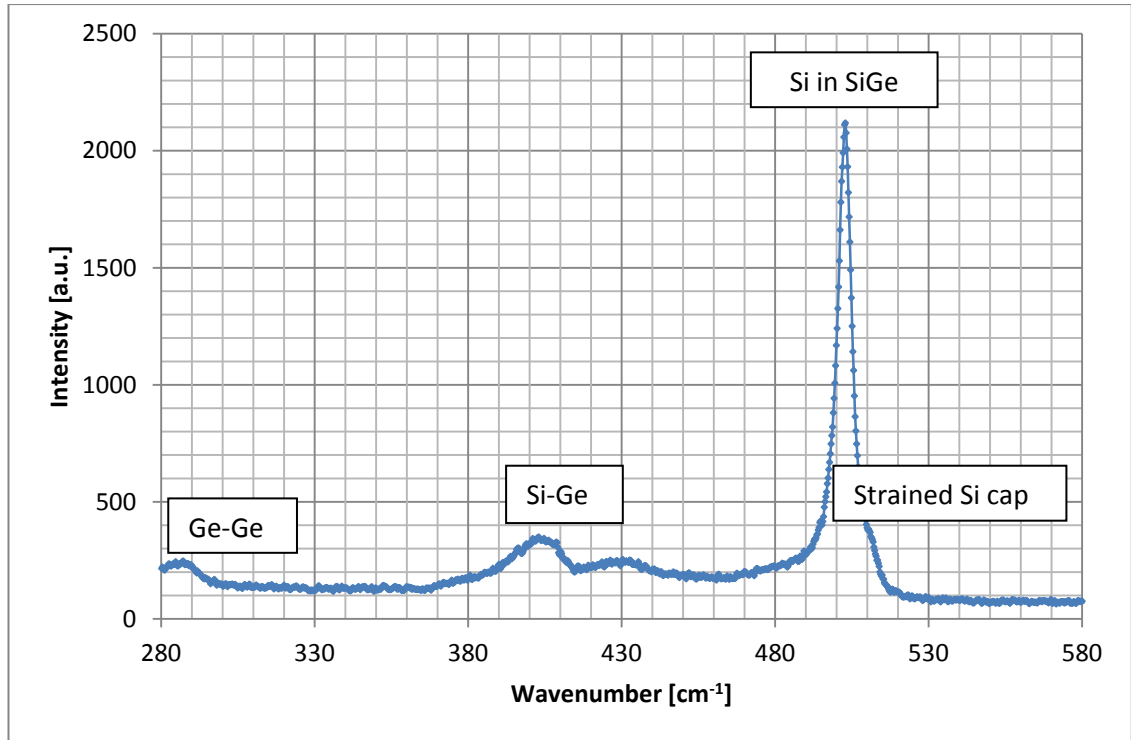


**Figure 4.4.** Typical peaks in a strained silicon sample with the structure depicted in figure 4.1. The strained silicon cap layer manifests itself as a small, difficult to analyse shoulder on the high wave number side of the much higher intensity Si in SiGe peak. The sample used to obtain the above spectrum is Si<sub>0.7</sub>Ge<sub>0.3</sub>. The excitation source is a 457 nm laser at approximately 1.57 mW power.

The SiGe spectrum shows four characteristic peaks. The peak at around 280 cm<sup>-1</sup> is the Ge-Ge bonds in the relaxed SiGe virtual substrate. The second peak near 400 cm<sup>-1</sup> is from the Si-Ge bonds. The most prominent peak is due to the Silicon bonds in the SiGe. This peak will vary between ~500 – 521 cm<sup>-1</sup>, depending on the Ge content. The position of this peak can establish the Germanium content in the sample. The fourth peak is the most difficult to see. This peak will quite often manifest itself as a small bump on the high wavenumber side of the Si in SiGe peak. The amount of strain in the system determines where this peak falls; tensile strain will cause a shift to a lower wavenumber, compressive strain will cause a shift to a higher wavenumber.

#### 4.4. Calibration Curve: Theoretical, Experimental and from Literature

Spectra were taken for the samples containing from 0 – 30 % germanium using the conditions mentioned earlier in this chapter. The peak positions were obtained using the peak fitting software supplied with the LabRAM HR800 system. Several spectra were taken from each sample several times to ensure repeatability and the results obtained were all within ~0.3 cm<sup>-1</sup>.

From the peak positions of the Si in SiGe bonds and the strained Si cap layer, it was possible to draw a curve of expected peak positions for a given germanium content. Shown below in figures 4.5 - 4.7 are the calibration curves acquired from three different laser lines, 364, 457 and 514 nm. There is a noticeable shift in peak positions between the curves, which can be explained by the differing penetration depths, detailed in the next section. The 514 nm laser will penetrate furthest into the sample, into the underlying graded SiGe layer. The peak position seen will therefore be an average over the whole of the depth probed. Even with the 457 nm line, there is still more scope for error in the data obtained when looking at the strained silicon cap layer in particular. The most accurate data comes from the 364 nm laser, which only gives information from the top few nanometres of the sample surface. The differences in the results below are likely to be due to experimental error with a small contribution from the varying penetration depths.

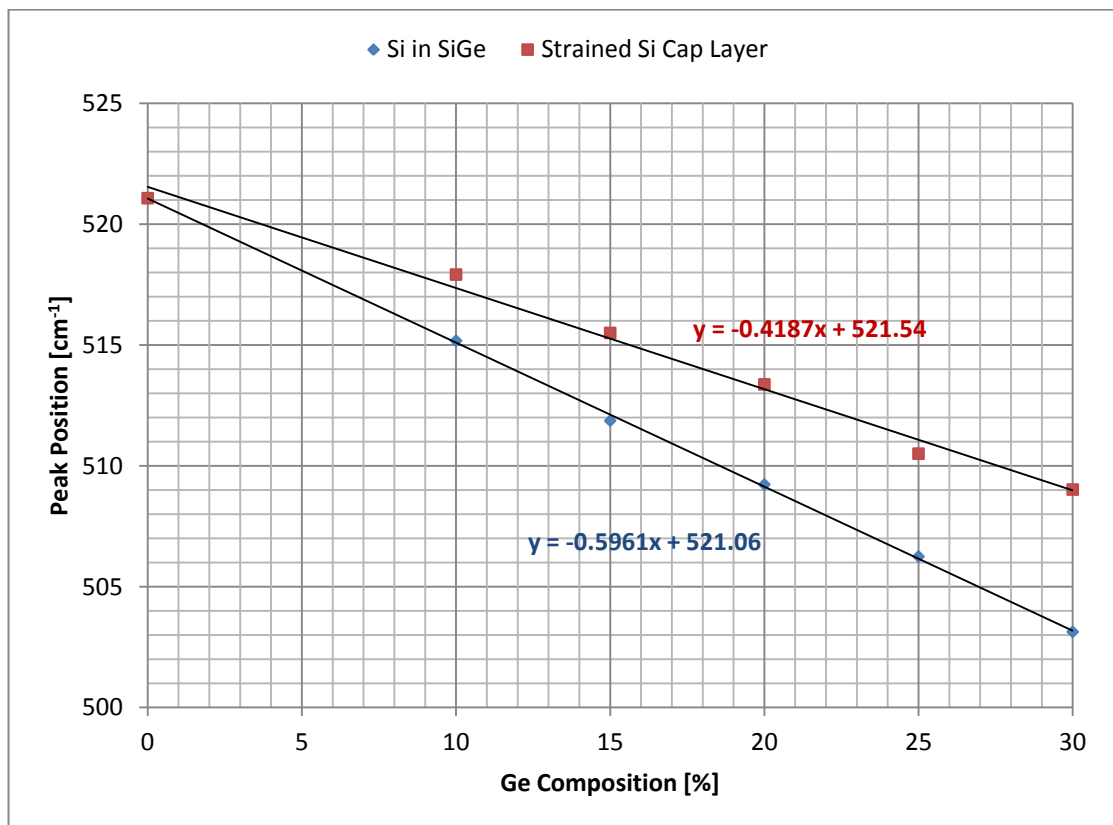


Figure 4.5. Strained Si cap peak position and the Si-Si in SiGe bonds versus Ge Content for 514.5nm (green) laser at 1.1mW power

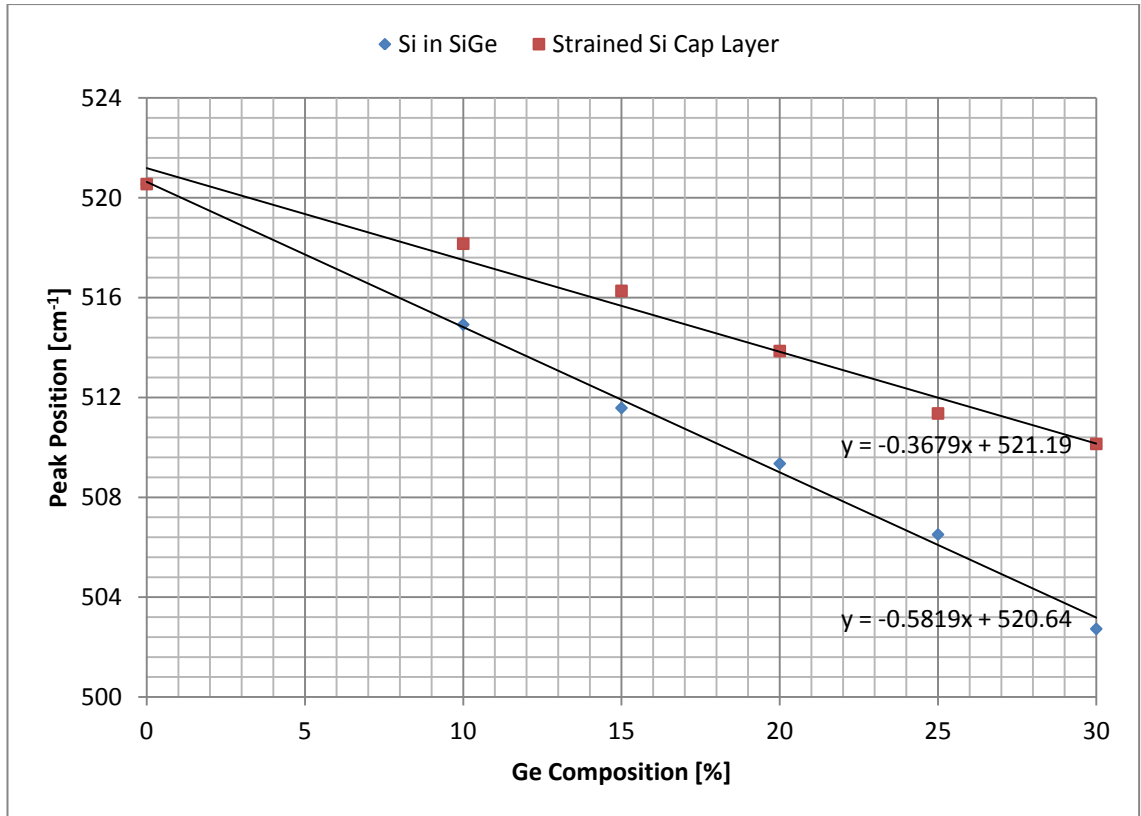


Figure 4.6. Strained Si cap peak position and the Si-Si in SiGe bonds versus Ge Content for 457.9nm (blue) laser at 1.57mW power.

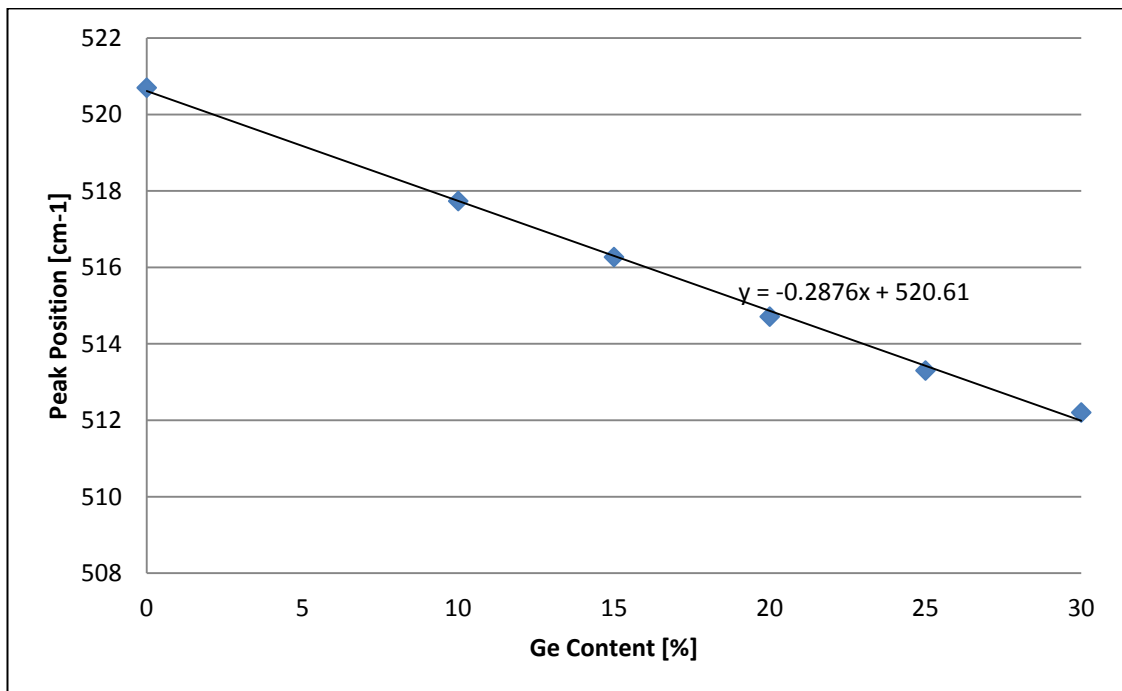


Figure 4.7. Strained Si cap peak position versus Ge content for 364 nm (UV) laser

#### 4.4.1. Theoretical and Literature Calibration Curve

Values depicted on calibration curves vary greatly throughout literature, along with the methods of obtaining them. This section looks in detail at the differences between

theoretical peak position values and those found both in literature and through the experimental work reported in this chapter.

There are Raman modes related to Si-Si, Si-Ge and Ge-Ge bonds in a SiGe structure. The frequencies of these modes are dependent on the Ge content and on any strain present in the SiGe layers. The following relationships apply [Kasper, 1995]:

$$\omega_{\text{SiSi}} = 521 - 68x - 815\varepsilon// \quad (4.1)$$

$$\omega_{\text{SiGe}} = 399.5 + 14.2x - 575\varepsilon// \quad (4.2)$$

$$\omega_{\text{GeGe}} = 282.5 + 16x - 385\varepsilon// \quad (4.3)$$

Where  $\omega_{\text{SiSi/SiGe/GeGe}}$  is the peak position and  $\varepsilon//$  is the strain value. There is debate surrounding the exact values of the constants [Kasper, 1995]. This is a major source of variation between calibration curves calculated from published literature. The theoretical compressive/tensile strain curves were calculated as follows:

Using Vegard's Law, the lattice constant of SiGe [Dismukes, 1964]:

$$a_{\text{Si}_{1-x}\text{Ge}_x} = (1-x)a_{\text{Si}} + xa_{\text{Ge}} \quad (4.4)$$

where x is the Ge%

The strain is calculated as follows:

$$\varepsilon = (a_{\text{sub}} - a_{\text{epi}})/a_{\text{epi}} \quad (4.5)$$

where  $a_{\text{sub}}$  is  $a_{\text{Si}}$  and  $a_{\text{epi}}$  is  $a_{\text{Si}_{1-x}\text{Ge}_x}$

The difference in peak position from the Si peak is calculated as follows:

$$\Delta\omega = b\varepsilon \quad (4.6)$$

where b is the strain shift coefficient in  $\text{cm}^{-1}$

The value for b used here is  $-832\text{cm}^{-1}$  but these values vary in literature from  $\sim 700 - 900 \text{cm}^{-1}$  [Kasper, 1995].

x	a(SiGe)	Theoretical Strain ( $\epsilon$ )	$\Delta\omega$ (Si in SiGe)	Compressive Strain $\omega$ (Si in SiGe)	Tensile Strain $\omega$ (Si in SiGe)
0.1	0.5453	-4.218E-03	3.509	524.209	517.191
0.2	0.5476	-8.400E-03	7.140	527.840	513.560
0.3	0.5499	-1.250E-02	10.400	531.100	510.300
0.4	0.5522	-1.670E-02	13.894	534.594	506.806
0.5	0.5545	-2.070E-02	17.222	537.922	503.478
0.6	0.5568	-2.480E-02	20.634	541.337	500.066
0.7	0.5591	-2.880E-02	23.962	544.662	496.738
0.8	0.5614	-3.280E-02	27.290	547.990	493.410
0.9	0.5637	-3.670E-02	30.534	551.234	490.166
1	0.5660	-4.060E-02	33.779	554.479	486.921

**Table 4.1. Theoretical strain values for Si<sub>1-x</sub>Ge<sub>x</sub> where x is 0 – 100 %**

Figure 4.8 and table 4.1 depicts theoretical peak positions for Si-Si in SiGe bonds for compressive and tensile strained SiGe systems. There is little difference between these theoretical values and experimental values. The individual data lines on this graph are explained in more detail in this section.

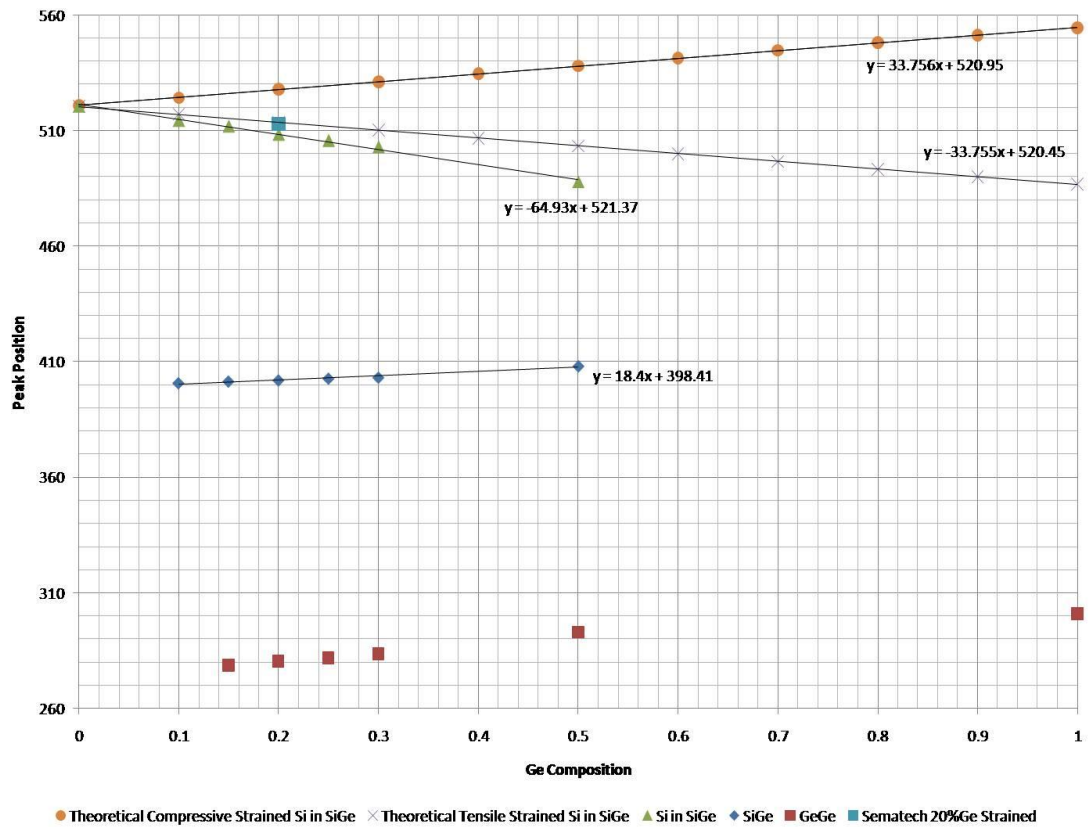


Figure 4.8. Theoretical and experimental peak positions for a fully relaxed SiGe sample

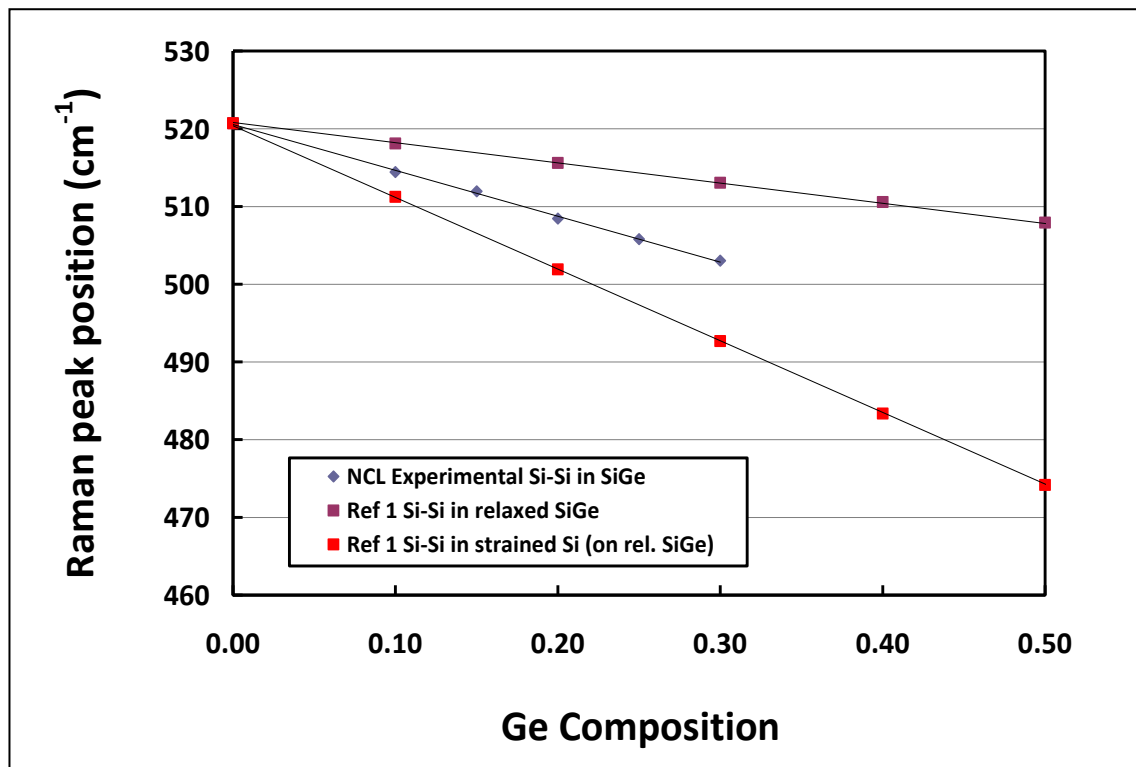


Figure 4.9. Raman peak position versus Ge composition comparing NCL experimental data with data found in literature using similar samples of fully relaxed SiGe. [References from Kasper, 1995]

Figure 4.9 demonstrates experimental results do not agree with literature data. However, the literature data is not universal, and illustrates the importance of individual

calibration of each Raman system. Figure 4.10 shows the full calibration curve for all bonds in the fully relaxed SiGe layer. Using the calibration lines shown in this chapter it should be possible to predict the level of strain in a SiGe layer that is not fully relaxed.

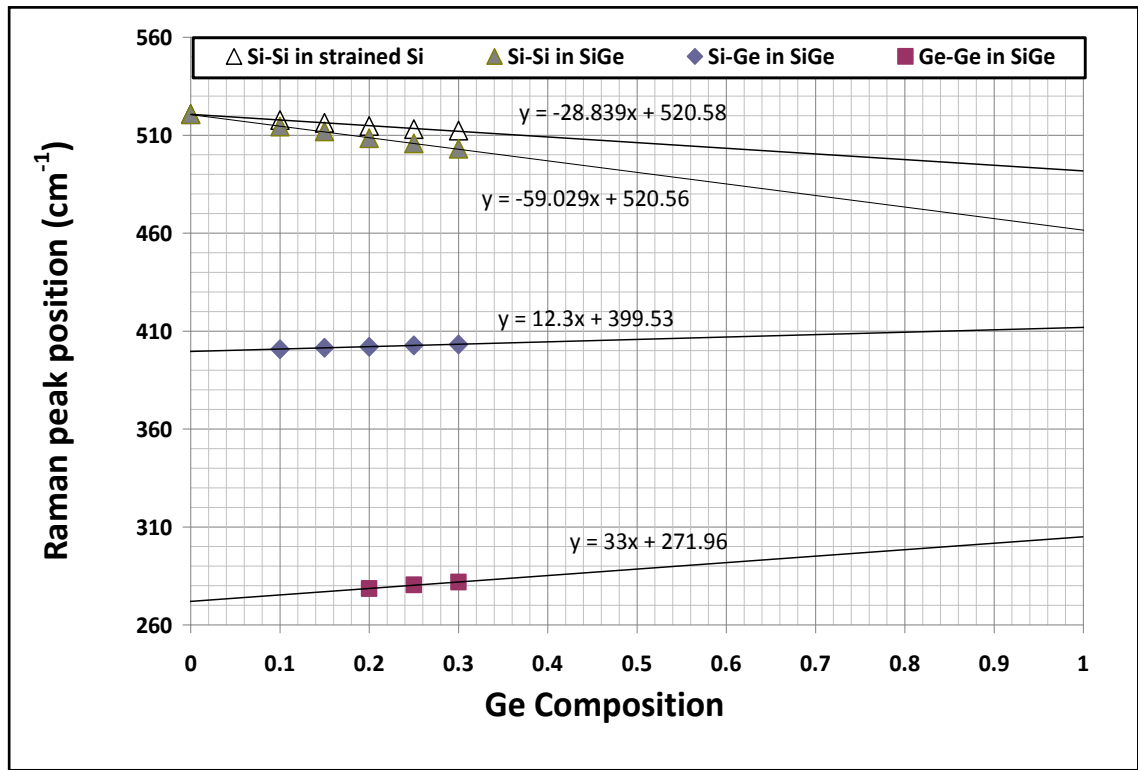


Figure 4.10. Data points from Si-Si, Si-Ge and Ge-Ge bonds in relaxed SiGe layers.

The samples used in figure 4.10 are as depicted in figure 4.1. The layers are fully relaxed as confirmed by XRD (X-Ray Diffractions) and the Ge content was confirmed by SIMS. It appears as though the Ge-Ge trend is not linear; instead, it flattens out at high Ge, however more data is required to prove this.

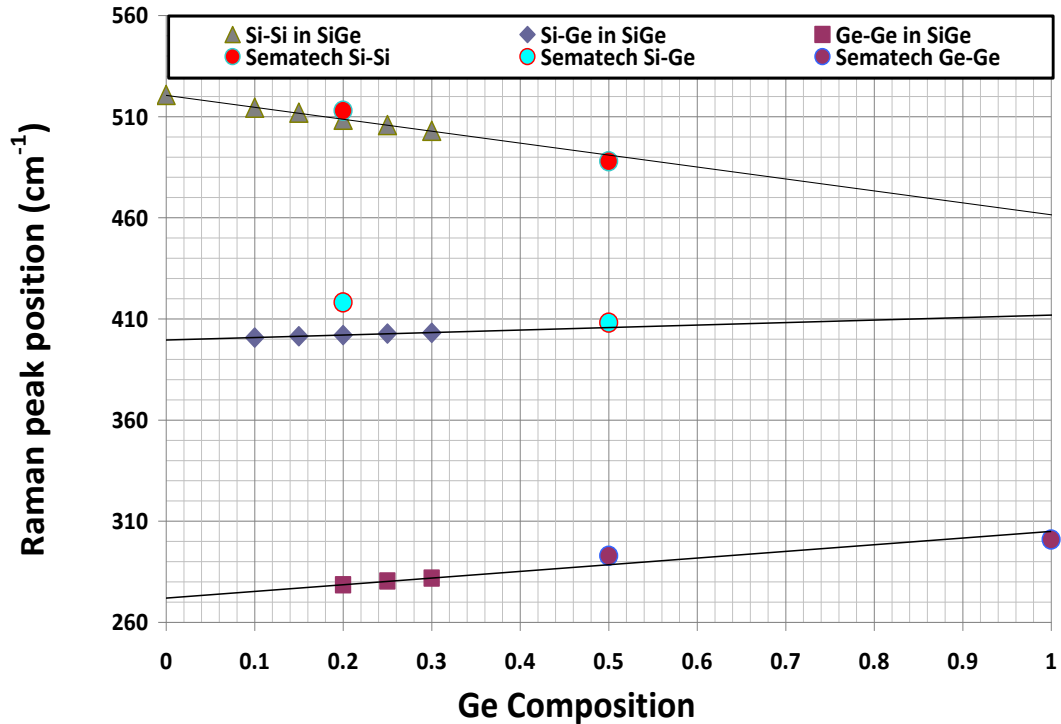


Figure 4.11. Peak position versus Germanium content for samples with residual strain in the SiGe layer [Sematech]

The thicknesses SiGe layers of the Sematech samples used here are as follows:

- 25 nm Si<sub>80</sub>Ge<sub>20</sub>
- 25 nm Si<sub>50</sub>Ge<sub>50</sub>
- 40nm Ge<sub>100</sub>

It is likely that in layers at these thicknesses, full strain relaxation has not occurred. From figure 4.12, 20% Ge gives higher Si-Si and Si-Ge peaks than calibration lines, indicating compressive strain in the SiGe layer. The sample with 50% Ge has peaks close to the calibration line indicating partial relaxation has occurred in this sample. However, in the slightly thicker 100% Ge sample, if a linear calibration line is used, then this indicates full relaxation has occurred in this layer.

These results in part answer the question of whether compressive (or tensile) strain can be quantified using a calibration curve. The data gathered suggests it is possible; however, a calibration line for a fully strained material must first be constructed as a further point of reference. This should also be done for Si-Si, Si-Ge and Ge-Ge bond vibrations.

#### 4.5. Effect of Heat and Laser Power

The choice of excitation source has a huge effect on the data gathered. The quality of spectra and information that can be gleaned from it will depend on factors such as the wavelength of the excitation source as well as the power of the laser. The penetration depth of a given wavelength varies quite significantly between materials. The absorption coefficient,  $\alpha$  is a constant for a material at any wavelength and is calculated by,

$$\alpha = \frac{4\pi \times K}{\lambda} \quad (4.7)$$

Where  $K$  is refractive index and  $\lambda$  is the incident wavelength. It is a measure of the extent at which a material will absorb incident radiation. The absorption coefficient for germanium is much greater than that of silicon. Hence, the introduction of germanium into the silicon has a large effect on the overall penetration depth of the exciting laser, which in turn affects the intensity of the Raman spectrum, depicted in figure 4.12.

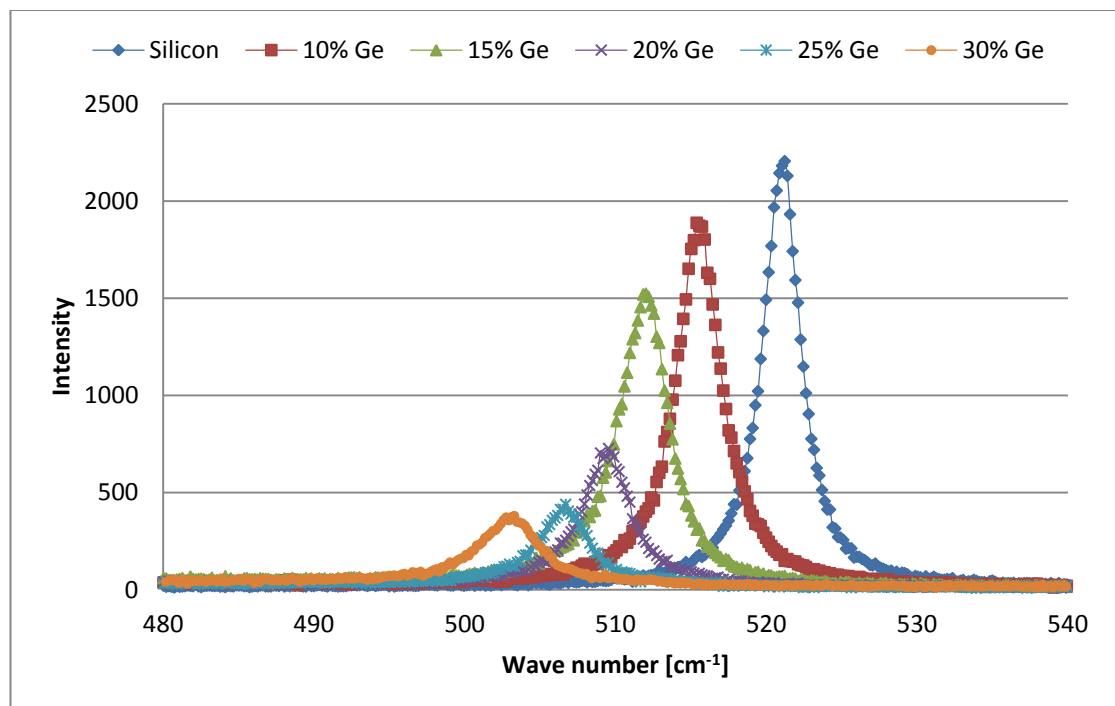


Figure 4.12. Effect of Ge composition on peak position and intensity.

Table 4.2 shows typical penetration depths at a range of wavelengths. Wavelengths in the UV region have the lowest penetration depth. When determining the strain in a silicon cap layer such as that on the samples used in this chapter, a wavelength in this region is the best choice of excitation source. The thickness of a strained Si cap layer is typically in the region of 10 – 20 nm. Penetration depth, therefore, becomes a problem

similar to that of the achievable spatial resolution. A schematic showing typical penetration depths of the commonly used excitation lines is shown in figure 4.13.

Laser Wavelength (nm)	Penetration Depth in Si (nm)	Penetration Depth in Ge (nm)
633	3000	32
514	762	19.2
488	569	19
457	313	18.7
325	~10	~9
244	~6	~7

Table 4.2. Effect of Germanium content on laser penetration depth [Horiba Jobin Yvon, 2008]

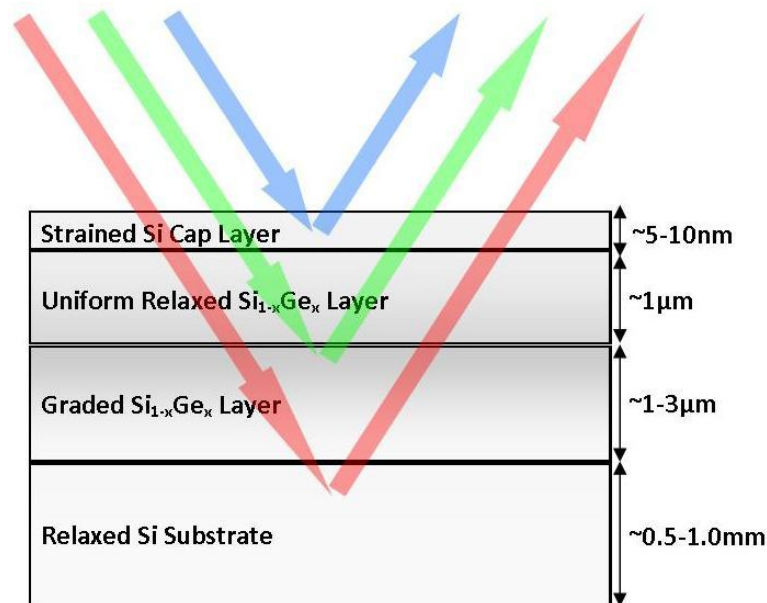
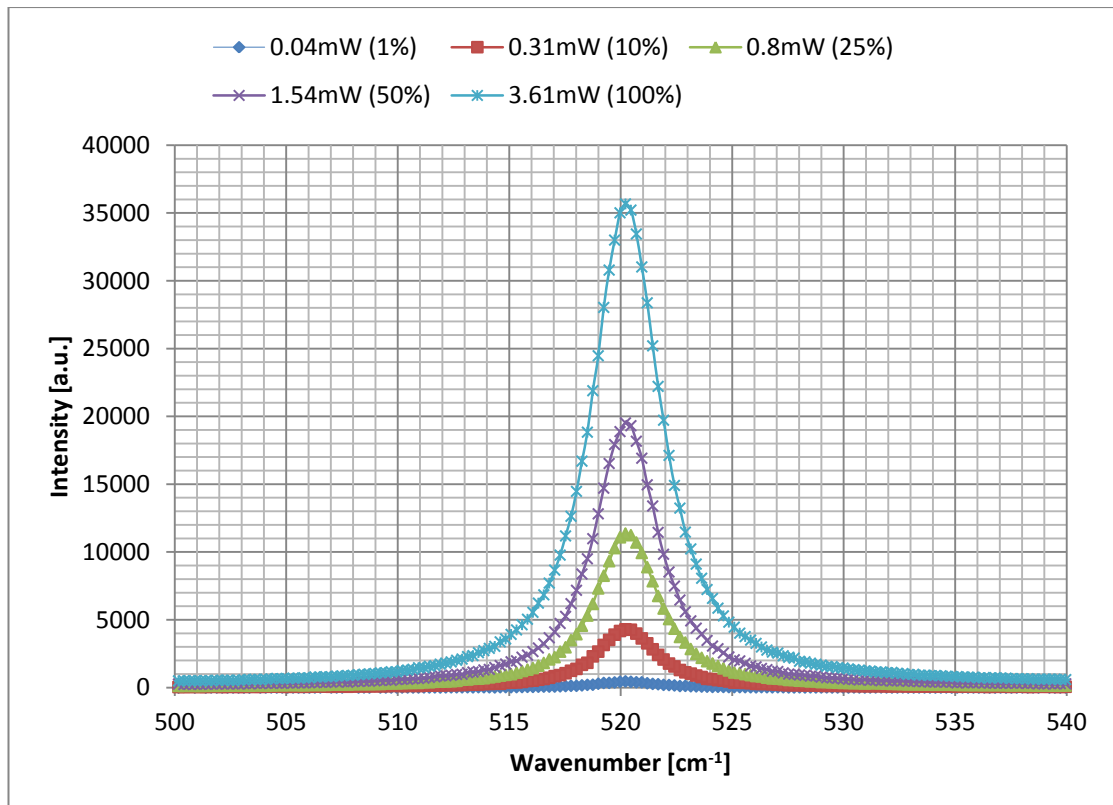


Figure 4.13. Schematic showing the typical penetration depths of some commonly used excitation lines. The blue arrows represent a UV source, with a wavelength of around 364 nm, and a penetration depth of only a few nanometres. A green laser, with wavelength of 514 nm will have a penetration depth of up to a micron, and a red laser of wavelength 633 nm will have the largest penetration depth in Si and Ge of much more than a micron, and up to 3 µm depending on Ge content.

The effect of the penetration depth is the level of detail it gives to a given region of the spectrum. The larger the penetration depth, the larger the overall probed volume. Shorter penetration depths will give a more accurate picture of what is happening at the

surface of the sample being analysed, however, other information may be lost. For example, a 364 nm excitation line will only give information from the first few nanometres of the silicon cap layer, therefore any information about the underlying layers cannot be gathered. Longer wavelengths make this layer difficult to analyse, but show in some detail the peaks from the other interactions described before i.e. the Si in SiGe, Si-Ge and Ge-Ge bonds. However, it is worth noting that when a larger volume is probed, the information gained is often an average of the strain throughout the layer and not necessarily specific to the region of interest.

Another factor affecting the overall output is the power of the excitation line, demonstrated in figure 4.14. Higher powers will cause an increase in Raman scattering, hence a spectrum with a higher intensity is acquired. Higher powers will also lead to less noise and a sharper peak. Using different powers throughout an investigation can lead to errors in results. It is therefore necessary to ensure all spectra are taken at exactly the same power. The power, as mentioned, should be chosen carefully. If too high a laser power is incident on a Si or SiGe sample then the local stress distribution may change due to the heating effect of the laser. This could lead to a slight shift in the peak position and therefore inaccurate strain analysis. The samples used here are relatively insensitive to the laser power, as the devices have been removed from the surface. It is worth noting that the peak position for each spectrum was within  $\sim 0.04 \text{ cm}^{-1}$ .



**Figure 4.14.** The intensity of a spectrum is directly affected by the power of the excitation source. Higher powers give a significantly higher intensity, however, can have a detrimental effect on the information gathered. Higher powers will drown out the peaks of much less intense bonds such as those from a strained silicon cap layer. More power also means more heat, and heat can affect the peak position giving a false value for strain.

The power of the laser used as an excitation source can have a significant effect on peak position. Large amounts of power incident on the sample surface causes the sample to increase in temperature. This heat can cause a sort of false strain, thus altering the peak position and giving erroneous results. Here, the penetration depth of the exciting laser needs to be taken into account again, along with the thermal conductivity of both silicon and germanium. The thermal conductivity of Ge is lower than that of Si [Glassbrenner, 1964, Cahill, 2005]. The larger the penetration depth, the larger the area the energy increase has to dissipate through. The series of figures below, 4.15 – 4.17 show the effect this has on the peak position of the strained silicon cap layer and the Si in SiGe bonds in the samples used earlier. The power from the 457 nm and 514 nm lasers was measured at each filter level using a handheld power meter, however, there was no meter available to measure the power from the UV laser, and hence arbitrary values of 1 – 100 % are used here with 100 % being the highest power available.

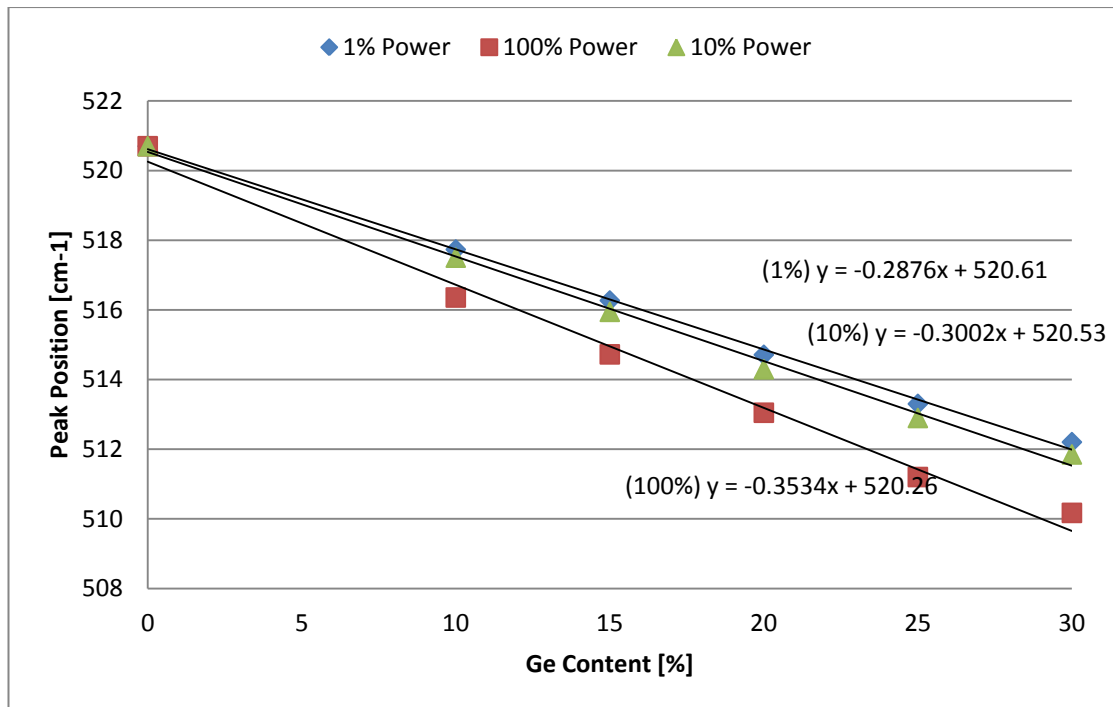


**Figure 4.15.** UV (364 nm) laser excitation source, varying powers shows a significant difference in peak position due to the heating affects at the sample surface. The small penetration depth coupled with the lower thermal conductivity of SiGe means that the heat is concentrated over a smaller area and not dissipated as well throughout the sample as the germanium content increases. The peak position shifts to a lower wavenumber as the heat is having the same effect as higher tensile strain in the sample.

Figure 4.19 shows the peak positions from the spectra obtained using a UV laser on samples with a silicon cap layer and varying Ge composition. The UV laser does not gather any information from any of the other bonds e.g. Si in SiGe etc. hence only data from the strained Silicon cap layer is shown. It is clear from this graph that there is a significant difference in peak position as the power increases and this difference is amplified as the Ge content also increases. In the pure silicon sample, the peak position remains the same within experimental error. Silicon has a better thermal conductivity than germanium, so although the penetration depth is still only in the order of nanometres, the heat is dissipated through a larger volume of sample than the other samples. As one small area of the sample is not being heated to any significant extent more than the rest of the sample due to heat dissipating quickly, there is no real difference in peak position unless the laser is incident in the same spot for a great length of time. However, as the germanium content begins to rise, the thermal conductivity of the sample worsens; therefore more heat is accumulating in a smaller region of the sample causing a shift in peak position that is more substantial, the higher the Ge content. If it is necessary to use a high power, this shift in peak position needs to be taken into consideration in any strain calculations. It is worth noting that these high

powers can have a permanent negative effect on the samples and it is possible to burn them.

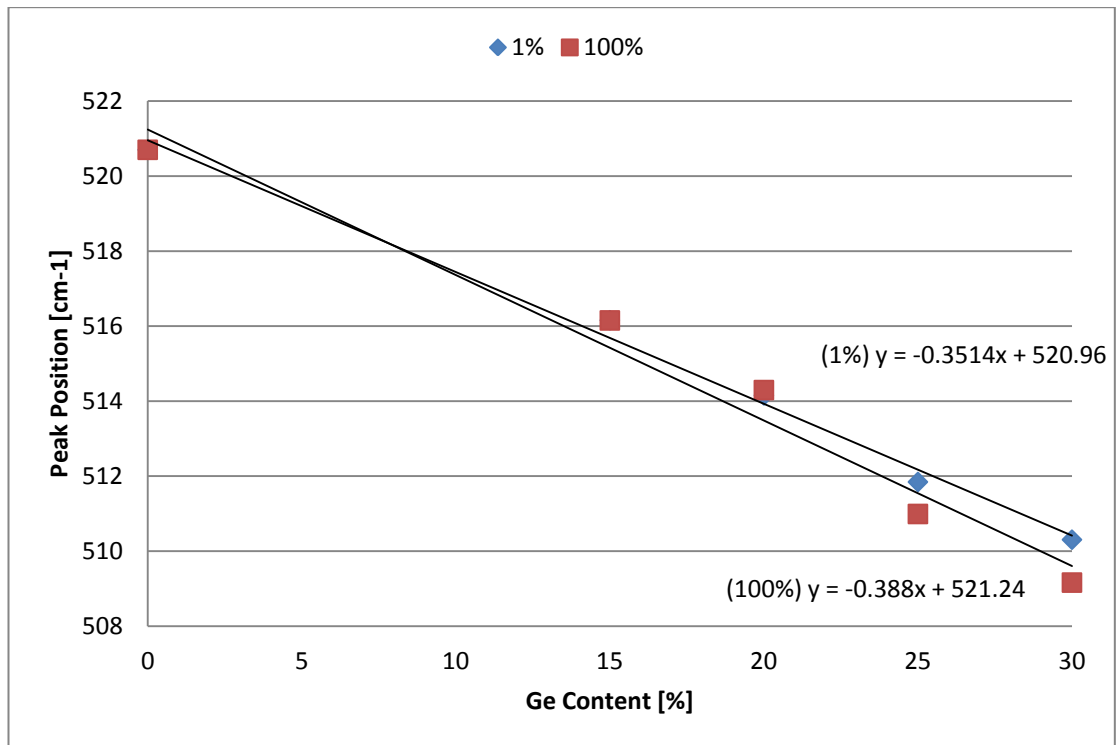


Figure 4.16. 457 nm exciting laser gives spectra with a difficult to analyse strained Si peak. The different in values only really manifests itself at higher Ge content and it could be argued there is no significant difference between the peak positions measured for either high or low powers.

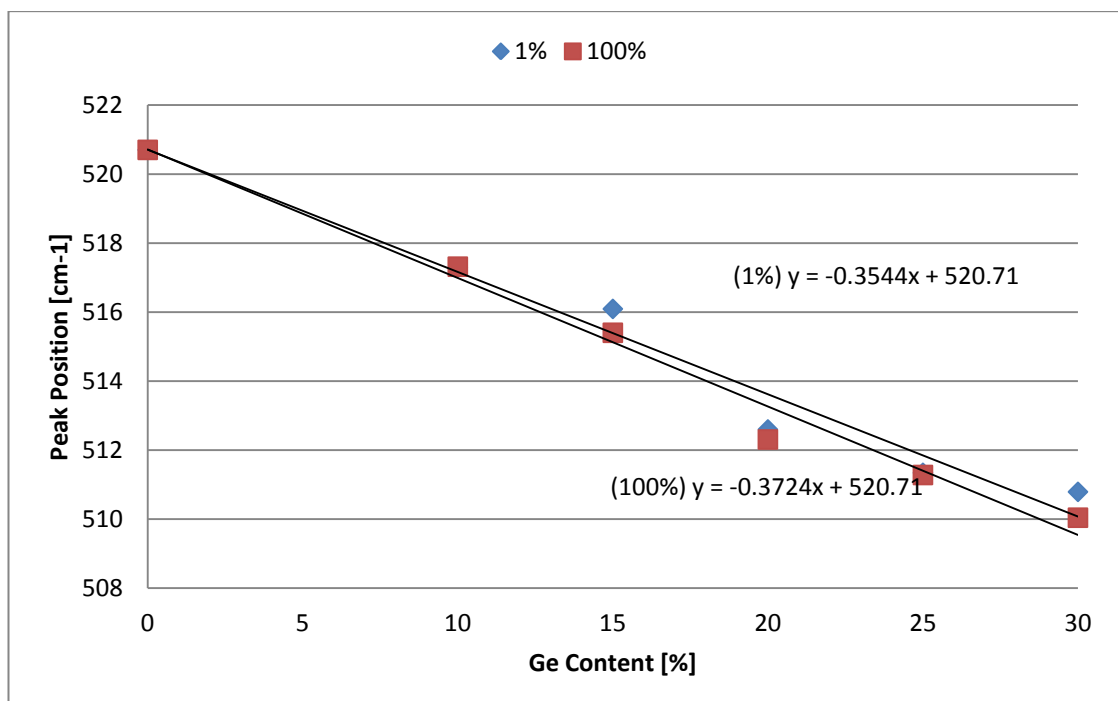
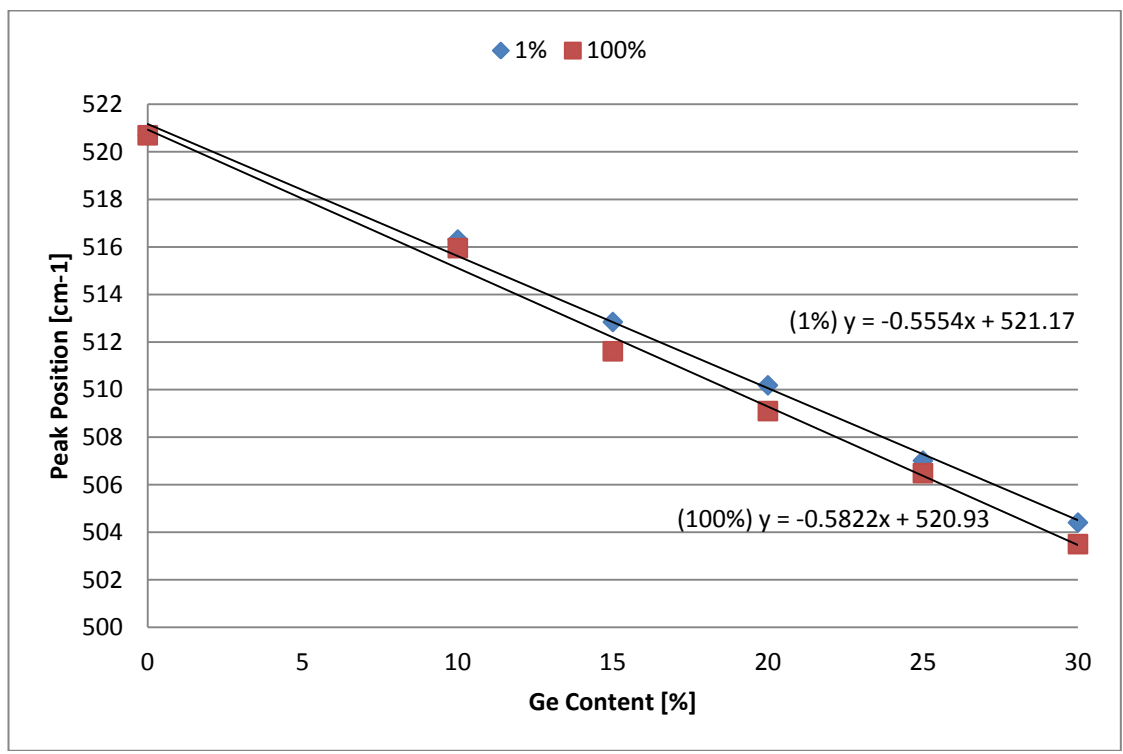
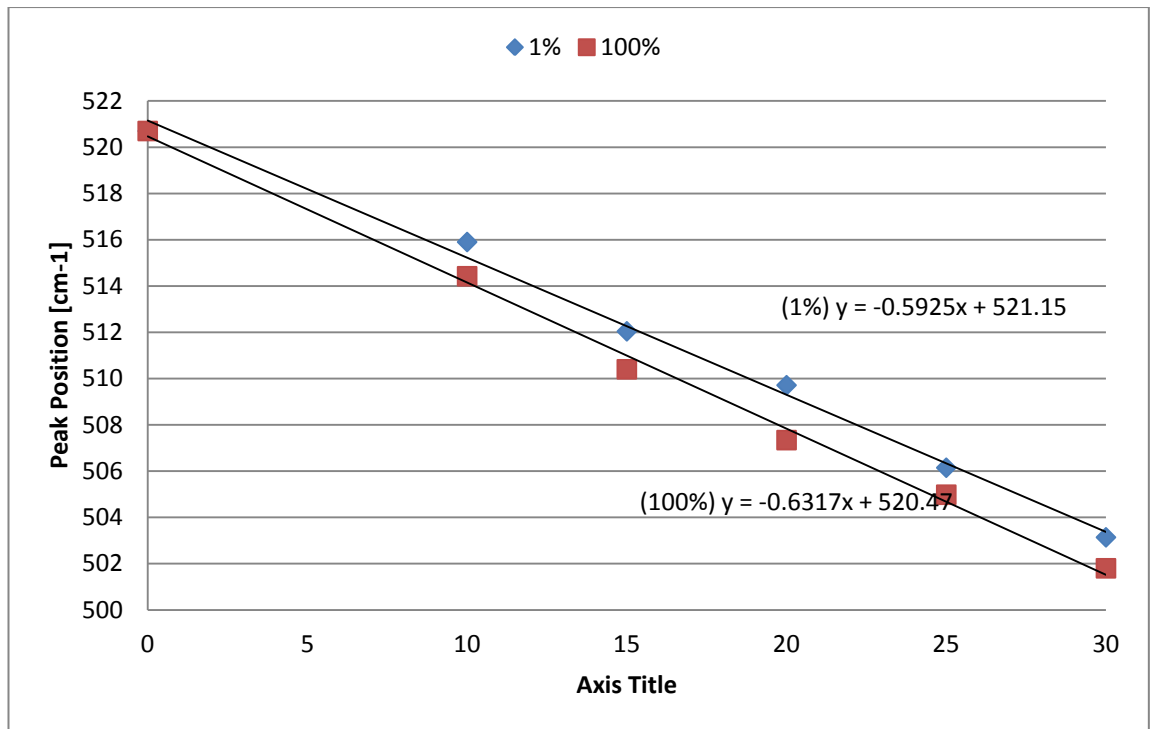


Figure 4.17. 514 nm exciting laser. The different in values only really manifests itself at higher Ge content and it could be argued there is no significant difference between the peak positions measured for either high or low powers.

Figures 4.20 to 4.23 were taken using 457 nm and 514 nm lasers as the excitation source to obtain spectra that show information from both the strained silicon cap layer and the Si in SiGe bonds. Although to a certain extent, the same differences are apparent as with the UV laser, the difference is not so considerable. The penetration depths of the 457 nm and 514 nm lines are much deeper than that of the 364 nm line. Any heating effect is distributed over a much larger volume, so even taking into account the differences in thermal conductivities of the materials, it can be argued that the overall effect the increase in temperature has on strain in the material is negligible.



**Figure 4.18.** 457 nm exciting laser gives spectra with a difficult to analyse strained Si peak. The different in values only really manifests itself at higher Ge content and it could be argued there is no significant difference between the peak positions measured for either high or low powers.



**Figure 4.19.** 514 nm exciting laser gives spectra with a difficult to analyse strained Si peak. The different in values only really manifests itself at higher Ge content and it could be argued there is no significant difference between the peak positions measured for either high or low powers.

#### 4.6. Verification of Raman results

In order to be certain that Raman results are as accurate as possible, they need to be confirmed by another method. Typically, this is done by XRD which is a highly accurate technique. Another potential way, briefly mentioned in chapter 2, is EBSD.

For elastic strain determination such as the strain present in the devices, the pattern the Kikuchi bands form may be used. Because the difference in Kikuchi pattern between strained and unstrained silicon is in the order of pixels and so cannot be seen with the naked eye, it is necessary to use image processing software.

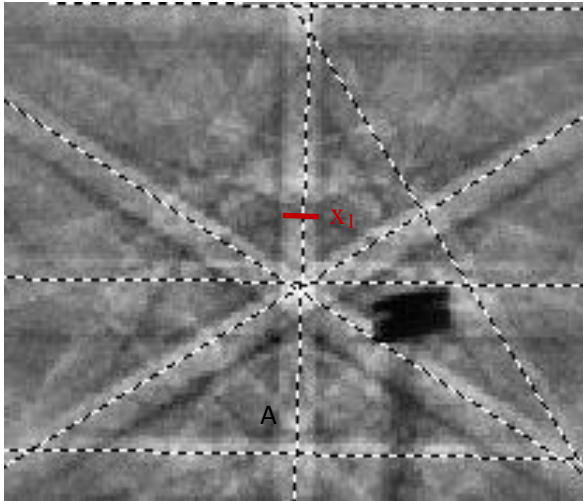


**Figure 4.20. Unstrained Si sample with Kikuchi bands of width  $x_1$ .**

The resolution of the phosphor screen is known, and this data can be used to measure the exact width of the bands.

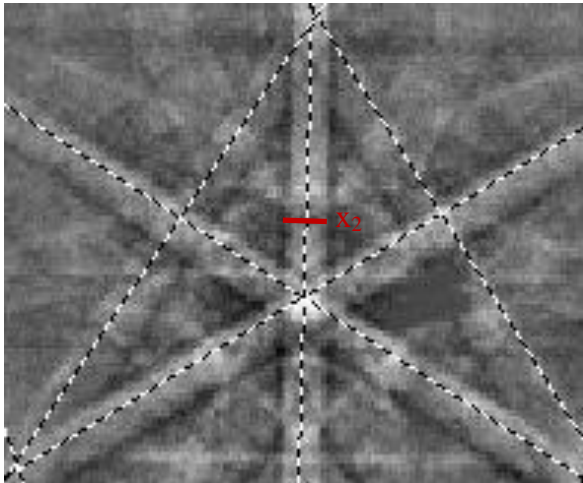


**Figure 4.21. Strained Si sample with Kikuchi bands of width  $x_2$ .**

Using imaging software to measure the relative widths of the bands allows a percentage value for strain to be calculated by;

$$\varepsilon_{\%} = \frac{x_1 - x_2}{x_1} \times 100 \quad (4.8)$$

Using this method on a Si<sub>0.7</sub>Ge<sub>0.3</sub>  $\varepsilon$ -Si sample gives a strain value using EBSD of 0.735%. The equivalent Raman spectroscopy result is 0.777%. This gives a difference of approximately 5% between the results. It could be argued that within experimental error, these results are similar, however, it is not accurate enough to be used as a Raman validation technique.

#### **4.6. Summary**

The differences shown between experimental, theoretical and literature results highlights the importance of calibration. Many factors can affect the experimental result making it differ from theoretical values and in order to collect good quality data, these factors must be taken into consideration throughout calculations.

The above results also show the limitations of conventional Raman Spectroscopy and highlight the importance of developing an alternative measurement solution. Results at the scale used in this investigation are prone to errors, however, there is potentially scope to push Raman Spectroscopy further.

Different measurement techniques bring with them different calibration methods. Many calibration methods are long standing, tried and tested techniques such as that for nanoindentation and EBSD. Calibration of equipment is still vital, it is important before any nanoscale measurement is carried out, sources of variation that could come from a machine that is not calibrated correctly are ruled out.

## Chapter 5. Strained Silicon on Insulator (sSOI) stripes

### 5.1. Introduction

When biaxial global strain is introduced to a semiconductor device, or bulk silicon surface, due to the techniques employed in growing the epitaxial layer, the strain is not evenly distributed. Structures such as strained silicon stripes have been shown to strain relax at the edges, but return their strain in the centre showing biaxial strain is also present in even in these narrow lines. Theoretically, however, if a narrow enough line or stripe of strained silicon is grown, there will be opportunity for complete relaxation in the width direction and something approaching uniaxial strain will have been achieved, which will eliminate the problems associated with biaxial strain.

Biaxial strained silicon can be difficult to implement in ULSI technology. Problems with material quality caused by misfit and thread dislocations, up-diffusion of Ge and cost are all key factors [Mistry, 2004]. Implications of design and fabrication of the meta-stable layers [Dodson, 1988] adds a complexity to the process that the disadvantages of may outweigh the benefits. Particularly when it is considered that at high effective fields, the hole mobility enhancement is modest. Uniaxial strain offers similar electron mobility gains, but much higher hole mobility improvements that are maintained at high effective fields [Shifren, 2004].

The strained silicon on insulator (sSOI) structures used in this investigation are equivalent to those grown on a SiGe buffer layer with 20% germanium content and are fabricated using Smart Cut technology [Ghyselen, 2004]. The technique is described in figure 5.1 below. Briefly, a thermally oxidised silicon wafer implanted with hydrogen is bonded to a secondary silicon (or strained Si) wafer. The initial wafer is then split where the hydrogen implant stops leaving silicon on oxide. This technique was employed for both samples used throughout this investigation, however, full details are beyond the scope of this thesis and the reader is referred to the work of Ghyselen *et al* mentioned above.

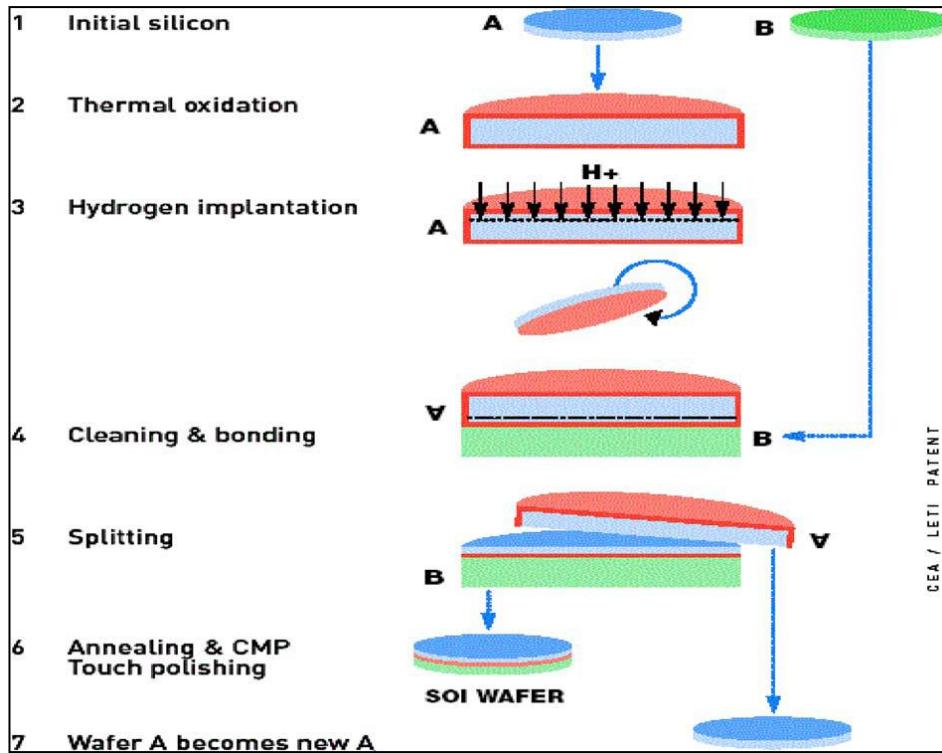


Figure 5.1. Schematic depicting the process flow for achieving a Silicon on Insulator (SOI) wafer. The process for strained SOI is similar and involves bonding a thermally oxidised wafer to a silicon wafer with a strained silicon epitaxial layer. Image from [Ghyselen, 2004].

The first half of the results will discuss strain relaxation with a decrease in stripe width, the second half investigates if pseudo uniaxial strain has been successfully produced in narrow stripes with a biaxial pad at each end of the stripe.

## 5.2. Results

### 5.2.1. 600 $\mu\text{m}$ sSOI stripes

The sample used in this investigation consisted of four 600 x 600  $\mu\text{m}$  boxes containing stripes of varying widths, shown schematically in figure 5.2, below. For each block, the pitch was 300 nm. The sSOI stripes were 25 nm thick on 140 nm buried oxide. The samples were supplied by FZ-Juelich. Figure 5.3 shows a SEM image of each stripe width.

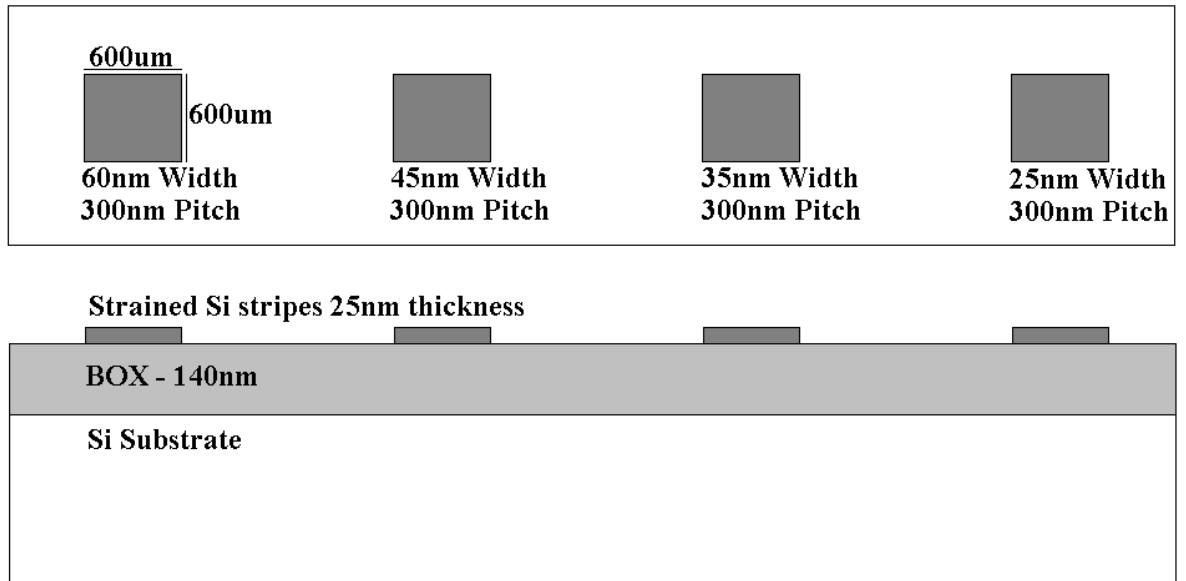


**Figure 5.2. Schematic of the initial sample, 600 x 600 μm sSOI stripes of varying widths. Each set of stripes had 300 nm pitch, were 25 nm of equivalent 20% Ge content on 140 nm of buried oxide.**

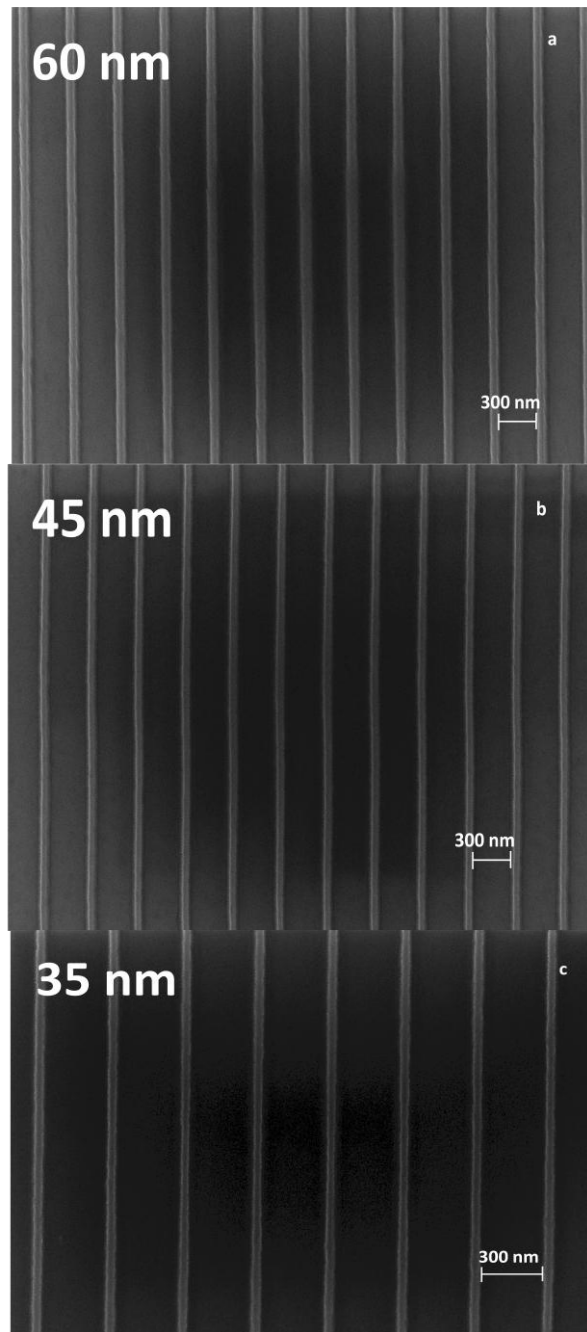


**Figure 5.3. SEM image of the sSOI stripes. A) 60 nm with 300 nm pitch. B) 45 nm with 300 nm pitch. C) 35 nm with 300 nm pitch. The 25 nm stripes are not shown due to significant damage across the centre of the box. These stripes were still analysed, though are thought to show significant relaxation due to the damage.**

Conventional Raman Spectroscopy was used initially to attempt to gain a profile of these very narrow stripes. ANSYS finite element (FE) simulations were used alongside to confirm the findings from Raman Spectroscopy. Due to a combination of the large laser spot size and the small pitch of the stripes, only an average measurement of strain could be calculated. The UV laser gives the smallest spot size at a little under 500 nm, with a pitch of 300 nm this results in at best one stripe being in the path of the laser, though more likely, for any given measurement, two stripes are being analysed. This

makes it impossible to gain any realistic view of the strain across the profile of a single stripe.

Care needs to be taken in choosing the experimental set up. There is a potential for erroneous results due to localised heating effects and damage from laser power in small, sensitive devices. However, reducing either the exposure time or power by too great an amount gives a signal that is very noisy and difficult to analyse with any accuracy.

The experimental setup chosen for the investigation was a 514 nm (green) excitation line held at 10% power, measured to be 0.7 mW. The spot size for the chosen laser can be calculated the laser spot size can be calculated using the formula:

$$d = \frac{1.22\lambda}{NA} \quad (5.1)$$

Where d is the diameter of the laser spot size,  $\lambda$  is the wavelength and NA is the numerical aperture of the objective.

The numerical aperture of the objective used was 0.9, so for a wavelength of 514 nm, the spot size is  $\sim 700$  nm. The exposure time per measurement was 2 seconds. The graph in figure 5.4 shows a  $2.4 \mu\text{m}$  line scan with 5nm step size. The line scan was carried out on the 60 nm stripes.

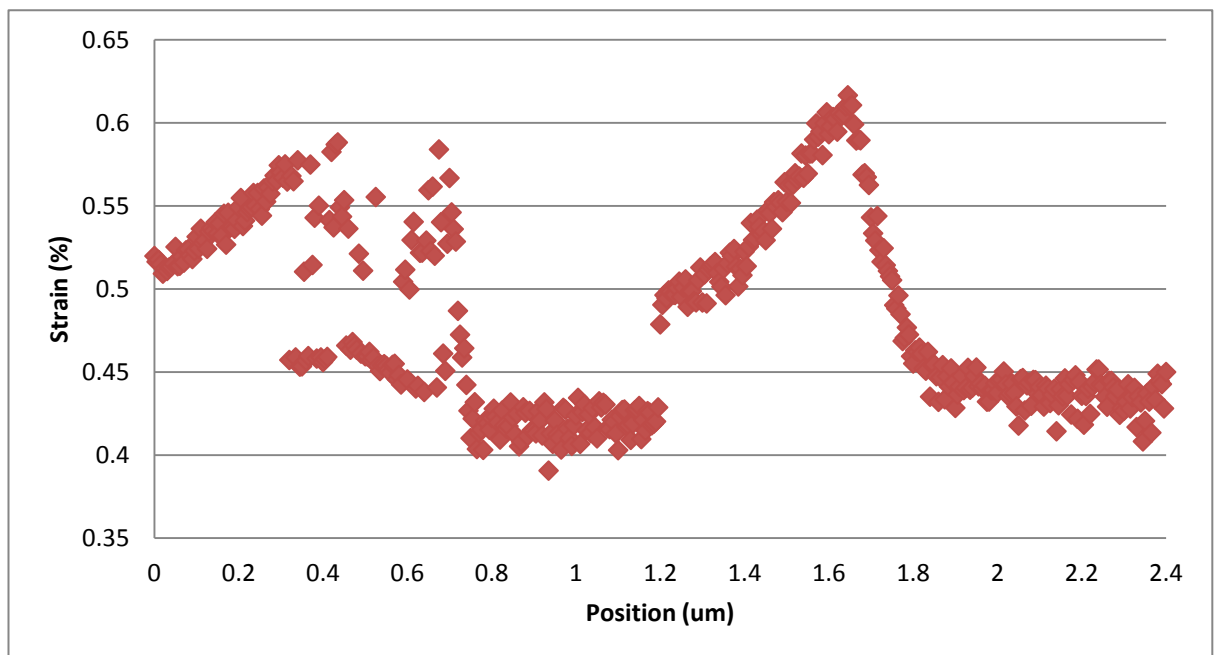


**Figure 5.4.** 514 nm laser source,  $2.4 \mu\text{m}$  line scan with 5 nm step size. Power was held at 0.7 mW and exposure time per measurement was 2 seconds.

The graph shows a repeating pattern with a sharp increase in strain, then a relaxation. The rise and fall occurs over approximately 600 – 800 nm, significantly larger than the width of the stripes even taking into account the pitch. While it is impossible, due to a combination of the sample pitch, stripe width and laser spot size, to establish a true stripe profile, what this shows is that there is an increase in strain somewhere on the profile of the stripe, however, what cannot be ascertained is exactly where this increase occurs. The value for strain never falls to zero because there will always be a portion of the stripe in the laser path, so there will always be a small signal from the sSi. The laser power profile is Gaussian so while there will be a signal from the whole of the laser spot, the centre of laser spot should be greatest as this is where the most power comes from, therefore a small changes in peak position from the stripes are still detectable. The above results show promise that a stripe profile can be achieved using conventional Raman Spectroscopy provided the pitch was larger. It was not possible to repeat this pattern on any of the narrower stripes.

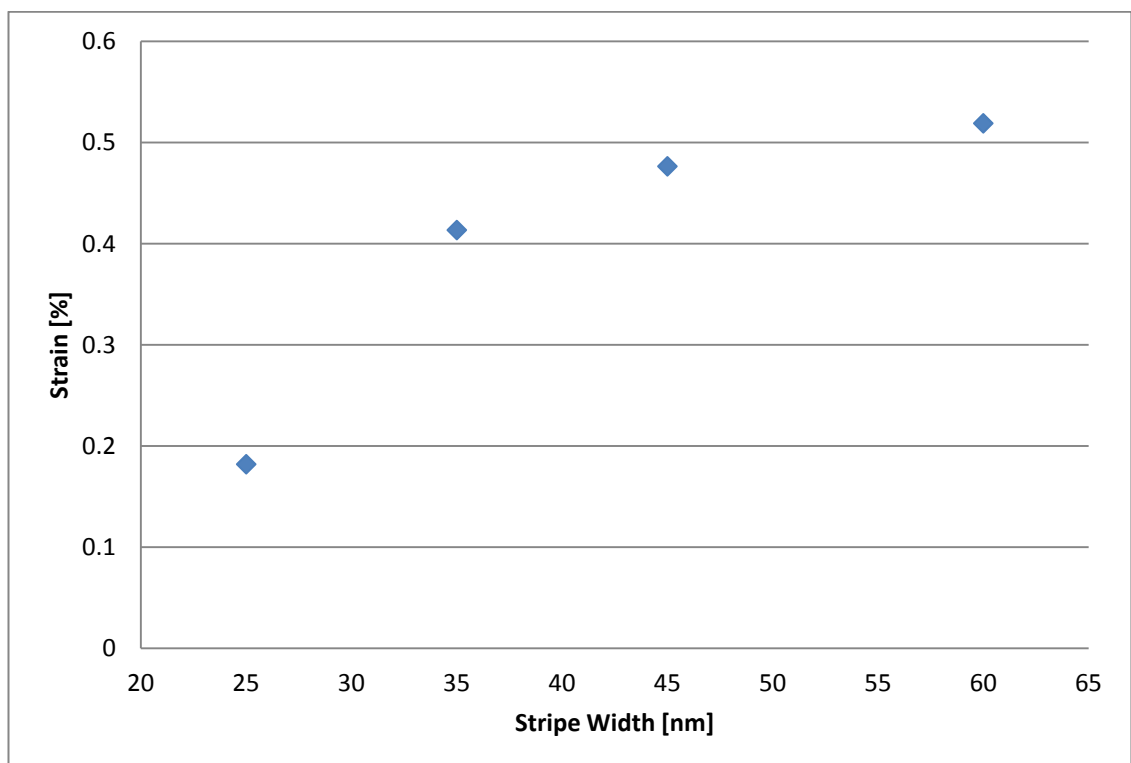


**Figure 5.5. Graph depicting strain relaxation as stripe width decreases. Damage on the 25 nm stripes has contributed somewhat to a lower than expected strain, however, the graph still indicates the relaxation isn't linear.**

Using the 457 nm (blue) laser, a 1  $\mu\text{m}$  line scan was carried out on each of the different widths. The laser power was held at 10% measured at 0.28 mW. Exposure time per measurement was 5 seconds. The graph in figure 5.5 shows that strain relaxes as the line

width decreases. It is important to mention that the sample had significant damage to the 25 nm stripes. Due to this damage, the peak position is likely to have shifted somewhat, giving a misleading strain value as the damage had caused some strain relaxation. However, the measurements were repeated several times and the results were consistent and indicate that the strain relaxation does not decrease linearly with a reduction in stripe width. As the width increases, the strain approaches the global, biaxial value. ANSYS simulations illustrated in figures 5.6 and 5.7 were carried out and show relaxation in the xx direction for all widths of stripe. The simulation shows absolute strain value, whereas the experimental results report a strain percentage.

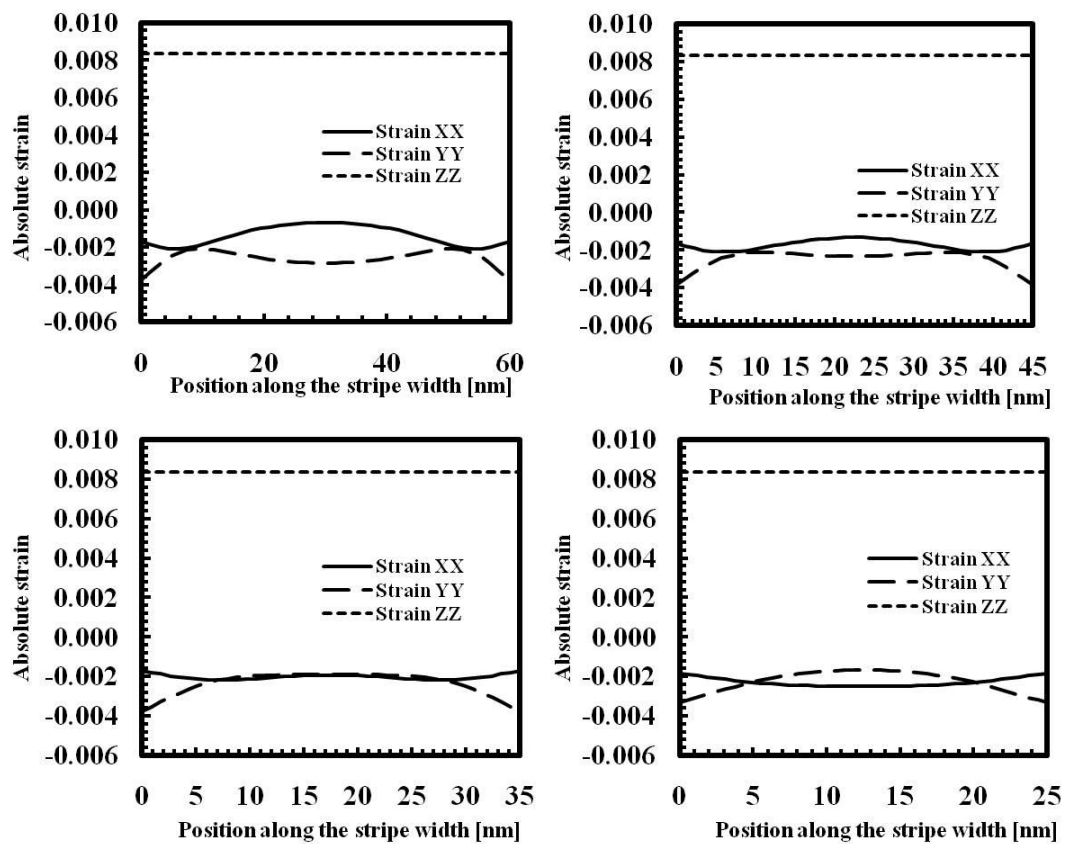
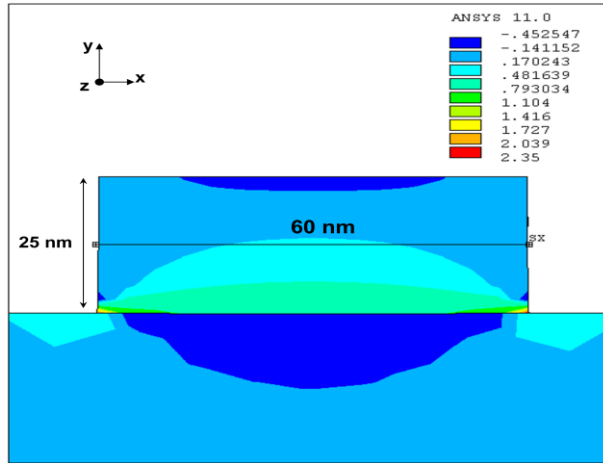


Figure 5.6. ANSYS simulations show almost full strain relaxation at the centre of the stripe for all widths.



**Figure 5.7. ANSYS simulation of 60 nm sSOI stripe**

The ANSYS simulation can predict exactly where within the system strain relaxation should occur. The above figures show that relaxation occurs, as expected, at the edge of the stripes for the slighter larger thicknesses. There is also significant relaxation within the stripe where it meets the silicon substrate. With narrower stripes, 35 nm and 25 nm, the strain is decreased, and the relaxation in the xx direction occurs more at the edge of the stripe. ANSYS simulation shows that the strain in the xx direction is compressive and that along the stripe the strain is tensile. Strain in the two directions is related by Poisson's ratio, where:

$$\nu = - \frac{\epsilon_{xx}}{\epsilon_{zz}} \quad (5.2)$$

Or;

$$\epsilon_{xx} = \frac{-\nu}{\epsilon_{yy}} \quad (5.3)$$

For silicon,  $\nu = 0.28$ , therefore, if  $\epsilon_{zz} = 0.008$ ,  $\epsilon_{xx}$  should be -0.0022 if complete strain relaxation has occurred. ANSYS values of around -0.002 are produced indicating that relaxation is not complete but conditions are close to uniaxial in the centre of the stripe. The Raman measurement will average strain in all directions so will measure a combination of tensile strain along the wire with compressive strain across the width. Average strain is calculated by;

$$\epsilon_{avg} = \frac{\epsilon_{xx} + \epsilon_{zz}}{2} \quad (5.4)$$

The average strain is 0.3 in this case – similar to what is observed for the 25 nm damaged stripes. ANSYS implies that almost complete relaxation has occurred along

the centre for all stripe widths but the experimental data in figure 5.5 shows that a higher strain is measured for the wider stripes implying incomplete relaxation. For the widest stripe the measured strain implies about 60% relaxation of the strain in the stripe.

### 5.2.2. 20 $\mu\text{m}$ sSOI Stripes

The sample used in the second half of the investigation were also provided by FZ-Juelich and consisted of blocks containing 20  $\mu\text{m}$  lines of varying widths, with a biaxially strained bond pad at each end as depicted schematically in figure 5.8. The stripes were 25 nm thick sSi equivalent of 20% Ge content, on 100 nm of buried oxide. A SEM image of the 70 nm stripes is shown in figure 5.9. The 70 nm stripes were analysed by Raman Spectroscopy lengthways and across the profile.

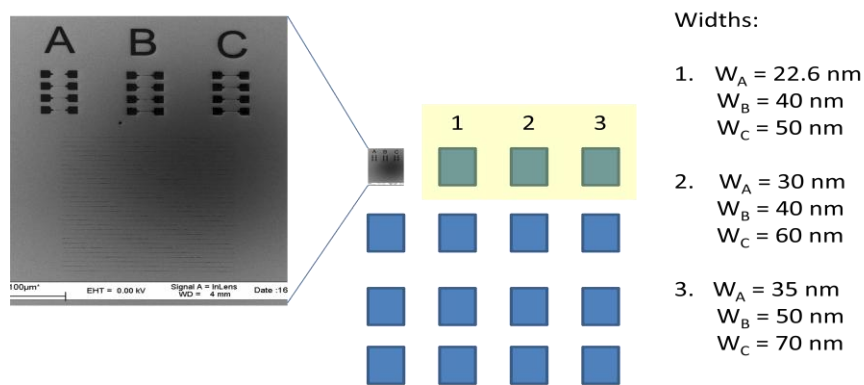


**Figure 5.8. Schematic of sSOI stripes with varying widths. A biaxially strained pad is present at each end of the stripes.**

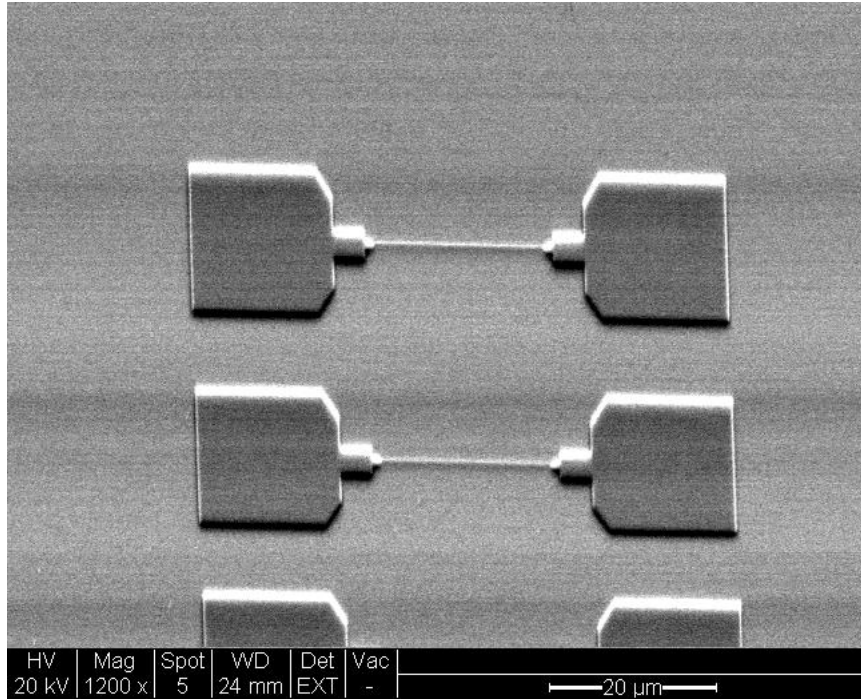


**Figure 5.9.** SEM image of 70 nm wide, 20  $\mu\text{m}$  long sSOI stripes with biaxial strained pad at each end

#### **5.2.2.1. Visible Laser**

From the investigation in the first half of this chapter, it is expected that in the 70 nm stripes there will be some degree of strain relaxation at the edges of the sSOI stripes. Initially, a 2  $\mu\text{m}$  scan was taken, with 5 nm step sizes. The majority of the scan was on plain silicon, the distance chosen to ensure there was a certain amount of clearance from the stripe at either side, taking into account the laser spot size. This distance also ensures, the whole of the laser spot covers every part of the width of the stripe.

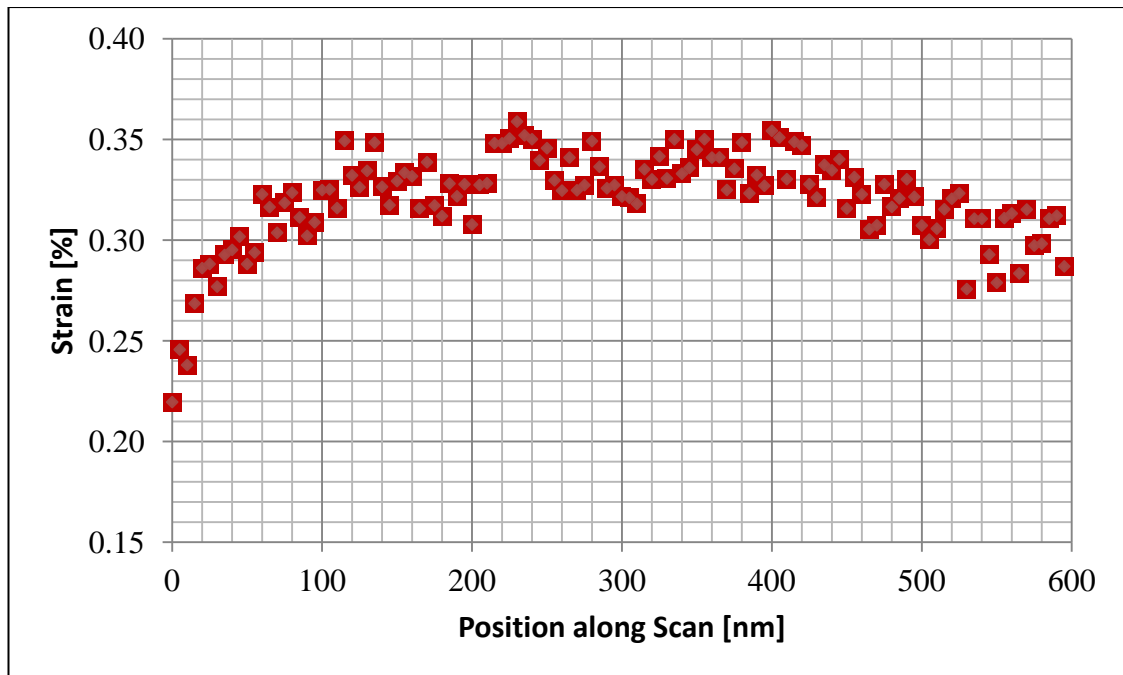


**Figure 5.10. 70 nm stripe profile taken using 514 nm laser at 0.7 mW power.**

Figure 5.10 shows a line scan taken using the 514 nm laser as the excitation source. The power was held at 10% which was measured to be 0.7 mW. The exposure time per measurement was 5 seconds. The chart depicts the stripe profile along the length of the scan. As mentioned previously in this chapter, the diameter of the spot size for the 514 nm laser is in the region of 700 nm. The distance of the line scan that shows a value for strain is approximately 600 nm, in keeping with the diameter of the laser spot.

The signal from this scan was very noisy, and there is a large amount of experimental error in the results. The oxide layer is invisible to the UV excitation line, and so the peak from the underlying silicon layer overwhelms the small strained Si peak. The signal from the narrow, thin stripe is extremely small and there is a high signal to noise ratio. When fitting such peaks, the strained Si peak often gets overlooked by the peak fitting software, making analysis very difficult. As such, a silicon spectrum taken well away from the stripes was subtracted from the scan spectra leaving a highly noisy but noticeable strained Si peak from the stripe which could be fitted more easily. The downside to this method is the increased error in fitting it leads to. However, this method is capable of producing a profile of the strip.

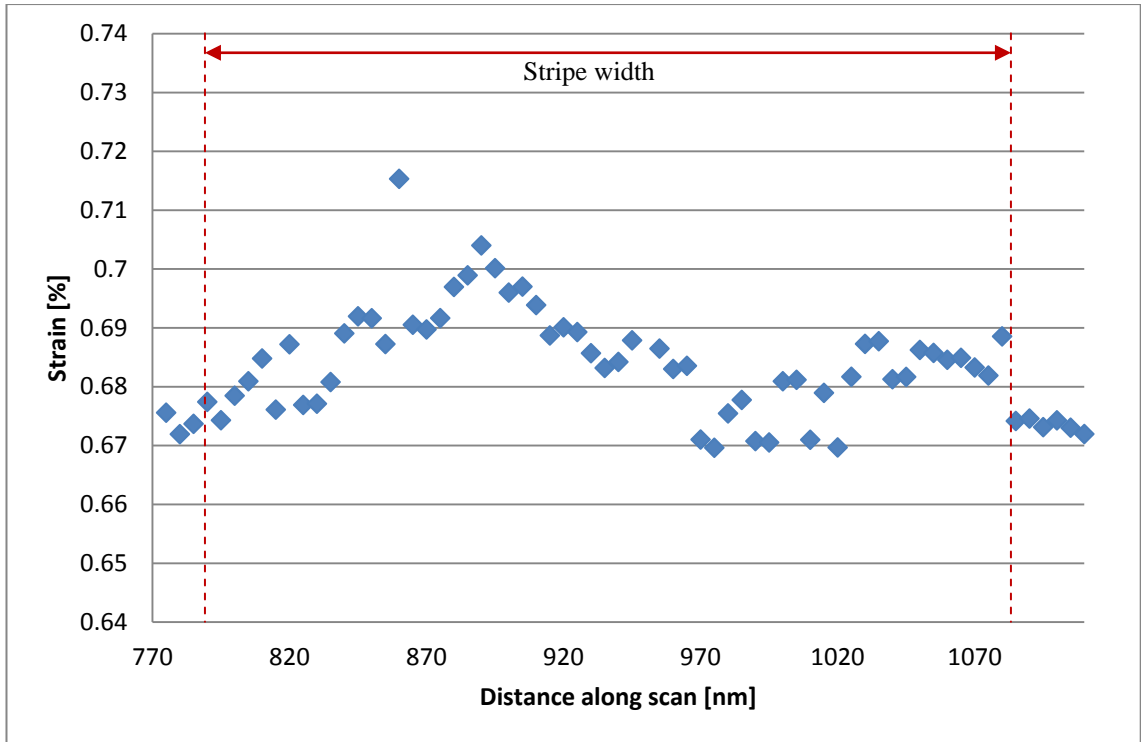
To get the profile in figure 5.10, several scans were taken with various configurations of power and exposure time until the optimum signal to noise ratio was found. The results were not repeatable every time. The calculated strain is significantly smaller than

theoretical strain for  $\text{Si}_{0.8}\text{Ge}_{0.2}$ . This difference can be accounted for, partly because of the reasons already discussed in the calibration chapter. On any given measurement, the signal will be collected from the whole of the laser spot. As previously mentioned, the laser power profile is Gaussian, and as such, the majority of the signal is collected from the centre of the spot. As such, an average strain of everything that is being probed by the laser for the measurement will be calculated, however, small fluctuations in peak position/strain are able to be picked up on due to the nature of the power profile. The overall strain value calculated is not, therefore, a perfectly accurate representation, but what is important in this investigation is showing where on the stripe the relaxation occurs and by what degree, as opposed to precise strain values. The profile agrees with the expected outcome and shows relaxation at the edge of the stripes. There is also a degree of relaxation in the centre of the scan which was also predicted by the ANSYS simulations.

To achieve the scan shown in figure 5.10 was difficult and time consuming, but shows promise that with careful measurements and analysis, conventional Raman Spectroscopy is capable of evaluating much smaller devices than it is currently used for.

#### **5.2.2.2. *UV Laser***

UV Raman was utilised to repeat the experiment described above, as this has the smallest beam footprint. The laser spot size can be calculated to be 495 nm. This is still vastly larger than even the widest stripe, 70 nm. Again, while using this method will only ever give an average of the peak positions showing across the whole of this spot, we can be reasonably confident that the change we see between the centre of the stripe and the edges is real as the results obtained agree with previous work and simulations. The limiting factor here is that the profile still shows the stripe to be around 500 nm rather than 70 nm.



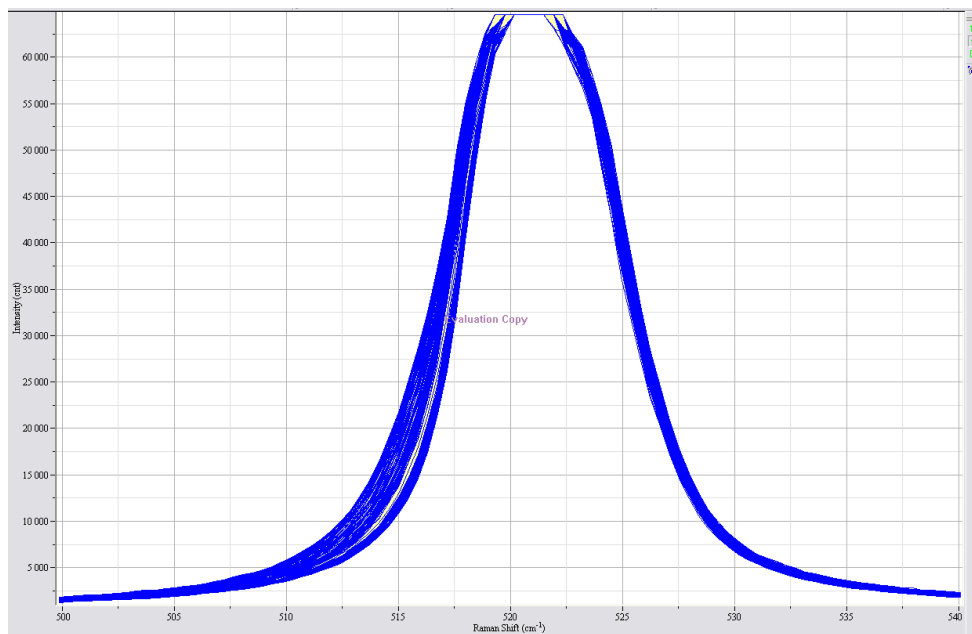
**Figure 5.11. Stripe profile of 70 nm wide stripe using UV laser held at half power and a 15 second exposure time per measurement along the scan. Scan step size was 5 nm.**

Figure 5.11 depicts the profile achieved from the initial experimental set up. The scan was 2  $\mu\text{m}$  using 364 nm laser line at 50% power. The exposure time per measurement was 15 seconds and the step size was 5 nm. No method of measuring the absolute power reaching the same was available and so only arbitrary values are given here in percentage form, as per the filters on the Raman microscope. A profile which shows good agreement with figure 5.10 was obtained, however, similar levels of noise are seen and there is little improvement with the smaller laser spot size.

By way of improving the signal to noise ratio between the strained and silicon peaks, it was necessary to increase the signal as much as possible from the stripe. To do this, the power reaching the sample and the exposure time had to be increased to such a point where the silicon intensity completely saturates the detector meaning the stripe peak is as large as it can be. Increasing the power, as previously discussed, has several drawbacks. The increased heat from the laser has the potential to burn and damage the sample. For these reasons, under normal conditions, it is necessary to keep the power as low as possible. A trade off was required where the detector was saturated, but the power was as low as it could be, and the exposure time as short as possible for this condition to still be satisfied. Several combinations were tested before settling on the final conditions. Silicon has much better thermal conductivity than silicon germanium

so this technique worked for these samples but would cause more problems with SiGe samples, thus more care would need to be taken.

Increasing the power to the highest possible and a 15 second exposure ensures that the detector is saturated and the highest possible intensity of strained silicon peak is achieved. Figure 5.12 shows a screen shot of the peak fitting software that gives evidence that it is the strained SI peaks that can be seen and is not just Silicon peaks broadening due to the increased intensity. This shows every peak in the line scan overlaid on top of each other. A strong Silicon peak is seen at  $520.7 \text{ cm}^{-1}$ . Down the high wavenumber, right hand side of the peak, there is variation of approximately  $0.3 - 0.5 \text{ cm}^{-1}$  which is within expected experimental error. However, down the low wavenumber, left hand side of the peak there is significant variation which appears to suddenly step up, as shown in figure 5.13.



**Figure 5.12. LabSpec screenshot of each spectrum overlaid. At the high wavenumber side of the spectrum there is little variation, however, there is a significant width variation at the low wavenumber side caused by the sSOI stripe.**

Because the high wavenumber side of the strained Silicon spectrum is identical, within experimental error, to the Silicon spectrum, this change in width on the low wavenumber side can only be attributed to the sSOI stripes.

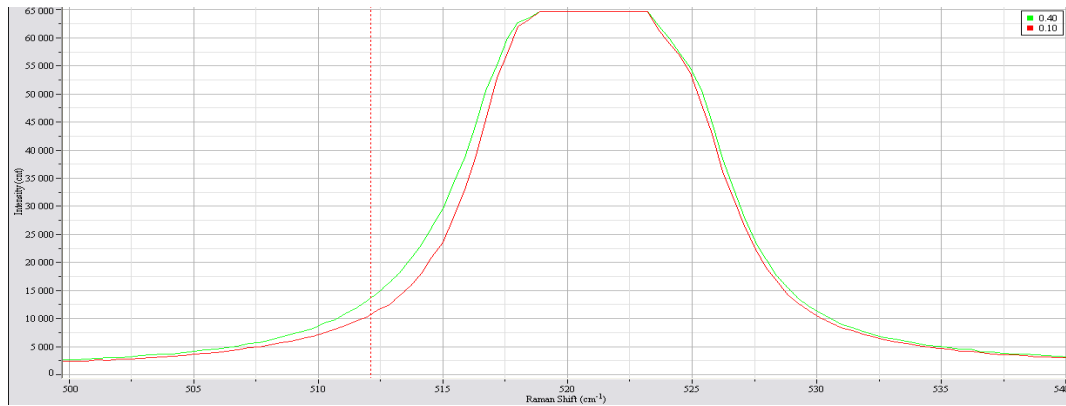


**Figure 5.13. LabSpec screenshot of the widest spectrum overlaid on an unstrained Si spectrum. The high wavenumber side of the spectra are identical. The difference in width on the low wavenumber side is down to the presence of a peak from the sSOI stripe.**

Repeating the earlier method of subtracting a silicon spectrum from the whole line scan leads to a difference spectrum as shown in figure 5.14. The signal to noise ratio has been improved to such a degree that the remaining spectra are comparatively noise free, and significantly easier to fit.

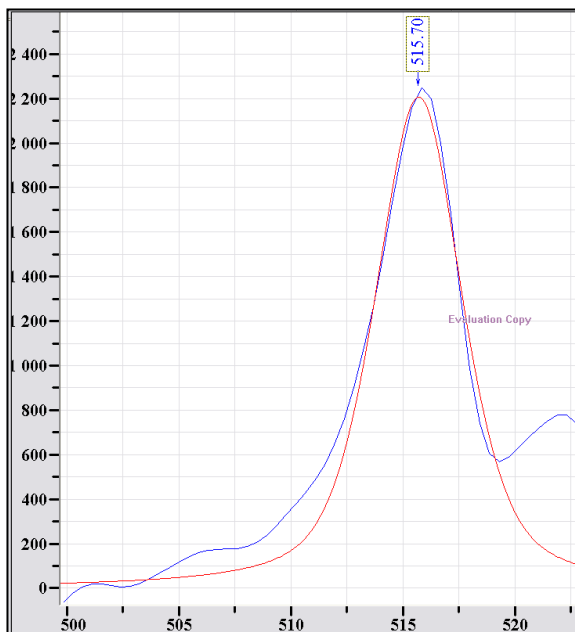


**Figure 5.14. LabSpec screenshot of the difference spectrum obtained from subtracting the Si spectrum from the wider sSOI spectrum.**

By employing this method, the profile shown in figure 5.15 is achieved. Although not easily repeatable, it is much simpler to replicate this profile than the previous. The pattern duplicates that seen in the very first profile, though the overall profile is now much smoother, with virtually no noise. The calculated strain values are somewhat closer to the theoretical values, implying less strain relaxation is measured for the UV laser.

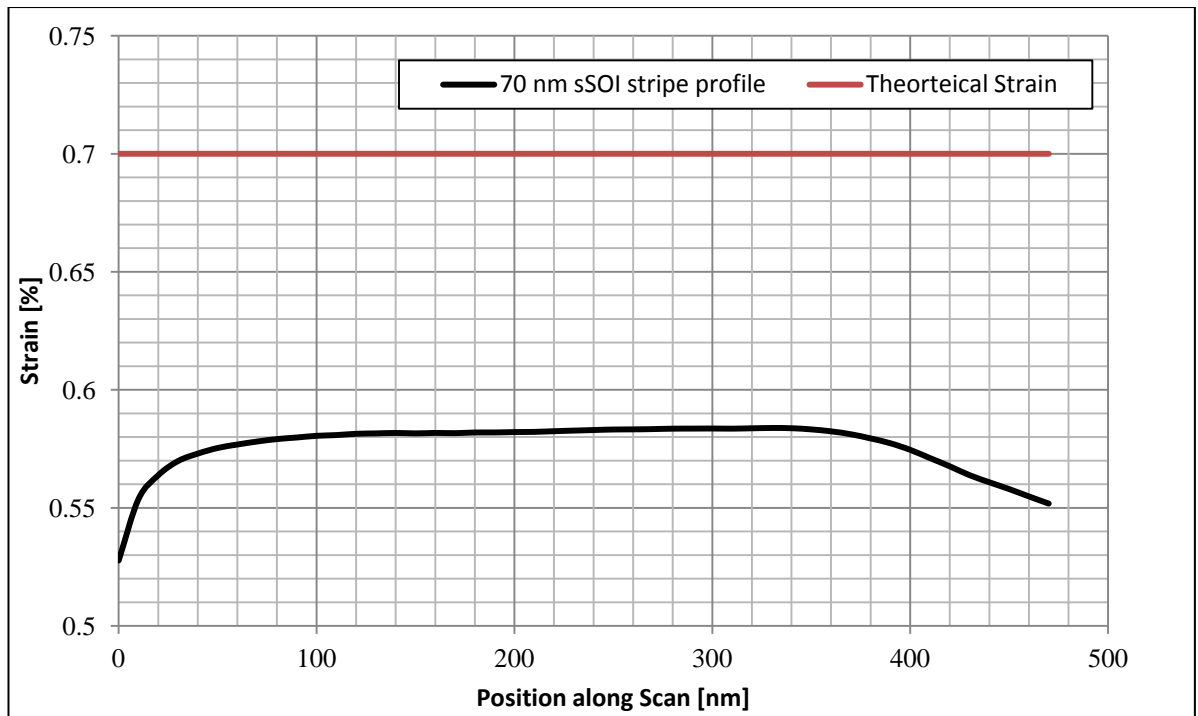


**Figure 5.15. Profile of the 70 nm sSOI stripe. The UV laser was held at maximum power with a long exposure time to ensure maximum intensity from the  $\epsilon$ -Si and hence the most accurate strain values are obtained. The theoretical strain line shows biaxial strain, the uniaxial value would be at 0.3%**

### 5.3. Summary

The methods employed throughout this chapter were lengthy and the importance of taking careful measurements with a well calibrated system and no external influences was paramount. Several problems were encountered due to everything from ambient room temperature, electrical interference and most prevalently, stage drift. When working in step sizes of sub 10 nm, even the slightest amount of drift has a significant effect on results. Minimising external influences also minimises stage drift.

This investigation shows that it is possible to use conventional Raman Spectroscopy to achieve results from much smaller features than previously thought, as long as certain conditions are met. Currently, it is simpler to achieve this than to use the much more complex and less understood tip enhanced Raman Spectroscopy (TERS). TERS, as well as a potential SERS method are discussed in the following chapter.

## Chapter 6. Surface and Tip Enhanced Raman Spectroscopy

### 6.1. Introduction

Surface Enhanced Raman scattering (SERS) was first observed in 1974 [Fleischmann, 1974] and was shown to be an effective method of amplifying the signal collected via the mechanisms described in chapter 2 [Pettinger, 1979, Moskovits, 1985]. Some 26 years later, work by M. S. Anderson in 2000 shows a Raman system coupled with an AFM termed RAFM or Raman Atomic Force Microscopy [Anderson, 2000], more commonly known as Tip Enhanced Raman Spectroscopy (TERS) demonstrating the potential to use an AFM tip to provide spatially selective enhancement of a Raman Signal using the SERS effect. The mechanisms behind what causes the enhancement for these techniques are still not fully understood and are the subject of some debate. Both of these techniques have been found to be more effective with some materials than others and SERS enhancement factors of  $10^8 - 10^{14}$  have been reported [Anderson, 2000]. Currently, SERS is more successful at demonstrating an enhancement with silicon based materials than TERS which has often non-repeatable and less significant enhancements. However, the major disadvantage of SERS, specifically when industrial applications are considered, is its destructive nature. The semiconductor industry strives to minimise costs and waste product, SERS is simply not a viable option for use in a production line to replace the currently used Raman Spectroscopy. The first half of this chapter will concentrate on a possible simple method of achieving non-destructive SERS and look in detail at the surface selective properties of the technique.

TERS, with its non-destructive nature is a much better option for industry, however, this technique is still at a stage where it will take a great deal of work for it to be of a standard that is of use in an industrial setting. When looking at simple dyes or carbon nanotubes, TERS provides a good enhancement and repeatable results [Stockle, 2000]. A system such as silicon and silicon germanium proves difficult to gain a repeatable enhancement, if an enhancement is seen at all. Literature suggests enhancements are achievable on silicon samples using a TERS setup using silver nanoparticles and 488 nm exciting line [Hayazawa, 2007], however, it was not possible to recreate these experiments. The second half of this chapter demonstrates the importance of the set-up and the sample orientation in order to take specific, accurate measurements.

## 6.2. Nanoparticle fabrication

The review of the literature in chapter 2 explains SERS and TERS operation and the need for a metal nanoparticle (NP) to be present in order for an enhancement to be gained. Here, for SERS experiments, a gold NP solution was fabricated by a reduction method detailed below. Presence of gold NPs was confirmed by UV-Vis spectroscopy, EDX and SEM images, figures 6.1 and 6.2.

The NPs were suspended in hexane, a non-polar solvent. Being non-polar ensures the solvent cannot bond or react with the particles. When a droplet of the NP containing solvent is allowed to dry on a sample surface, the addition of more hexane will ‘wash’ the NPs from the surface. This potentially provides the basis for a simple non-destructive SERS solution.

Nanoparticle fabrication was carried out as follows:

Gold (III) Chloride ( $\text{AuCl}_3$ ) (0.1217 g, 0.4 mmol) was dissolved in approximately 13ml of deionized water. Phase transfer catalyst tetraoctylammonium bromide (TOAB) (0.9649 g, 1.76 mmol) in chloroform ( $\text{CHCl}_3$ ) (9 ml) was added to the gold (III) salt solution and stirred vigorously for an hour at room temperature. The mixture was then added to a separation funnel where the layers were separated and the aqueous layer discarded. Dodecanethiol ( $\text{C}_{12}\text{H}_{25}\text{SH}$ ) (86  $\mu\text{l}$ , 35 mmol) was added to organic phase and stirred for 5 minutes. The reducing agent, sodium borohydride ( $\text{NaBH}_4$ ) (0.1786 g, 4.72 mmol) was dissolved in 11 ml of deionized water and added drop wise over 3 minutes. The resulting bi-phasic solution was left stirring overnight.

The solution was placed in a separation funnel and the layers separated with the aqueous layer discarded. The remaining organic phase was placed in a conical flask and was diluted with a polar solvent (ca. 30 ml Methanol ( $\text{MeOH}$ )) until precipitation began. The organic solution was divided equally in into 4 PTFE vials and centrifuged at 3500 rpm for 45 minutes at  $10^\circ\text{C}$ . On completion, black particulate matter had fallen out of solution, while the supernatant formed was colourless. The colourless supernatant was removed and the residual solid re-suspended in hexane and stored in vials prior to further analysis.

The process for silver dodecanethiol nanoparticle synthesis would be exactly the same, replacing the gold salt with Silver Nitrate ( $\text{AgNO}_3$ ) (0.068 g, 0.4 mmol).

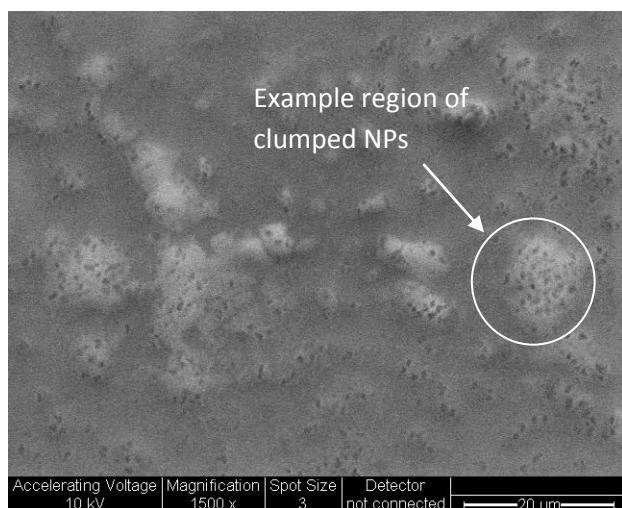


**Figure 6.1.** SEM analysis of gold nanoparticles. The particles are contained within the raised areas, however, the SEM image could not be resolved enough to focus on individual particles or clumps of particles. TEM would be required for this analysis

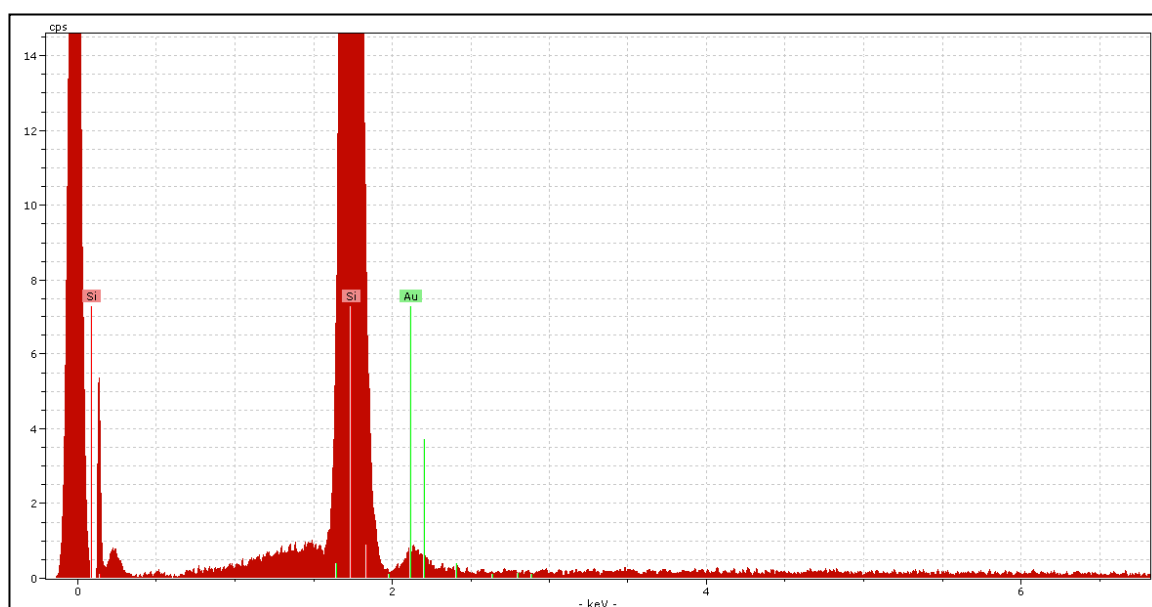


**Figure 6.2.** EDAX spectrum confirms the presence of small quantities of Au

### 6.3. Non-destructive SERS

The NPs suspended in hexane were deposited onto the sample by surface vertical deposition [Diao, 2003]. At this stage, this is a fairly crude method of depositing the NPs, with no control whatsoever on where they were deposited or in what formation, this would need to be refined in order to ensure particles are deposited in the area to be analysed. However, due to the nature of suspending the NPs in a non-polar solvent such as hexane, the particles were not adhered to the surface by anything other than a weak and reversible bond. If it was necessary to have a non-destructive method of analysis,

such as in the semiconductor industry where cost issues are such a burden. These results have been positive in that they have confirmed the possibility of non-destructive SERS.

Following the investigation, the samples were rinsed in hexane and analysed by EDAX. This demonstrated the ability to remove the Au NPs.

#### 6.4. SERS experiment

The samples used were plain silicon, and  $\text{Si}_{0.8}\text{Ge}_{0.2}$  with varying strained cap layer and virtual substrate thicknesses as detailed below in figure 6.3.

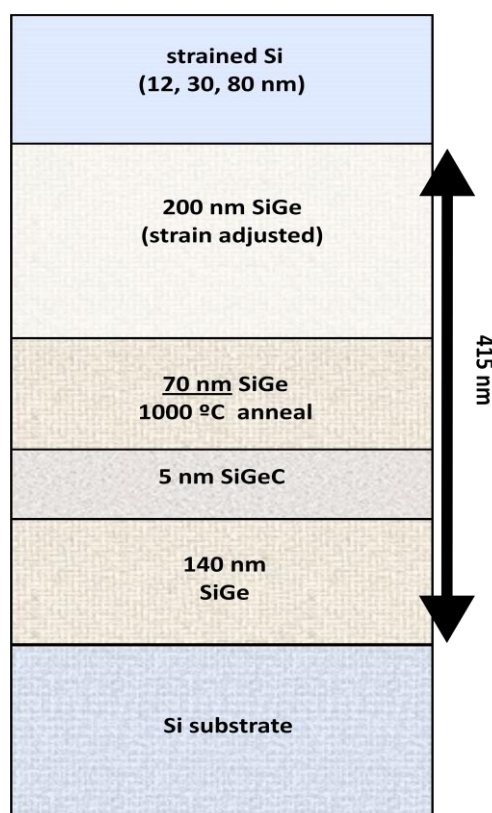
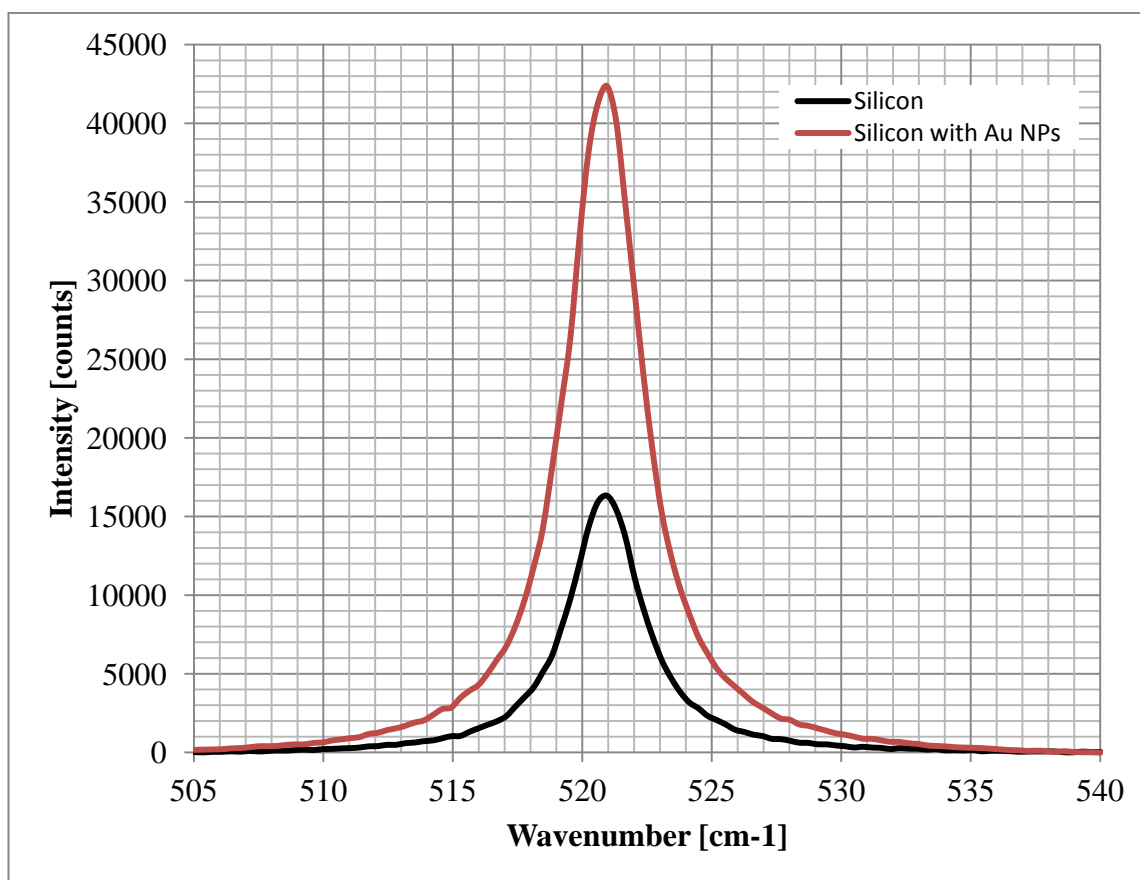


Figure 6.3. Thin C-growth SRB: D02: 12 nm strained Si; D04: 30 nm strained Si; D05: 80 nm strained Si proved by Sematech.

Au NPs were deposited by surface vertical deposition. For further details please refer to work by Diao [Diao, 2003]. The samples were held vertically in the solution and slowly drawn out. Where the meniscus of the liquid formed, the NPs were bonded with the surface. Under a microscope, drying marks from the solvent could be seen, and the NPs formed a random pattern.

The Raman Microscope was set up to use the visible laser tuned to 514 nm (green) excitation line. The filter was set to 25% power. For each sample, several points on the sample were measured, both on and away from areas of NP congregation.

### 6.4.1. Silicon



**Figure 6.4. Plain silicon spectra taken from a sample coated in Au nanoparticles compared with a sample without. The consistent, reproducible enhancement with the presence of Au NPs shows an increase in amplitude of ~260%. The formation and location of the NPs seemed to make little difference to whether an enhancement was achieved.**

There is a significant, clear enhancement of silicon with gold NPs present, depicted in figure 6.4 above. The intensity of the silicon peak with the Au NPs is 260% bigger than bare silicon, significantly smaller than the enhancements reported in literature, but still large. The peak width and positions, within experimental error, are exactly the same.

This was repeated several times, on several sections of the sample, with similar intensity readings achieved each time. The relative positions and pattern of the NPs compared with the laser spot made no difference to the overall intensity, indicating that for pure silicon, the sensitivity to NP size and location is low, as long as there are Au NPs in the laser spot, there will be an enhancement. For plain silicon, machine setup is relatively unimportant and it is easy to achieve an enhancement.

#### 6.4.2. D02: 12 nm sSi

This sample has a very thin cap layer characteristic of what is likely to be found in an actual device. This was grown on a 4-layer, 415 nm fully relaxed SiGe buffer at 20% Ge as per the schematic in figure 6.3.

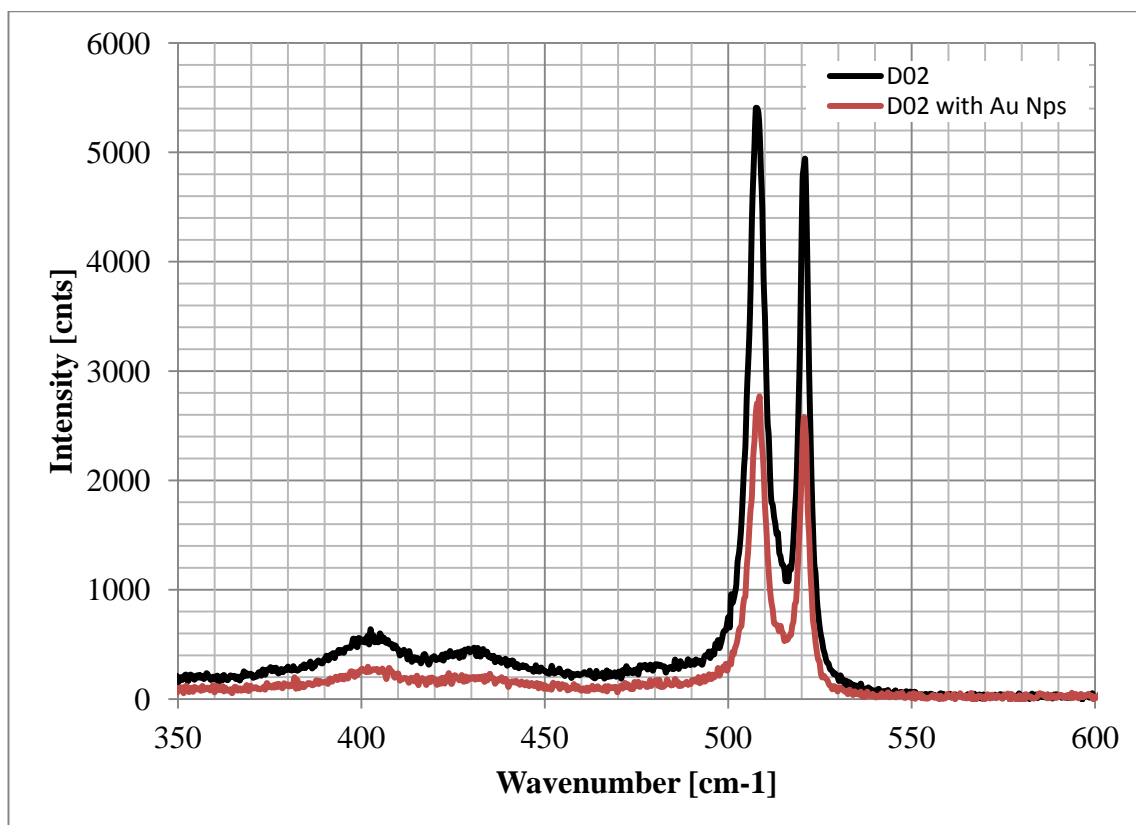


**Figure 6.5.** Sample D02 was a 4-layer  $\text{Si}_{0.8}\text{Ge}_{0.2}$  virtual substrate with a fully strained 12 nm  $\epsilon$ -Si cap layer. Samples were provided by Sematech. While there is no overall enhancement to the signal amplitude in this case, it can be argued that the small  $\epsilon$ -Si peak manifests itself as a more obvious peak rather than a shoulder. However, this spectrum was not reproducible on every measurement.

The most apparent feature of the SiGe sample D02 is the fact that the spectra taken on the samples with NPs have a lower intensity than those without, so in this respect, no enhancement is seen at all, figure 6.5. Potentially, the Au NPs are making the resulting signal more surface selective, one of the features of both SERS and TERS. Although in this instance, the signal from the cap layer is very small, it is actually much more of an obvious peak than that achieved from the sample without the NPs present.

Relative intensity of the strained Si peak to the Si peak is fairly similar across both the sample with the NPs compared to without. However, where without the NPs there is a broad shoulder that almost looks like noise in the spectrum, with NPs, there is much clearer ‘peak.’ Within experimental error, the peak positions are in the same place. The

strained Si peak when NPs are present measures at  $514.6\text{ cm}^{-1}$ , without NPs it is  $513.6\text{ cm}^{-1}$ . The Si in SiGe peak with NPs present was  $508.2\text{ cm}^{-1}$  and without;  $507.9\text{ cm}^{-1}$ .

The ratio of intensities for the strained Si to SiGe peaks confirms that there is no relative enhancement of the strained Si peak. In fact, the ratio is fairly similar; without Au NPs present, the strained Si peak is approximately 26% the height of the SiGe peak and with NPs it is 25%. Within experimental error, these are arguably the same. The slightly clearer strained Si peak was repeatable, but it is important to stress that while it was possible to reproduce these results, it was not consistently achievable, there is, therefore, no evidence for surface enhancement or selectivity beyond the less intense signal for this sample.

#### 6.4.3. D04: 30 nm sSi

This sample has a slightly thicker cap layer at 30 nm. This was grown on a 4-layer, 415 nm fully relaxed SiGe buffer at 20% Ge as per the schematic in figure 6.3.

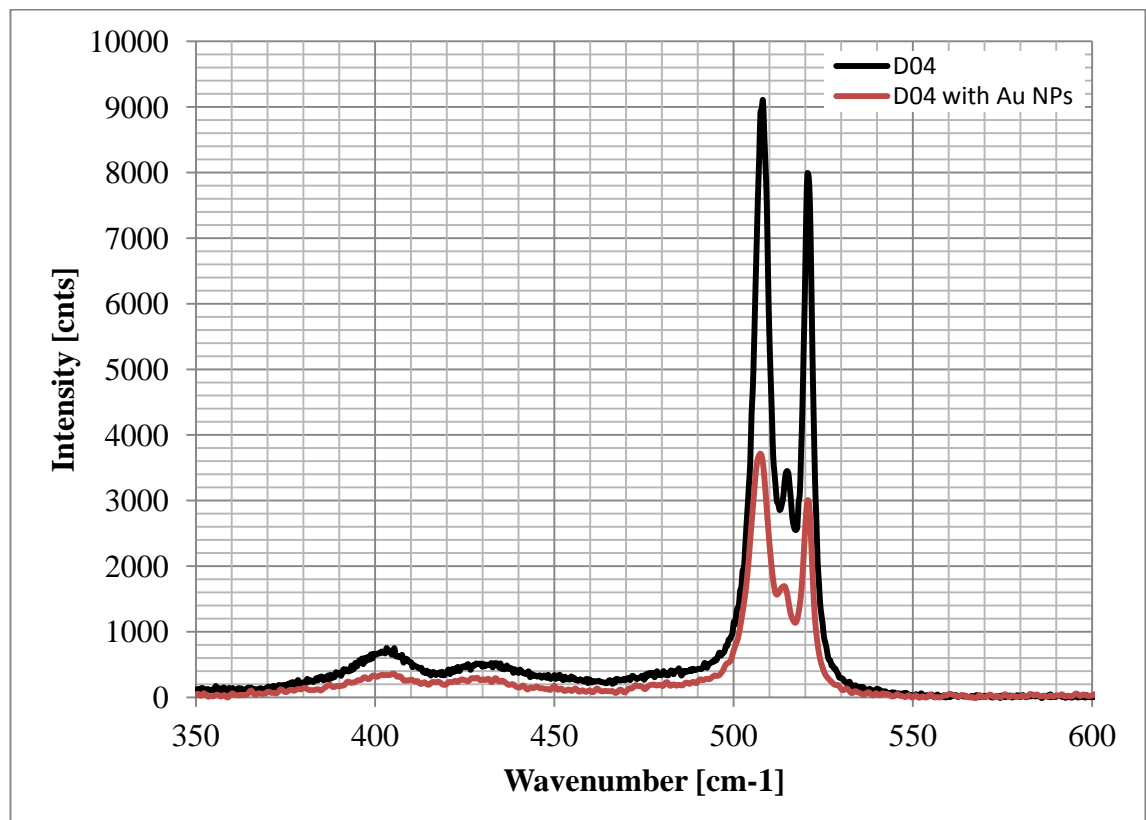


Figure 6.6. Sample D03 was a 4-layer  $\text{Si}_{0.8}\text{Ge}_{0.2}$  virtual substrate with a 30 nm  $\epsilon$ -Si cap layer. Samples were provided by Sematech. Once again, there is no overall enhancement to the signal amplitude. The relative intensities of the  $\epsilon$ -Si peak to the Si in SiGe and Si peaks shows that there was a small ( $\sim 5\%$ ) enhancement of this peak, indicating that with a slightly thicker cap layer, surface selectivity is beginning to become apparent.

Figure 6.6 shows once again, there is no enhancement to the intensity of the signal, however, the strained peak is about 60% of the intensity of the silicon peak with NPs compared with about 42% without. For strained Si to SiGe peaks, without NPs, the strained Si height is about 37% of the SiGe height, and with NPs it is about 43%, so there is approximately a 5% improvement in signal from the 30 nm cap layer. The relative intensity here indicates that with the presence of NPs, the signal collected is somewhat more surface selective. Within experimental error, the peak positions are the same in either case. The strained Si peak when NPs are present is at  $514.4\text{ cm}^{-1}$ , whereas without it is  $515.1\text{ cm}^{-1}$ . The Si in SiGe peak with NPs present was  $507.3\text{ cm}^{-1}$  and without;  $507.9\text{ cm}^{-1}$ .

#### 6.4.4. D05: 80 nm sSi

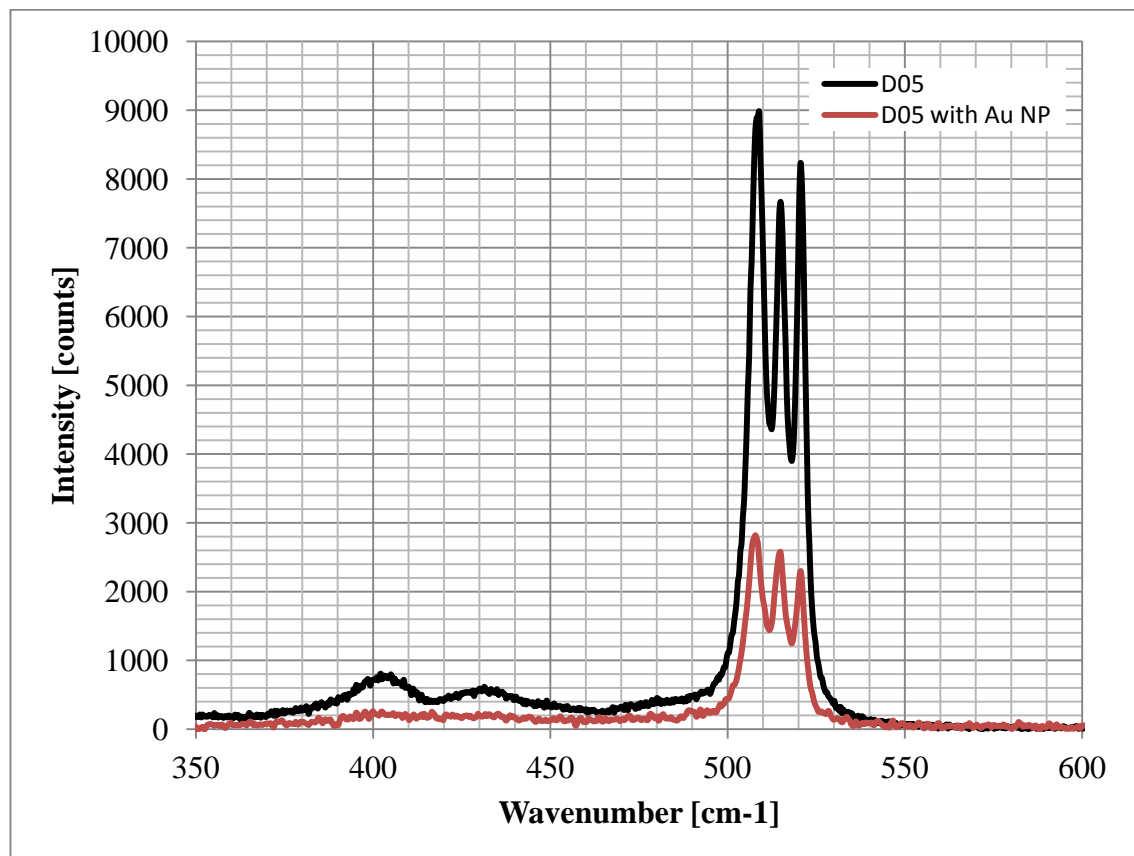
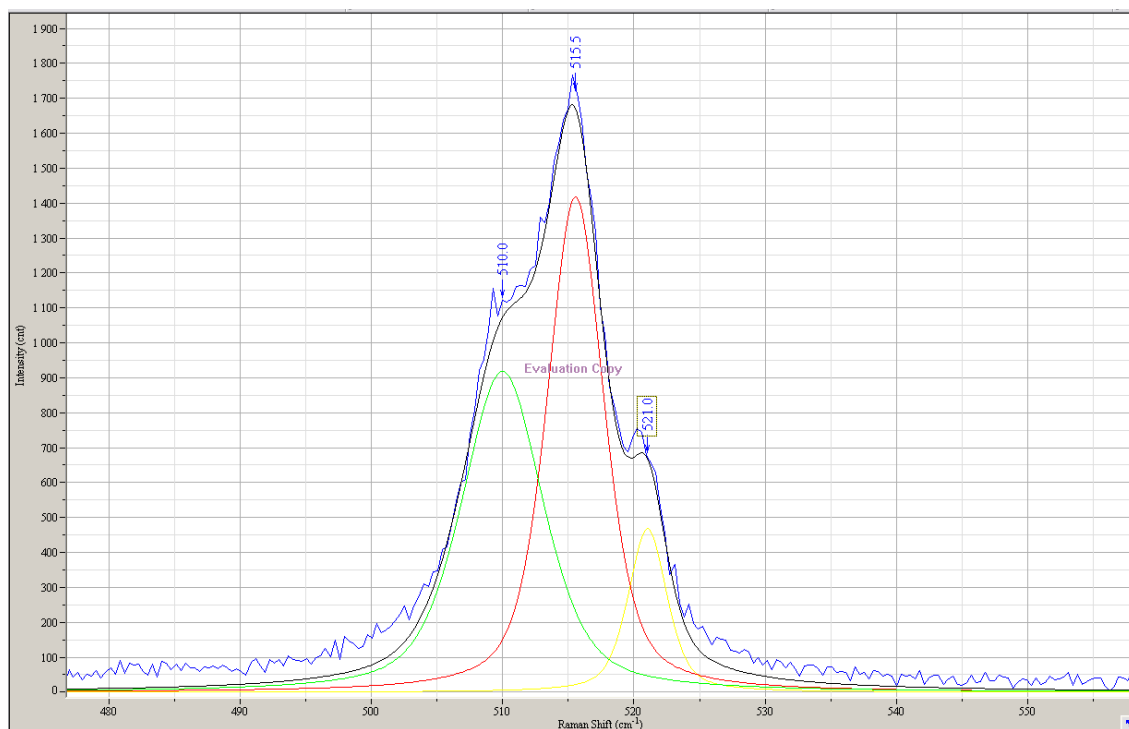


Figure 6.7. Sample D05 was a 4-layer  $\text{Si}_{0.8}\text{Ge}_{0.2}$  virtual substrate with the thickest  $\epsilon$ -Si cap layer of the samples at 80 nm. Samples were provided by Sematech. As per the previous samples, there is no overall enhancement to the signal amplitude. The relative intensities of the  $\epsilon$ -Si peak to the Si in SiGe and Si peaks show a much more apparent surface selectivity. While it was possible to achieve an enhancement with this sample, it was not always reproducible, however, it was much more so than with the previous samples.

The surface selectivity is most clear in the sample with the thickest cap layer. Figure 6.7 shows the peak from the underlying silicon substrate is actually the least intense and

relative to the SiGe peak, the strained layer is much more intense. Relative intensities show the strained Silicon peak is 95% of the SiGe peak on the sample with NPs, compared with 85% on the sample without. The strained Si relative to the Si peak is 105% for the NP sample compared with 93% without. So here, the surface selectivity is very apparent. This effect was more easily repeatable than with the previous samples. Within experimental error, the peak positions are the same in either case. The strained Si peak when NPs are present is at  $514.7\text{ cm}^{-1}$ , whereas without it is  $514.9\text{ cm}^{-1}$ . The Si in SiGe peak with NPs present was  $507.7\text{ cm}^{-1}$  and without;  $508.4\text{ cm}^{-1}$ .

A range of enhancements was seen varying from no enhancement to that described in figure 6.7 above, finally to that depicted below in figure 6.8 below. This figure shows a screen shot of the LabSpec peak fitting software depicting the greatest achievable surface selectivity, with the strained Si layer having the greatest intensity. The SiGe and Si peaks manifest themselves as shoulders on the low and high wavenumber sides of the strained Si peak respectively. The point to notice here is that, while within error, the strained Si peak is the same as the sample without the coating of NPs, the other two peaks have shifted to the right. The spectrum contains quite a lot of noise and as such a lot of potential error in the fitting of the peaks. However, there is an unmistakable relative enhancement of the strained Si peak, which was only achieved for this measurement. Setting the Raman microscope to measure in the same place gave a spectrum without the same enhancement. More detailed investigation into the locations, size and amount of NPs is required.

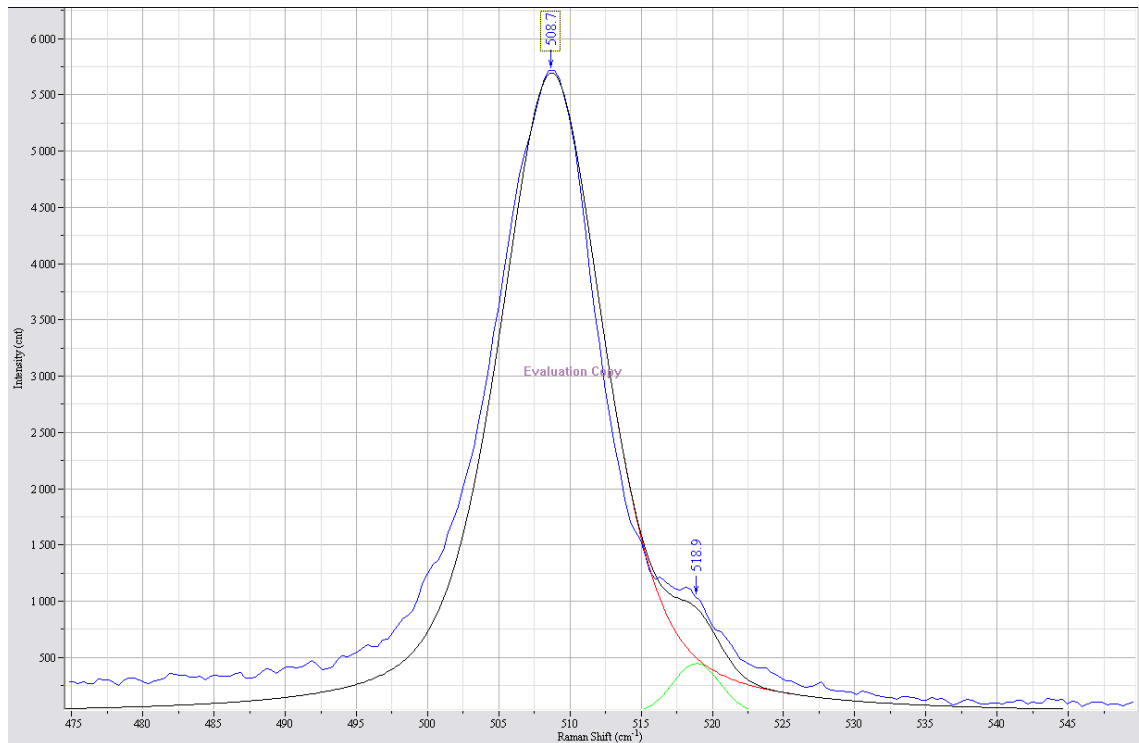


**Figure 6.8.** A LabSpec screen shot of a spectrum taken using the D05 sample described previously shows it is possible to get total surface selectivity using this SERS technique. Most spectra, however, were much more like that shown in figure 6.7. A slight peak shift in the Si and Si in SiGe peaks was noted.

## 6.5. Graded Ge

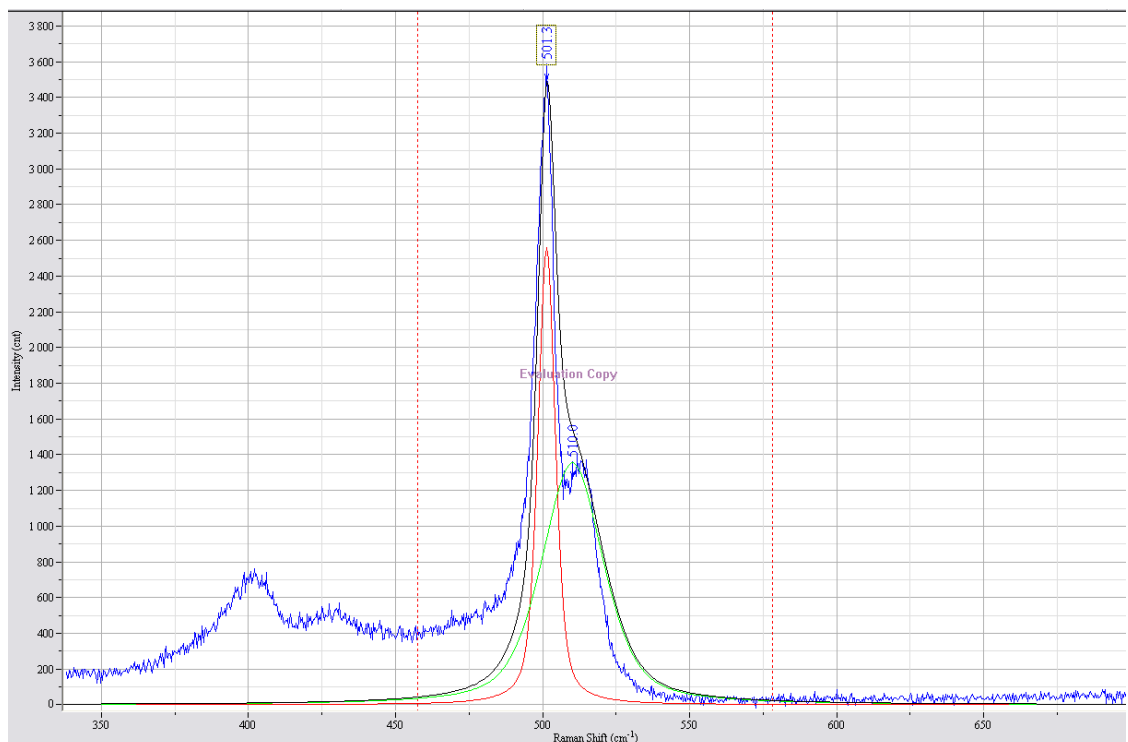
The next part of the investigation looked at replicating the calibration curve described in chapter 4 using the surface enhanced signal acquired via the methods used above. Au NPs were deposited onto the samples as with the previous samples and the experimental setup was identical.

Figure 6.9 below shows the signal collected from the  $\text{Si}_{0.9}\text{Ge}_{0.1}$  sample. Several spectra were taken from several areas of the sample and enhancement was only achieved once. The Si in SiGe peak has the highest amplitude, however, instead of simply being a small shoulder easily mistaken for noise, the strained Si peak manifests itself as a much more obvious peak. The Si in SiGe peak position based on empirical data for 10% Ge content is  $\sim 514 \text{ cm}^{-1}$ . The large shift in peak position shown here is unaccounted for.



**Figure 6.9.** A LabSpec screenshot of the 10% Ge spectrum shows a relatively obvious  $\epsilon$ -Si peak when compared to the conventional Raman spectroscopy spectrum.

Despite several spectra being taken for each Ge content, it was not possible to achieve an enhancement for any sample other than the minor, somewhat unconvincing enhancement shown in figure 6.9 and in figure 6.10 below, using the  $\text{Si}_{0.7}\text{Ge}_{0.3}$  sample.



**Figure 6.10.** A LabSpec screenshot of the 30% Ge shows a definite  $\epsilon$ -Si peak instead of the small shoulder usually observed with conventional Raman spectroscopy.

Figure 6.10 shows a definite peak compared with the small shoulder seen in the calibration chapter 4. There is a slight shift in strained Si peak position which can be accounted for by the noise on the spectrum around the peak giving fitting errors. Smoothing the spectrum leads to large peak shifts and so only raw data is shown.

Most of the minor shifts in peak position can be explained by natural variation and noise causing large peak fitting errors. There was no enhancement in the amplitude of the signal collected due to the presence of the Au NPs. For the spectra collected, the overall signal is less intense. This can be explained by the diameter of the laser spot compared to the nanoparticles. The far field signal was not polarised as it would be in the case of TERS, and so a lot of signal was being collected from the area surrounding the NPs. Where the NPs were giving more surface selectivity, this was competing with the far field signal, and so a strong background signal from the laser was also collected. Nevertheless, there is a shift in the relative intensities with the strained silicon peak being enhanced slightly. The enhancement is not consistent and not easily repeatable; some spectra show an enhancement, often the signal to noise ratio means the peaks are not easily visible. The reason for the repeatability of the enhancement on plain silicon can possibly be explained due to it being a single crystal sample with no epitaxial layers, however, at present the cause is unclear.

## **6.6. TERS**

The TERS experimental setup is described in chapters 2 and 3. Some preliminary tests were carried out to establish what is achievable. The 514 nm laser was used on a plain Si sample and the sample D05, as in the above investigation. In order to guarantee the signal collected is from the area directly under the tip apex, the sample has to be polarised to block out the far field signal as much as possible. When the tip is away from the surface, very little signal should be seen.

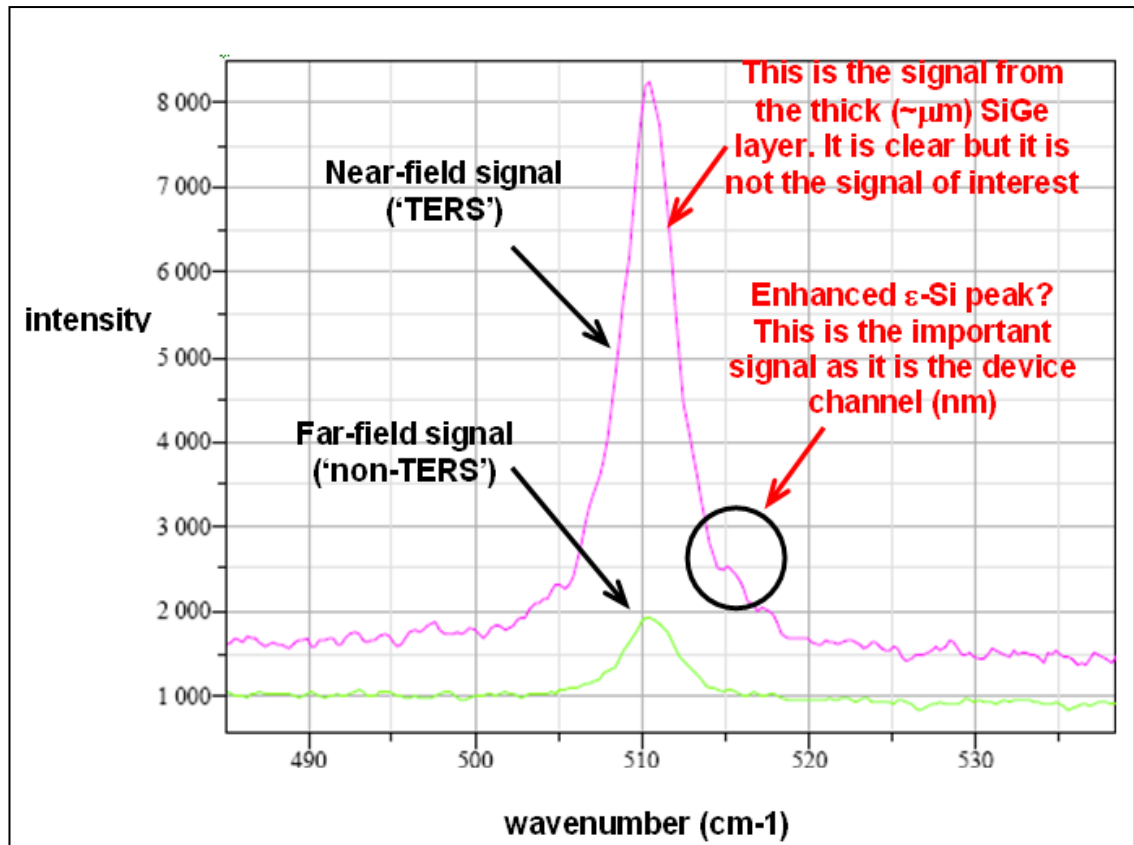
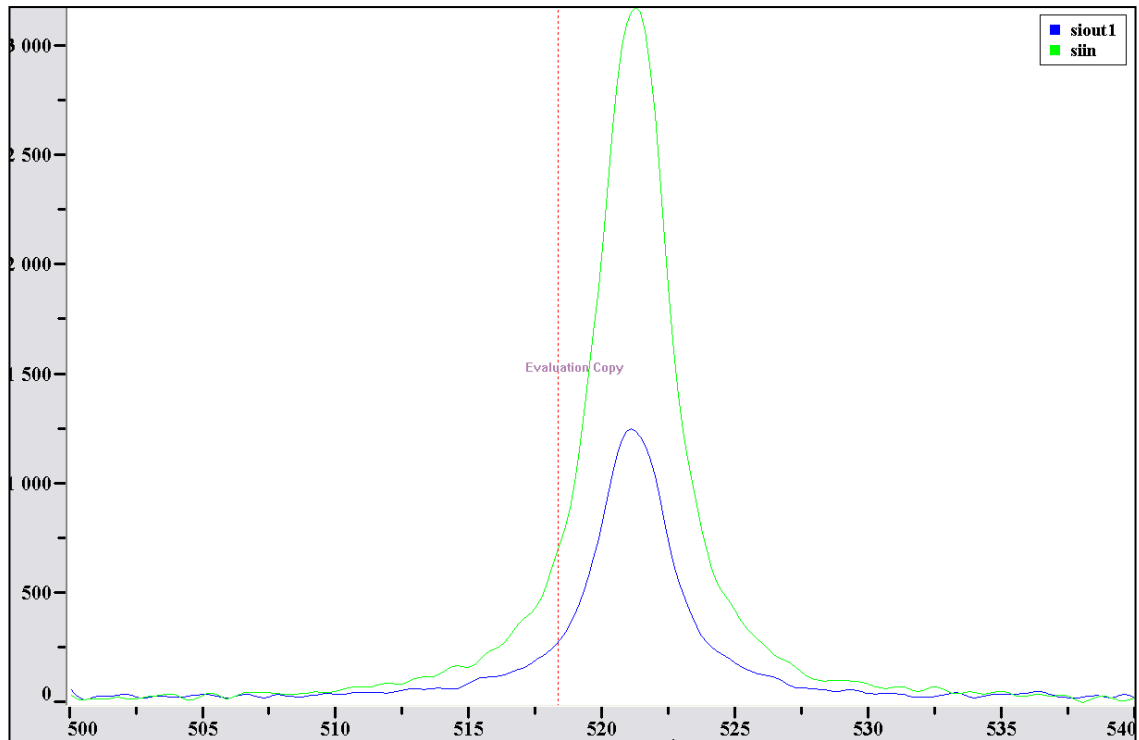


Figure 6.11. The initial TERS spectrum taken with the set up described in chapter 3 using a sample provided by Imperial College. An enhancement from the thick SiGe virtual substrate is noted, however, there is no apparent surface selectivity.

The spectrum in figure 6.11 above shows an enhanced signal for 15nm  $\epsilon$ -Si on relaxed  $\text{Si}_{0.85}\text{Ge}_{0.15}$  grown by Imperial College. The TERS Si in SiGe peak is greatly enhanced compared to the non-TERS, far-field signal. The  $\epsilon$ -Si cap layer peak, however, does not show the same enhancement. Because TERS is a surface selective effect, this signal should also be greatly enhanced with a lesser enhancement of the Si in SiGe peak. This could be due to the equipment set up or the tip used. As the thickness of the  $\epsilon$ -Si cap layer increases, the enhancement should be seen more from the surface. This is not ideal as when the thickness increases above the critical thickness, some relaxation occurs in the sample. Clearly, this is not practical for real devices.



**Figure 6.12. Plain silicon, near-field comparison with far-field. As with SERS it is significantly easier to reproduce this enhancement using a single crystal sample as opposed to the multi-layer SiGe samples.**

Figure 6.12 shows a small enhancement with a plain silicon sample. The ‘enhanced’ near-field peak is approximately 200% the size of the far field. However, as with SERS, an enhancement on a single crystal, thick structure is not as difficult as with a thin epitaxial layer. Being able to achieve an enhancement with such a structure holds no real benefit to the applications TERS is required for.

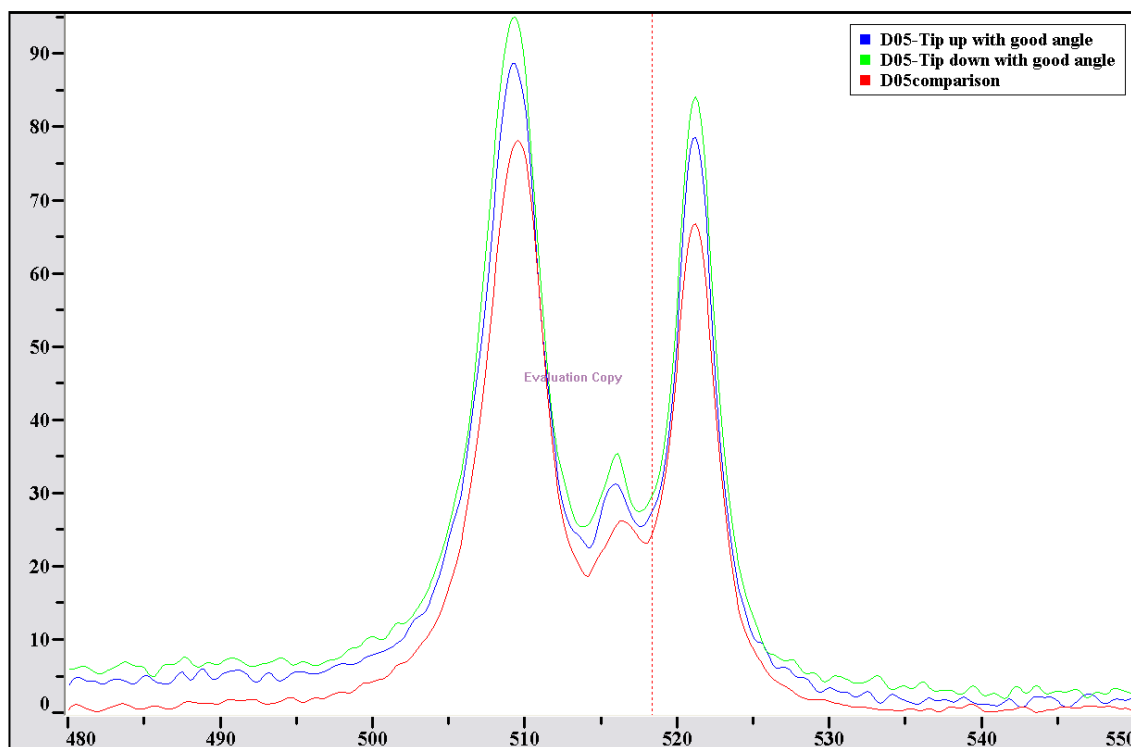


**Figure 6.13.** A LabSpec screenshot showing a comparison of spectra between near-field, far-field spectra and with a depolarised sample.

Figure 6.13 shows a comparison between the near-field and far-field spectra, as well as a spectrum taken with the sample at a slightly different angle, so not fully polarised. A very minor increase in intensity is seen between the near-field and far-field signals. However, when the tip is removed and the sample is turned slightly, the intensity drops marginally. When the polarisation is set up properly, this intensity will be at its lowest. The ‘tip up’ far-field spectrum shows the sample wasn’t polarised fully before the measurement was undertaken. What this shows is that it is possible to get similar levels of so called enhancement just by altering the polarisation of the sample. This highlights the importance of proper machine set up and calibration otherwise there is a high chance that the reported enhancement is false and is a product of poor setup rather than the TERS effect. Depolarization effects on the signal obtained are discussed in literature [Martin, 1997, Merlen, 2009, Poborchii, 2009].

Considerable effort was made to optimise conditions to get enhancements in all the samples tested for SERS and TERS but in no case did the level of enhancement justify the effort put in. It is unlikely that this will be a commercially viable analysis technique for these strained samples unless a different method of enhancement (e.g. a different nanoparticle or tip coating) is employed.

## 6.7. Summary

What is clear from these results is that, unlike several of the SERS results, there is little evidence to support TERS as surface selective technique. When dealing with TERS, there are several more variables to consider than with conventional Raman Spectroscopy or even SERS. Firstly, and arguably most important is the sample polarisation. In order to get the true TERS effect, the far-field signal needs to be blocked as much as possible. What these results show is that it is possible to achieve similar levels of enhancement to that shown and even those published simply by altering the sample set up slightly.

These results as well as a distinct lack of available literature on TERS for silicon suggests there is still extensive work required until it is a workable technique outside of a research environment. For both TERS and the proposed non-destructive SERS technique factors such as NP structure, location and material need much more investigation to optimise the enhancement. When thinking solely about TERS, optimum machine set up, tip fabrication and angle and correct polarisation of the sample need also to be considered.

The investigations in this chapter were conducted with gold as the material for the nanoparticles and the 514 nm excitation line. By virtue of the fact the penetration depth is smaller, using a 457 or 488 nm laser with Ag NPs would naturally provide more surface selectivity and may be the key to providing the surface selectivity required for looking at such thin layers of  $\epsilon$ -Si.

Nevertheless, until such work is carried out, the results of chapter 5 perhaps show there is promise that conventional Raman Spectroscopy is capable of significantly more precise measurements on small structures than thought previously. Where more surface selectivity is required, and once optimised, it may be possible to incorporate non-destructive SERS into a semiconductor manufacturing line, should silver prove to give similar results.

FEOL has been considered in some depth over the previous 3 chapters. Chapter 7 will discuss the techniques available to characterise BEOL processes, concentrating on EBSD and nanoindentation of copper thin films and bulk material. How this relates to copper interconnects in a semiconductor device is considered.

## Chapter 7. Mechanical assessment of copper metallisation at high spatial resolution

### 7.1. Introduction

As discussed in the review of the literature, copper is now used extensively in modern, state of the art microelectronics devices in place of aluminium. Using a new material always brings problems with it, and these problems have been highlighted as delamination, blistering, peeling, cracking etc. On top of this, stress and strain play an important role in the reliability of the interconnects and these properties need to be fully characterised on samples processed under the conditions they will see throughout the manufacturing process.

One of the most important properties of Cu and one of the main causes of the problems mentioned above is its microtexture. Traditionally used Al does not have the same problems seen with copper as aluminium is much more isotropic, therefore there are no orientation issues. That is, all crystallographic axes are similar enough for there not to be any real differences in properties based on this. This is not the case with copper which is a very anisotropic material as shown in figure 7.1. It will be shown in this chapter that properties such as hardness and elastic modulus are different depending on the orientation of the sample.

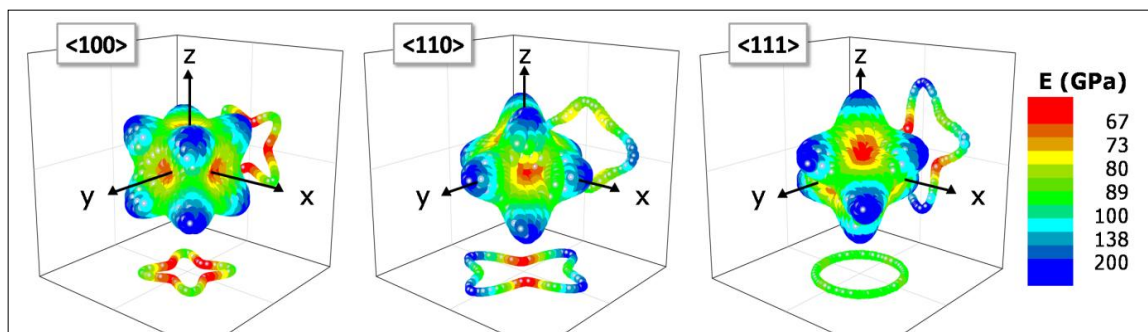


**Figure 7.1. Copper is a highly isotropic material. This diagram shows the change in elastic modulus with a change in crystallographic orientation [Wilson, 2009].**

Cu has a higher melting point than Al, however, the atomic mobility even at room temperature is such that it allows grain growth. When subjected to anneals similar to those seen in a semiconductor processing line, microtexture can be greatly affected. This influences thermal, electrical and mechanical properties of the thin Cu film when interconnect widths fall below approximately 0.5  $\mu\text{m}$ .

Issues arise with characterisation as conventionally, the grain size of the deposited material is very much smaller than the feature size, i.e. the interconnect. With deep submicron interconnects in the order of 100nm, this is no longer the case. Image 7.2 shows the formation of a structure where the diameter of each individual grain is somewhat larger than the width of the interconnecting wire, thus forming a bamboo like structure. The following chapter will discuss the stresses and strains that act on structures such as this and on polycrystalline interconnects.

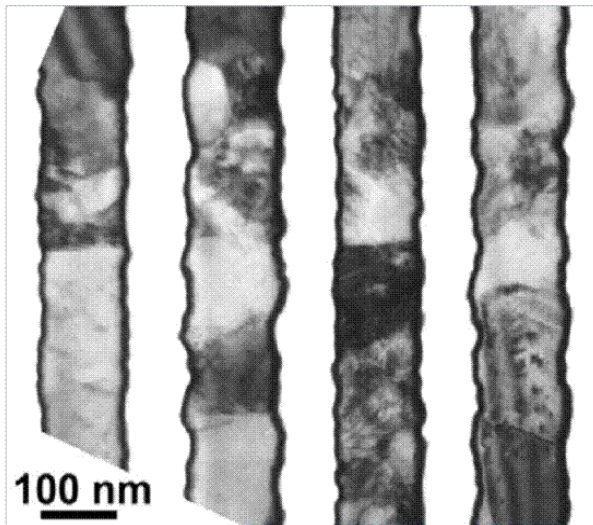


**Figure 7.2.** TEM image of 100 nm wide Cu interconnects. The grain structure in these narrow interconnects where grain size is often much wider than the width of the wire is approaching what is known as a bamboo structure.

The aim of this chapter is to investigate how the bulk properties of copper relate to the thin film properties of samples annealed under conditions that mimic those in a process line. Ultimately, the properties of actual interconnects need to be known. It is important to understand the properties of bulk Cu and thin Cu films before full understanding of the interconnects can be achieved. Differences in grain size and orientation, and material properties under the different anneal conditions are analysed in order to predict what this means for real devices. Perhaps most important is ensuring that the data obtained from experimentation is reliable.

Nanoindentation has been used extensively to extract properties of grains at different orientations. The issues that have arisen include the need to identify if it was single crystal, continuum or bulk behaviour being witnessed. Where the indent size is very much larger than the grain size, it is not possible to use this data to show single crystal behaviour so the question of how to interpret this data arises. If the indent size is comparable to the grain size, there is still the issue of plastic zone size. The plastic zone

size extends very much beyond the indent size. Here, whether the data gathered is just from the copper, or if there is an influence from the substrate as well needs to be considered.

What these problems show is that it can be difficult to obtain good data by nanoindentation at this scale. There are also issues due to pile-up, discussed in the nanoindentation results. Data from low load indents show that the optimum indent depth is 40 – 100 nm to avoid interference from pile-up. The effect of the plastic zone area is analysed.

## **7.2. EBSD Results**

Results were obtained with an FEI XL-30 ESEM FEG (field emission gun) equipped with EBSD (HKL Technologies). To acquire the EBSD maps, the sample was tilted 70 degrees toward the phosphor detector.

Four samples were used, each with 800 nm of Cu deposited on a silicon substrate. The samples were then subjected to different anneal conditions similar to those that would occur in a semiconductor production process. One sample received no anneal and was as deposited, the other conditions were 100°C for 60 minutes, 180°C for 30 seconds and 350°C for 60 seconds. The samples were provided by IMEC. For each sample, a series of four 5µm by 5µm maps were taken to create one larger map. Taking smaller individual maps allowed for data to be gathered over a larger area while eliminating the effect from stage drift often seen on larger maps.

The working distance was set to below 25 mm, the electron beam was 10 keV and the spot size was set such that the highest intensity signal was obtained without compromising the speed of measurement that can also cause stage drift.

The electron backscatter patterns (EBSPs) generated from the maps were used to build up inverse pole figure (IPF) maps, or texture maps, as per the following results section. EBSPs are made up of Kikuchi bands, which relate to the crystallographic orientation of the sample. Each pattern obtained within the area of the sample being analysed is indexed by the software. This involves Kikuchi band location, determining the angle between the bands and comparing these to theoretical values. Once this is done, the phase can be determined. The identified bands are indexed automatically. The system

stores a variety of data from each point on the map that can be processed further to generate texture maps [www.stanford.edu, 2012].

An IPF map shows colour coded pixels according to the orientation of the sample, or section of sample. This colour coding is described by the unit triangle of the IPF map, an example of which is shown in figure 7.4. [Schwartz, 2000].

### 7.2.1. No Anneal

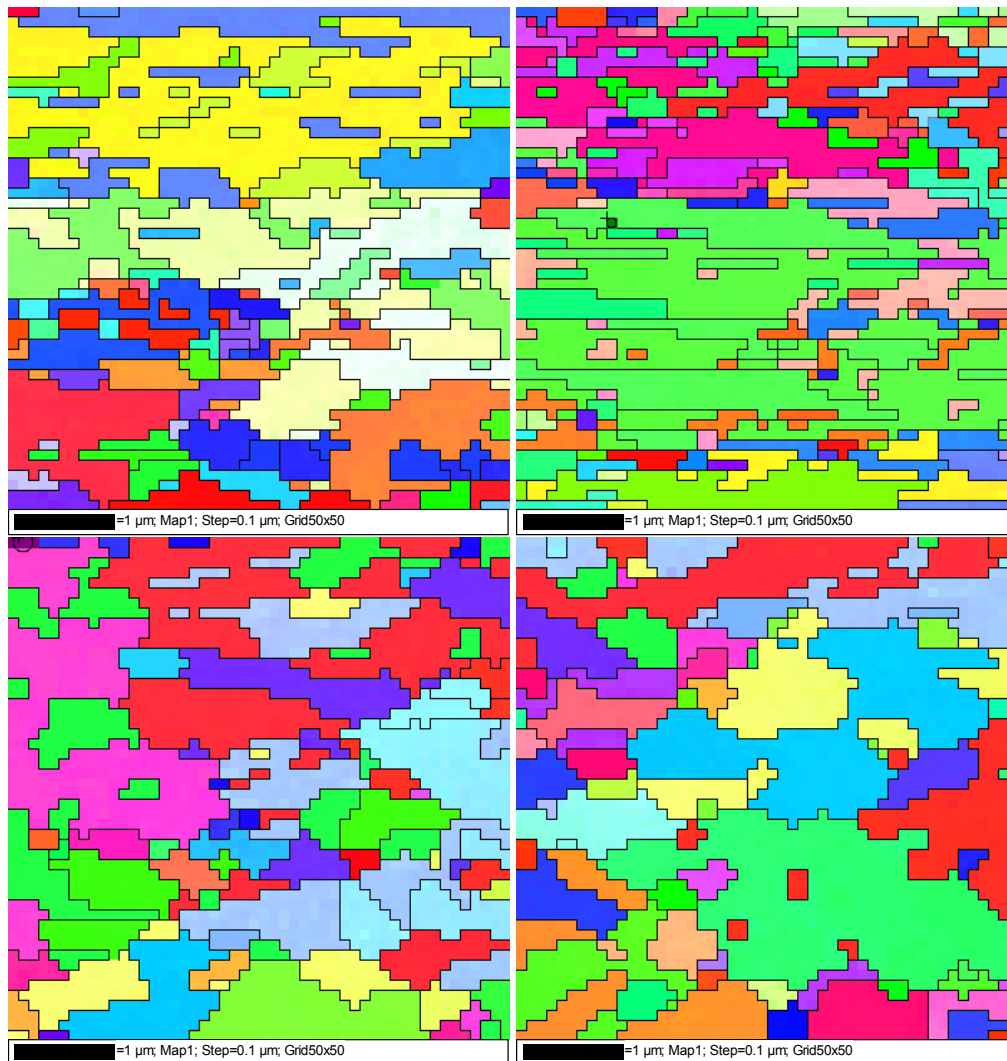


**Figure 7.3.** Cu film as deposited with no anneal. A series of four 5 μm x 5 μm EBSD maps were taken and show a mix of large and small grain size characteristic of an as deposited sample.

Figure 7.3 shows the EBSD maps obtained from the as deposited sample with no anneal. The inverse pole figure in figure 7.4 and table 7.1 show the as deposited sample favours (101) grain growth.

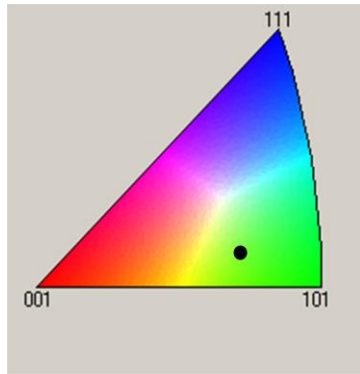


**Figure 7.4.** Inverse pole figure showing the crystallographic orientation of the Cu grains on the sample with no anneal.

<b>Orientation</b>	<b>% area exhibiting orientation</b>
100	33
111	16
101	51

**Table 7.1.** Crystallographic orientation of the sample with no anneal

### 7.2.2. 100°C 60 Minute Anneal

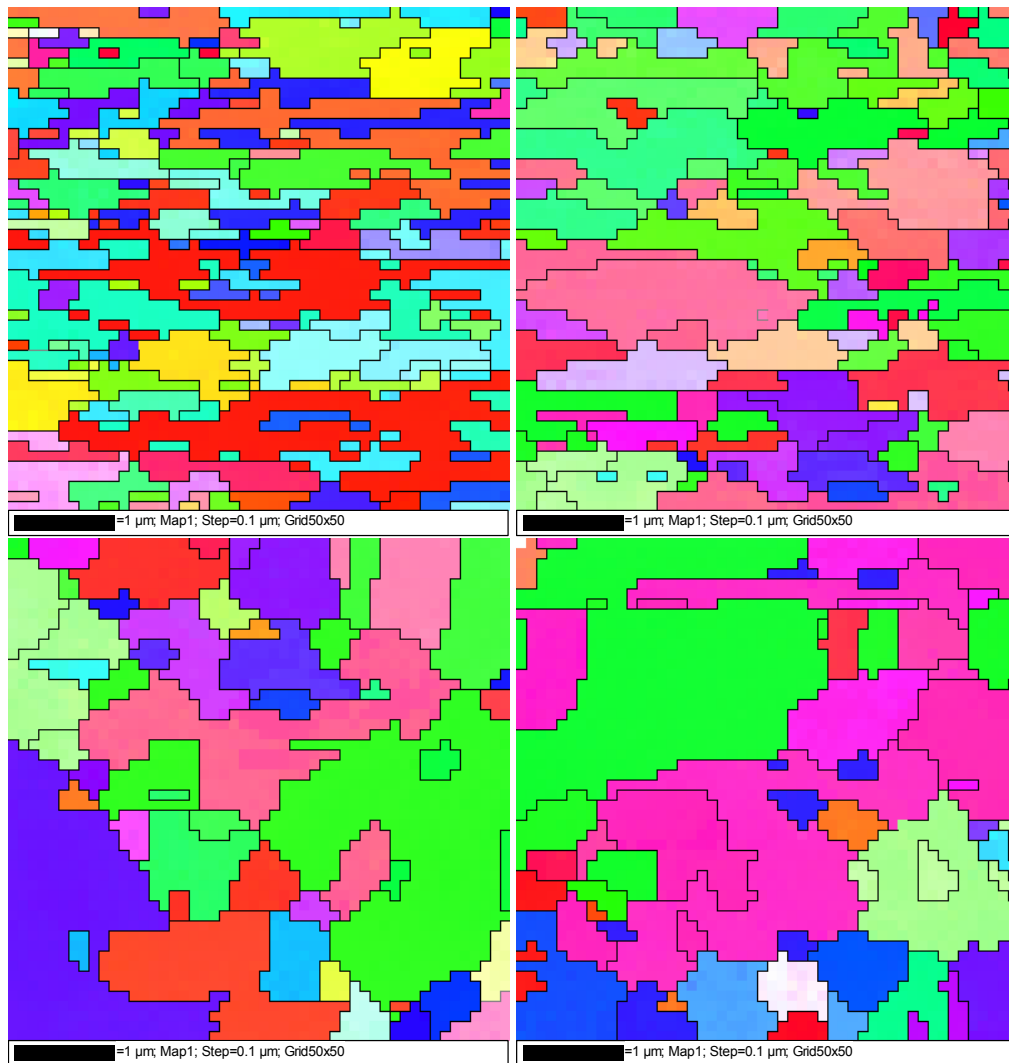


Figure 7.5. Cu film annealed at 100°C for 60 minutes. A series of four 5 μm x 5 μm EBSD maps were taken and showing some larger grains beginning to grow.

Figure 7.5 shows the EBSD maps obtained from the sample annealed at 100°C for 60 minutes. The inverse pole figure in figure 7.6 and table 7.2 show the crystallographic orientation has begun to take on more of a (001) texture. Some larger grains are starting to grow at this anneal temperature.

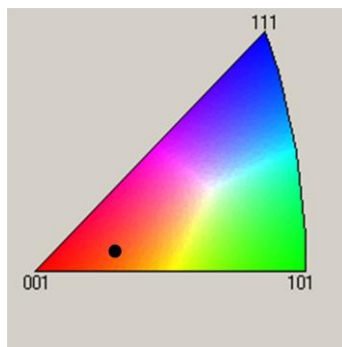


Figure 7.6. Inverse pole figure showing the crystallographic orientation of the Cu grains on the sample annealed at 100°C for 60 minutes.

Orientation	% area exhibiting orientation
100	57
111	8
101	35

Table 7.2. Crystallographic orientation of the sample annealed at 100°C for 60 minutes.

### 7.2.3. 180°C 30 Second Anneal

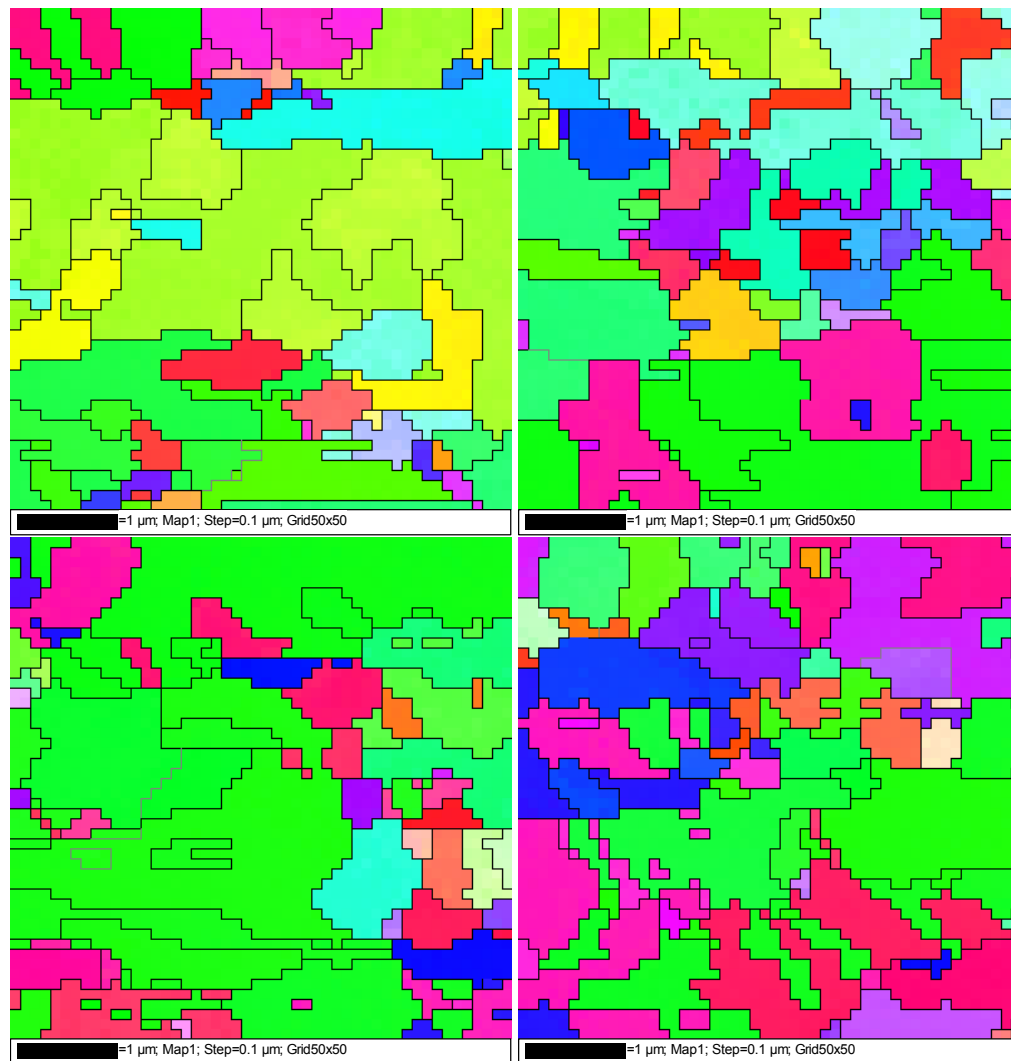


Figure 7.7. Cu film annealed at 180°C for 30 seconds. A series of four 5 μm x 5 μm EBSD maps were taken and showing larger grain sizes.

Figure 7.7 shows the EBSD maps obtained from the sample annealed at 180°C for 30 seconds. The inverse pole figure in figure 7.8 and table 7.3 show the crystallographic orientation a strong (101) texture and the higher temperature has caused large grain growth.

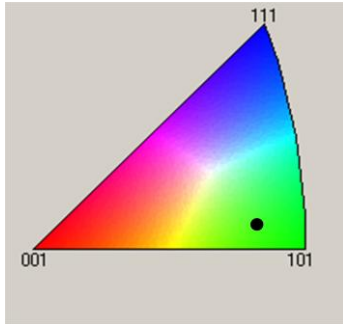
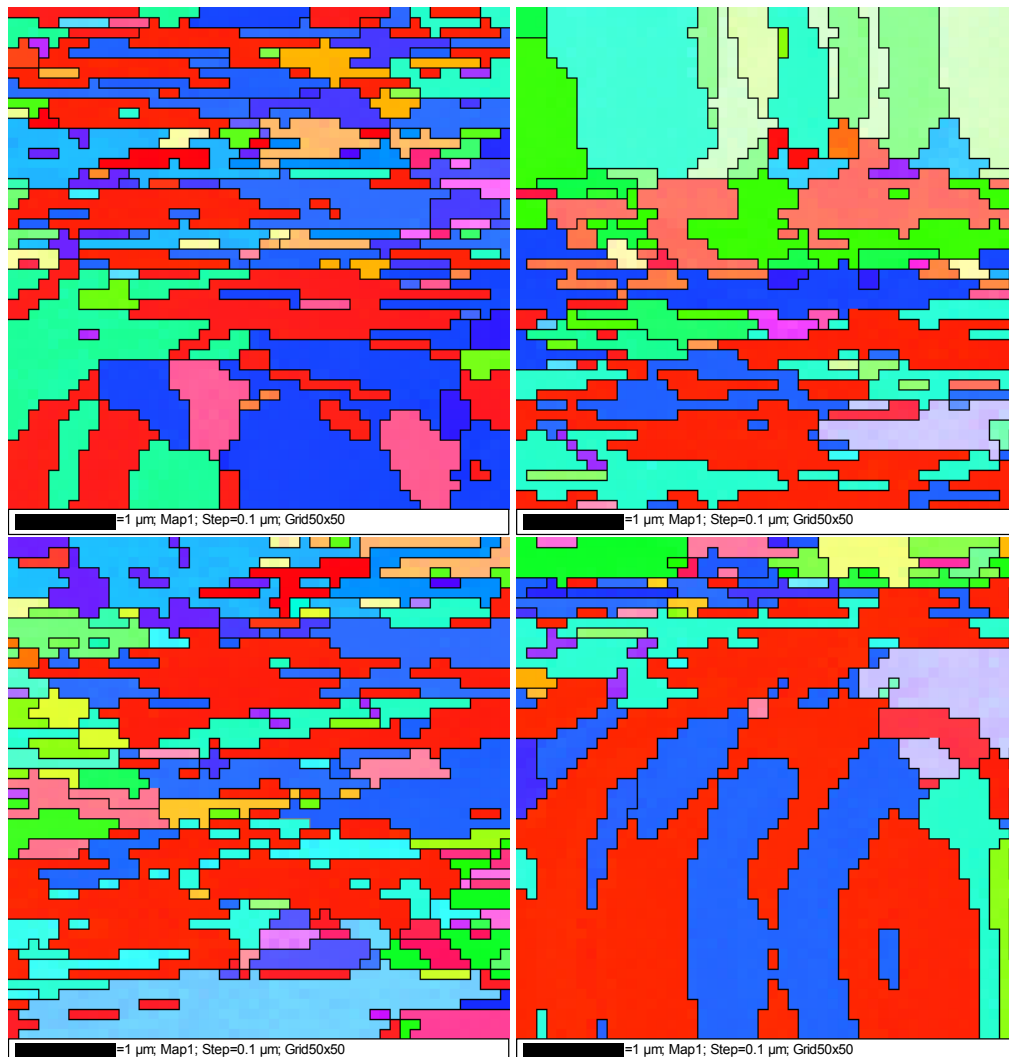


Figure 7.8. Inverse pole figure showing the crystallographic orientation of the Cu grains on the sample annealed at 180°C for 30 seconds.

Orientation	% area exhibiting orientation
100	22
111	12
101	66

Table 7.3. Crystallographic orientation of the sample annealed at 180°C for 30 seconds.

#### 7.2.4. 350°C 60 Second Anneal



**Figure 7.9. Cu film annealed at 350°C for 60 seconds. A series of four 5 µm x 5 µm EBSD maps were taken and showing some recrystallisation is beginning to occur.**

Figure 7.9 shows the EBSD maps obtained from the sample annealed at 350°C for 60 seconds. The inverse pole figure in figure 7.10 and table 7.4 show the crystallographic orientation shows a (111) texture and some recrystallisation begun to occur.

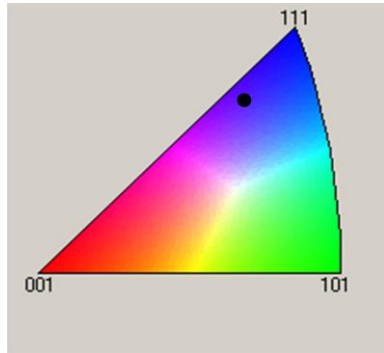


**Figure 7.10. Inverse pole figure showing the crystallographic orientation of the Cu grains on the sample annealed at 350°C for 60 seconds.**

Orientation	% area exhibiting orientation
100	37
111	51
101	12

**Table 7.4. Crystallographic orientation of the sample annealed at 350°C for 60 seconds. The orientation results from the final map are omitted due to the significant drift seen**

### 7.2.5. EBSD Discussion

Anneal temperatures in industry can reach up to 500°C and so the effect of annealing on microtexture needs consideration. An as deposited thin Cu film that has undergone no anneal with contain a range of large and small grains. When the Cu film is subjected to heat, larger grains will grow as the temperature increases. High temperature annealing leads to a (111) grain orientation in FCC materials.

The results above show the overall crystallographic orientation of Cu film on each of the four samples. The texture moves towards (111) orientation with an increase in anneal temperature. The nanoindentation results in the following section will link this orientation to the elastic modulus, E. At low annealing temperatures, there is a reduction in the amount of fine grains seen because it is energetically favourable for small grains to disappear first. The percentage of (111) grains present increases as the anneal temperature increases, shown in figure 7.11. The 350°C anneal generates some recrystallisation and a large increase in the amount of (111) grains is observed.

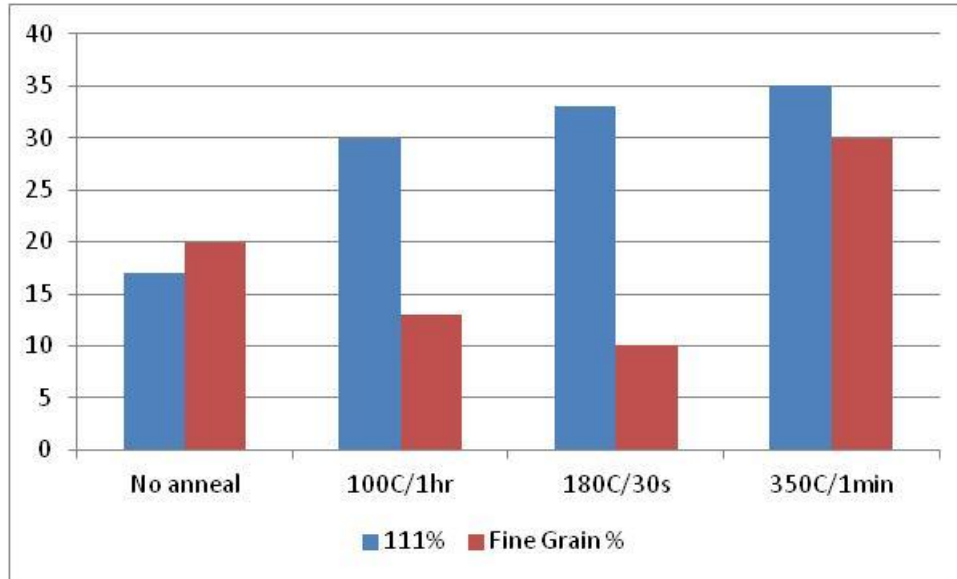


**Figure 7.11. (111) grains grow at the expense of fine-grained material for low temperature anneals. The anneal at 350°C generates some recrystallisation with a higher percentage of fine grains and a strong (111) texture.**

EBSD can be used to determine effect of anisotropy on measured data. Ideally, the same set of experiments needs to take place on deep submicron interconnects. This has already taken place on older technology, however, although theoretically possible, due to signal to noise ratio and factors such as stage drift, it is difficult to obtain good EBSD data on such small feature sizes.

The grain size and orientation of thin (800 nm) Cu films annealed at various temperatures have been measured by EBSD. The next section will examine the same set of samples with nanoindentation.

### **7.3. Nanoindentation Results**

In nanoindentation, a load is applied to an indenter tip in contact with the sample at a specified rate. As the load is applied, the penetration depth is measured. A measure of the contact area between the tip and sample surface is taken, that along with the shape and angle of the tip allows calculation of the sample hardness. This is done by dividing the maximum applied load with the measured contact area. In the nanoindentation data analysis, the method first proposed by Oliver and Pharr [Oliver and Pharr, 1992] is the most common technique to calculate hardness and Young's modulus. More information on this technique can be found in [Fischer-Cripps, 2004].

Indentations were performed on a Hysitron Triboindenter with a Berkovich tip with an effective 100 nm radius, shown schematically in figure 7.12.

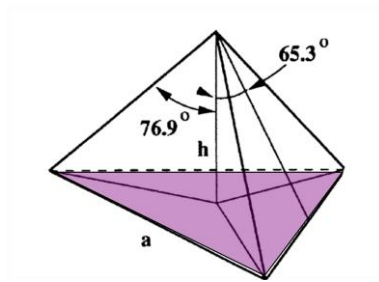


Figure 7.12 Schematic of a Berkovich tip

The Berkovich tip has a three-sided pyramid shape capable of producing well-defined plastic deformation in sample surface. The Berkovich tip is usually used for bulk materials and thin films in excess of 100 nm thick.

Multicycling (load/partial-unload) and single cycle tests were carried out as per figures 7.13 and 7.14 under load control to obtain material properties versus depth. The hardness and Young's modulus were obtained using the Berkovich indenter.

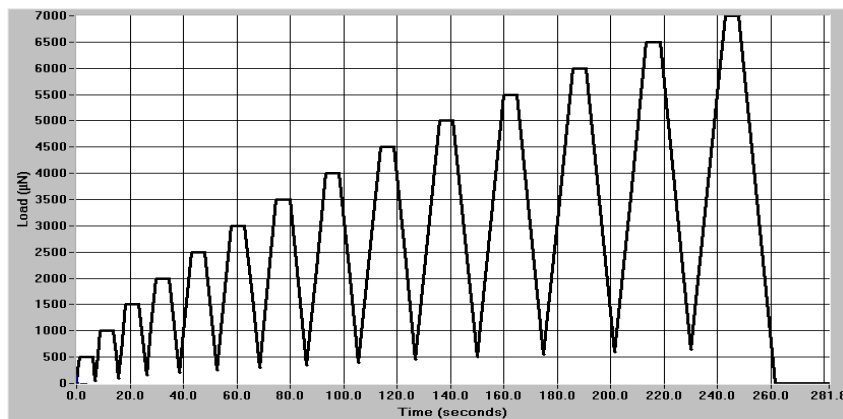


Figure 7.13. Multicycling load versus time experimental set up for a load/partial-unload cycle

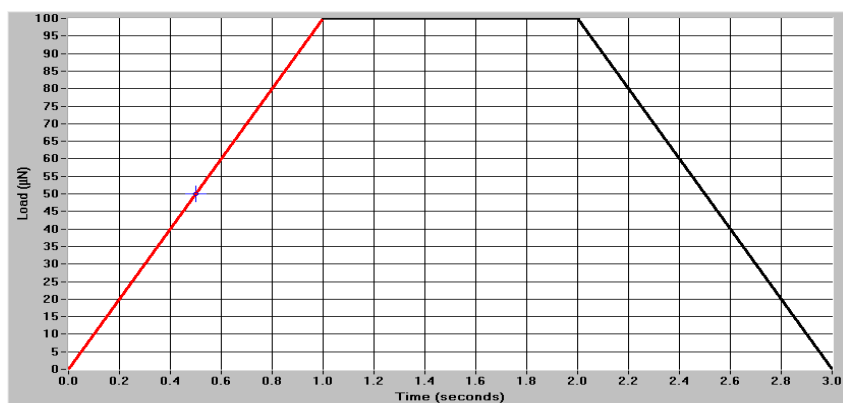
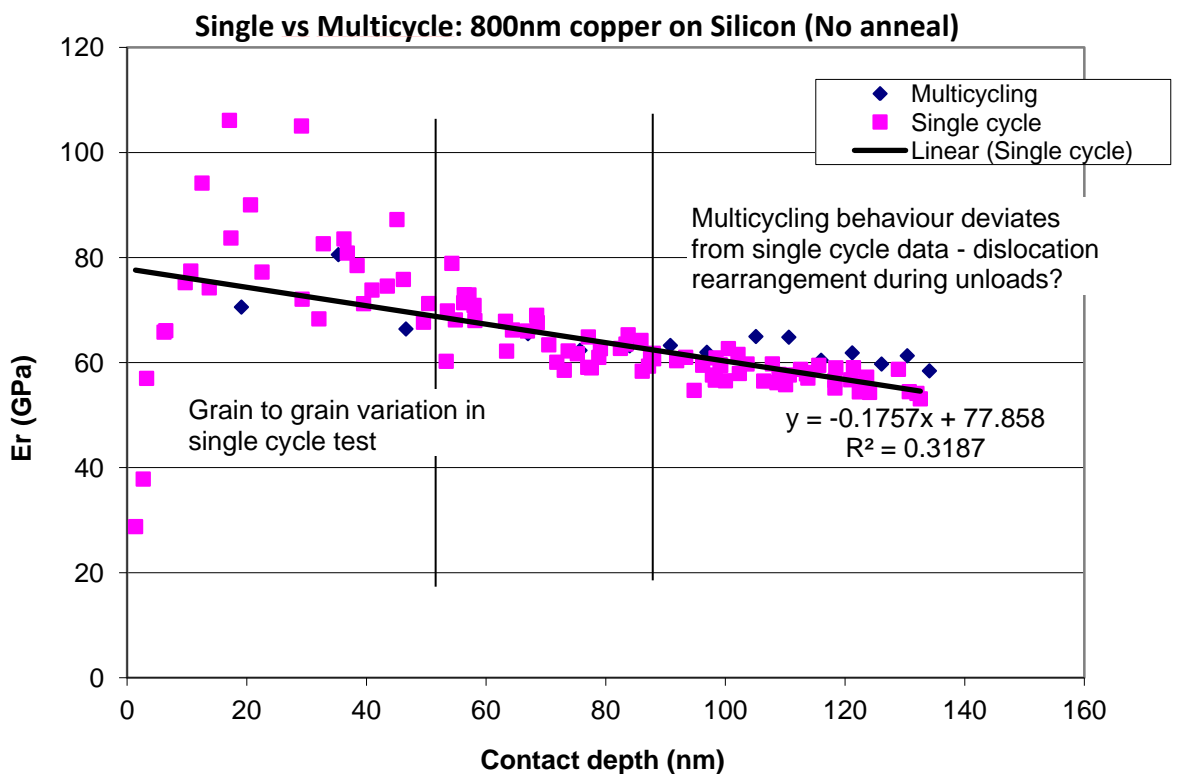


Figure 7.14. Single cycle load versus time experimental set up.

Figure 7.15 compares the single and multicycling indentation for the as deposited, no anneal sample. At higher contact depths,  $h_c$ , the multicycling behaviour deviates from single cycle data. This can be caused by rearrangements of the dislocations caused during the unload. There is a lot of scatter at low contact depths caused by grain to grain variation. Contact depths between approximately 60 – 100 nm shows almost complete agreement between the single and multicycling data implying that this depth is the optimum for obtaining reliable results. This will also ensure there is no influence on the results from the underlying silicon substrate.



**Figure 7.15. Single versus multicycling data. At contact depths between approximately 60 – 100 nm, multicycling data agrees with single cycle, implying this is the optimum depth for reliable data.**

Figure 7.16 shows the data obtained on the sample with no anneal, however this behaviour was observed for all four samples. There was no real difference no significant difference between single indent and multicycling tests. The pile up width increases linearly with contact depth.

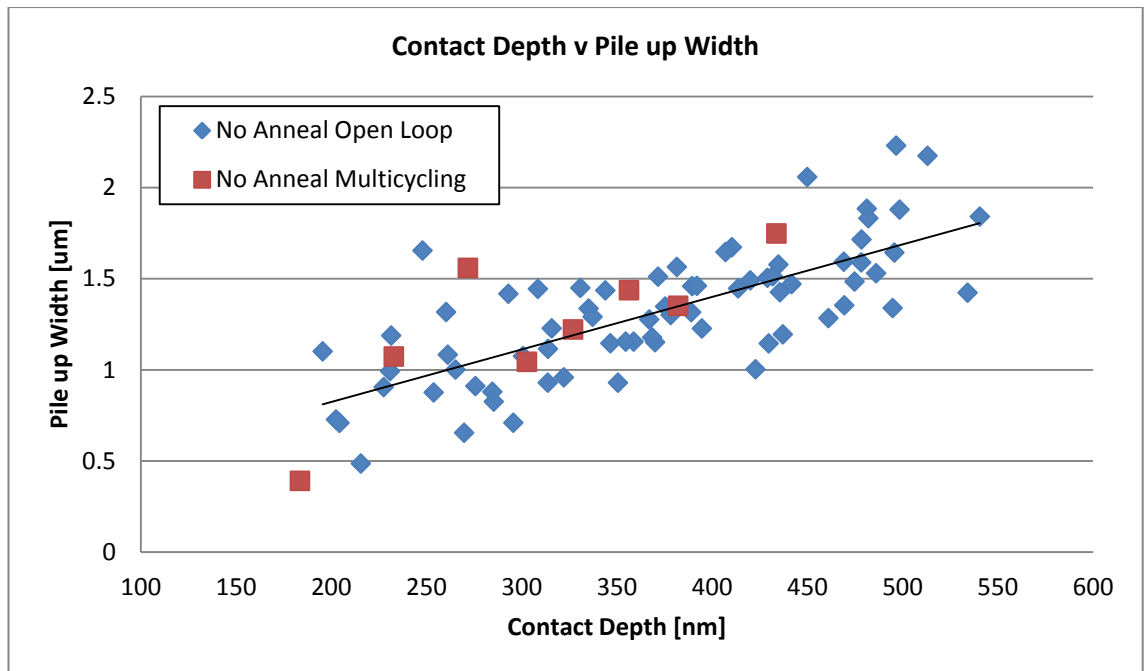
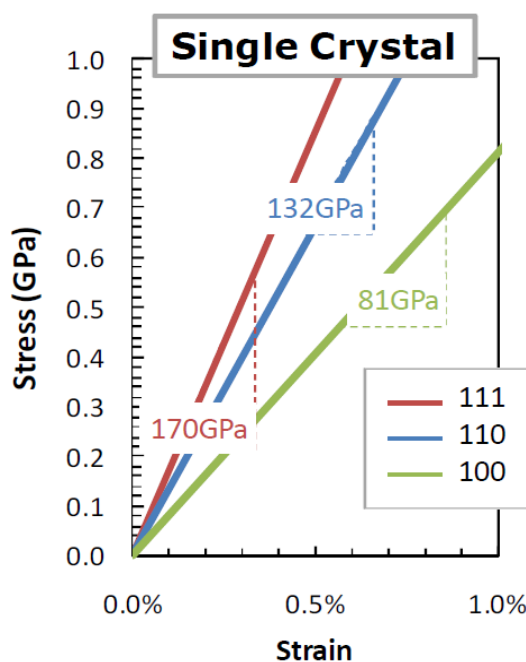


Figure 7.16. Contact depth vs. pile up width for the sample with no anneal. Pile up width increases linearly with contact depth, this behaviour was observed with all four samples.

Bulk copper data shows an elastic modulus of 80 – 170 GPa depending on orientation. Theoretical calculations give indication of the Young’s modulus expected when measuring at different crystallographic orientations. Figure 7.17 shows bulk Cu, single crystal values. This data shows (111) orientation to be stiff with a high modulus, (100) orientation is less stiff with a low modulus. This data is valuable in interpreting experimental data obtained from the thin Cu films. Grains tested with different orientations to those shown could give any value in between.



**Figure 7.17. Theoretical calculations of Young's modulus at different crystallographic orientations on single crystal, bulk silicon**

The elastic modulus,  $E_r$  versus contact depth for all four samples is plotted in figure 7.18. The elastic modulus decrease with contact. The sample annealed at 350°C exhibits the highest modulus which agrees with the theoretical data shown in figure 7.17, with the highest modulus on (111) grains. The 100°C and 180°C annealed samples are displaying (100) behaviour which somewhat agrees with the EBSD data. The sample annealed at 100°C shows strong (100) texture according to EBSD, however, the 180°C annealed sample exhibits stronger (101) orientation. This deviation in results between EBSD and nanoindentation is likely to be due to the small grain size. There is still a high presence of (100) grains and it is not possible to pick out specific grains with a specific orientation to indent. The no anneal sample agrees with the EBSD data, showing (101) behaviour.

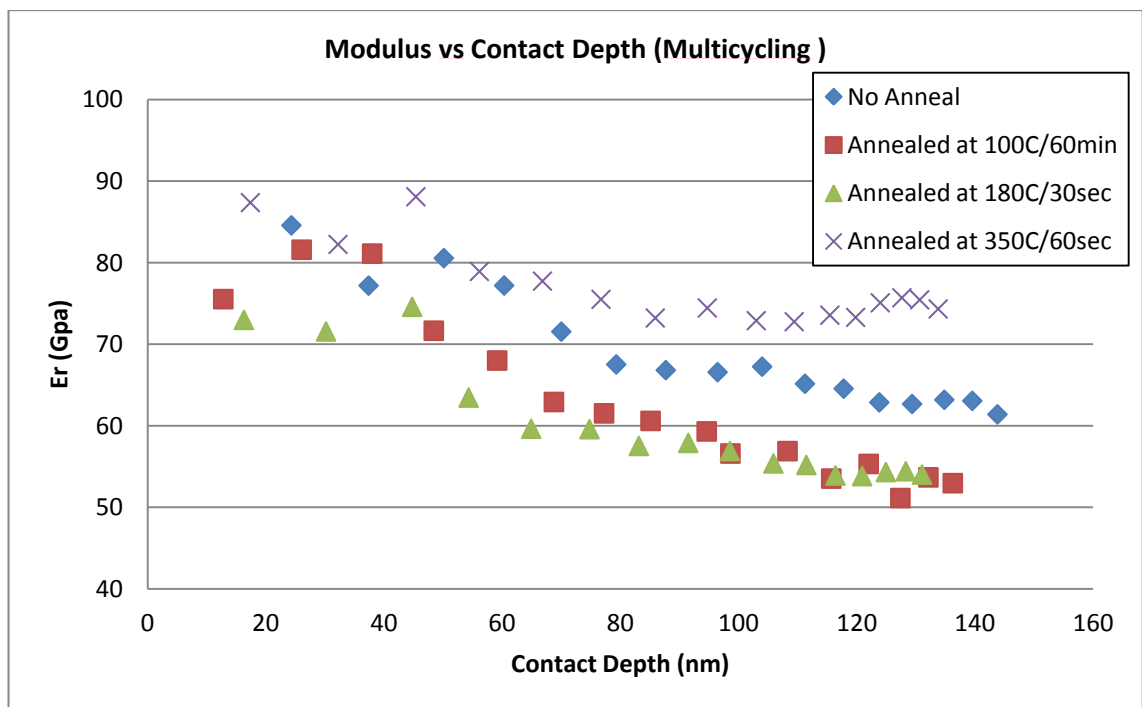


**Figure 7.18 Elastic modulus vs. contact depth. The no anneal sample shows (110) behaviour, 180°C and 100°C are exhibiting (100) type behaviour and 350°C exhibits (111) behaviour. This data largely agrees with the EBSD data.**

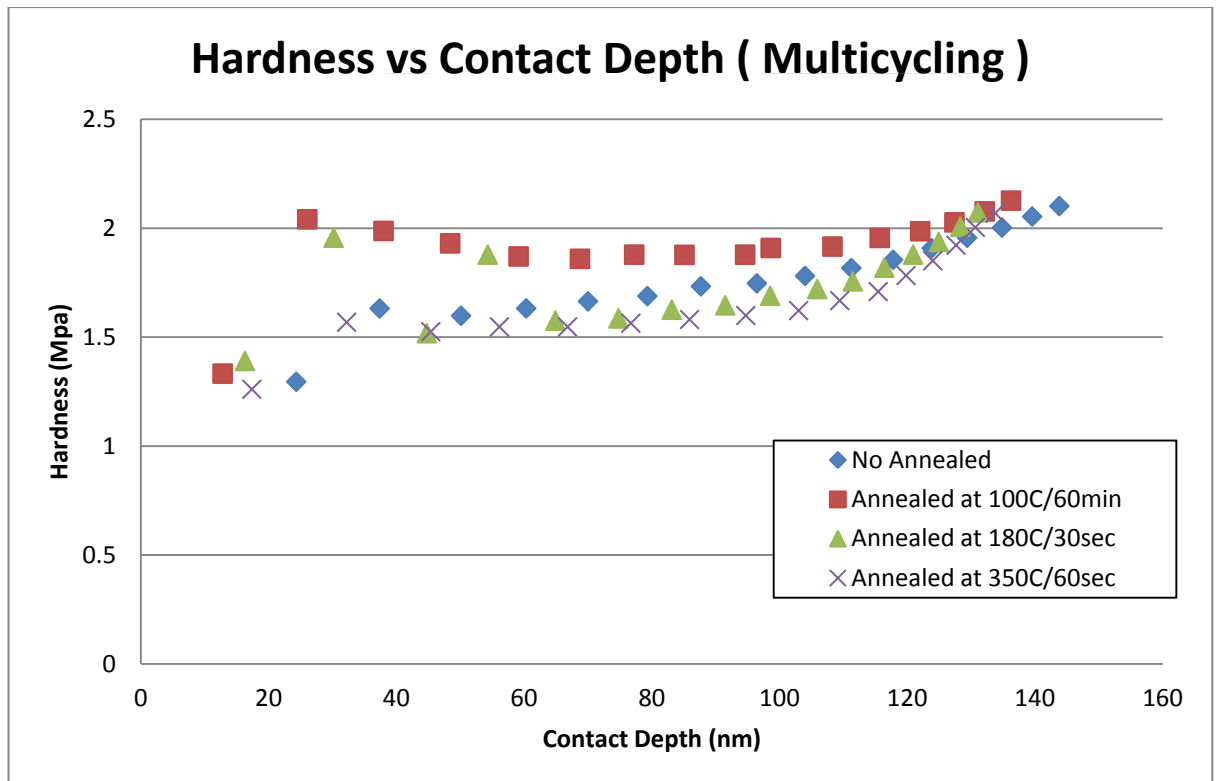


Figure 7.19 Hardness vs. contact depth. 100°C annealed sample displays a higher than expected hardness value likely due to the indent being carried out on a small grain. The hardness values at high contact depths converge due to the effect from pile up.

Figure 7.19 shows the hardness derived for multicycling indentation on the four Cu samples. Aside from initial scatter at very low contact depths, the hardness is relatively constant up until penetration depths above 100 nm. This sudden increase at high contact depth is due to the affect pile up has on the measured result. The data obtained for the 100°C sample is somewhat surprising but highlights a problem with multicycling. It is likely that each multicycling test was carried out an many small grains. As multicycling samples the same spot several times, then larger grains will not have been sampled at all. A method to pick out individual grains to sample would have avoided this. Ideally, using the EBSD data to image the grains then performing nanoindentation in the same area would ensure a large enough sample of grain sizes was investigated.

### 7.3.1. Nanoindentation Discussion

It is essential to know the size of the plastic zone associated with an indentation impression compared to the grain/phase size to understand measured behaviour. To gain representative results, sufficient data from a large enough number of different grains is necessary. This is not achieved with multicycling data, therefore it is necessary to repeat

this test in several areas. The nanoindentation results for elastic modulus largely agree with the EBSD data.

#### **7.4. Summary**

The hardness and Young's modulus values of Cu thin film on Si substrates were measured using EBSD and nanoindentation. With Cu there, it is observed that there is a lot of variation in results depending on microstructure which is not the case with Al.

Having obtained good data, it could be used to predict stress/strain behaviour of individual interconnects. Future work could be completed to fully characterize the pile up effects on mechanical properties. To achieve this, EBSD could be utilised to analyse the texture in the indented areas and around pile up. This would help match the indent data to individual grains. Also, more indents would ensure a larger range of small and large grains would be sampled to eliminate any anomalous data such as that shown in the hardness measurements.

EBSD and nanoindentation have proved to complement each other well and are very powerful microtexture analysis tools. The problems associated with them are highlighted here and potential work for the future based on overcoming these problems outlined. A greater understanding of the behaviour of thin copper films has been achieved which should help analysis of individual interconnects.

The final chapter outlines a summary of the findings in this thesis and makes some remarks on the future.

## **Chapter 8. Conclusions and future remarks**

The introductory chapters to this thesis explain that the demand placed on materials used in semiconductor fabrication have increased massively due to the desire to uphold Moore's law and hence aggressive device scaling. IC manufacturers want more performance out of their chips for the same or less cost to their predecessors and for this to be achievable the performance needs improve with no additional risks of failure.

Despite the many problems inherent in modern microelectronics, the reality is that many of the processing and measurement techniques surveyed in this thesis are already widely employed in industry. For example, Intel Corporation have been using strain engineering in their processors for since approximately 2002 [Intel Corporation, 2011] due to the benefits seen in performance. It is possible to engineer strain in strained silicon very accurately and when a process is in control, there is little need for constant measuring, so long the effect each processing step has on the strain is fully characterised and understood. Generally, a test structure is fabricated onto the silicon wafer and it is this structure that will be measured for strain. Naturally, a large structure will have a somewhat different strain to the channel of an actual device and this will have to be factored into any design plans. Similarly, copper interconnects are quite widespread in the semiconductor industry, and research is ongoing to solve the issues discussed throughout this thesis.

Following the literature review, chapter 4 discusses the importance of careful calibration. Whether measuring at the nanoscale or even micro-scale, it is important to be sure the data obtained is good quality. This often involves a significant amount of effort. Factors such as stage drift, vibration, electrical problems, even temperature can all have a large effect on the accuracy of a measurement. Careful machine set up limits these factors, however, care must still be taken before and during individual measurements, particularly at the nanoscale.

Chapter 5 continues with an investigation aimed at showing what can be achieved using the current industry choice for strain measurement of conventional Raman spectroscopy. Already mentioned is that generally, a test structure is used in an industrial setting that will be much larger than the actual device strained region. However, as devices get smaller, so will this test structure. For full characterisation, it is important to know how strain works along the full length of the channel. The benefits of

sSOI over  $\epsilon$ -Si are discussed in this chapter. Several very careful measurements were taken both along and across 20  $\mu\text{m}$  long, 70 nm wide sSOI stripe to determine whether uniaxial strain had been achieved. This chapter concludes that with careful measurements, it is possible to characterise devices and structures that are much smaller than the laser spot diameter. This shows that conventional Raman spectroscopy is a long way off reaching the end of its useful life.

Chapter 6 contains an evaluation of SERS and TERS. It was found that a large, reproducible enhancement was easily obtainable on single crystal, unstrained silicon. Significant effort was put into achieving a similar enhancement on  $\epsilon$ -Si/SiGe stacks. It is possible to gain a surface selective enhancement of just the strained cap layer or a relative enhancement of the cap layer and the SiGe VS compared to the underlying Si substrate. However, despite several runs of the same procedure, this proved not to be repeatable 100% of the time, if at all. This holds true for both techniques. It is a promising result as it shows enhancement of these layers is possible, however, much work is required in order to optimise the procedure and equipment. What is clear from this chapter is that although a small enhancement is possible, there is no real surface selectivity at present and the effort required to take a simple measurement does not justify the output. Based on the results obtained and literature, the application of this technique in an industrial setting is potentially still several years off.

Chapter 7 concentrates on BEOL processing and Cu interconnects. In situ characterisation of an interconnect is unlikely to be required, with manufacturers reacting to problems such as peeling, blistering, buckling etc as they arise. For this reason, it is imperative there is an understanding of potential problems and of material characteristics before processing, this will make problems less likely to occur and easier to solve if they do. A full characterisation of very thin Cu films including crystal growth and orientation is included in this chapter which paves the way for simulations and understanding how a deep submicron interconnect or via would act in an actual device. This chapter outlines the problems faced with nanoindentation and EBSD and once again highlights the importance of careful measurements.

Strained silicon technology and copper interconnects undoubtedly provide performance enhancement in the face of device scaling limitation and are helping to continue Moore's law. However, without the necessary techniques available to characterise or

measure them, this could have a severe knock on effect on device quality which would ultimately render them unsuitable.

On embarking on this thesis it was hoped that TERS would be emerging as a promising replacement to conventional Raman spectroscopy, providing a quick, easy and efficient method of measuring strain in devices in situ in a processing line. However, several problems encountered have raised more question than were answered. A technique that is seemingly simple when applied to materials such as carbon nanotubes, several types of dye, microbiological applications and even single crystal silicon cannot provide a reliable or surface selective enhancement of  $\epsilon$ -Si/SiGe stacks. However, that is not to say it is not possible, as shown in chapter 6. The next stage of research would be to attempt to answer some of the questions that have arisen.

It is still unclear what causes SERS and TERS enhancements and what makes this surface selective. Detailed research should be undertaken into nanoparticles, formation of these particles on a tip or island film and nanoparticle material. Once this is fully understood, TERS can be optimised for use with strained silicon.

The importance of obtained high quality data is a running theme throughout this thesis. Good Cu thin film data has been obtained and paves the way for predicting stress/strain behaviour of individual interconnects.

Although no major steps forward have been taken throughout this investigation, more understanding of what is required of various measurement techniques has been outlined. Currently, conventional Raman spectroscopy is more than capable of dealing with the demands placed on it in industry. However, TERS is still a promising technique and is likely to gradually improve and overtake Raman spectroscopy as the measurement technique of choice.

## **Appendix I**

Some of the work carried out in this thesis has been presented at conferences and published. The work carried out on sSOI stripes in chapter 5 was presented at The International Conference on Metallurgical Coatings and Thin Films (ICMCTF) in 2009. The work carried out in chapter 7 was presented at the Newcastle Nanoindentation Conference in 2010. This work has subsequently been accepted for published in the Journal of Materials Science and Technology. The title and abstract are below.

The effect of microstructure on the hardness of submicron thin films and nanostructured devices.

S J Bull, L. Sanderson, N. Moharrami and A. Oila

The manufacture of mechanical devices such as MEMS from thin films can lead to circumstances where the scale of the mechanical deformation induced by device operation is comparable to the scale of the microstructure of the materials from which they are made. A similar observation occurs when using indentation tests to assess the hardness of thin films where the plastic zone dimensions may be comparable to the grain size. This paper highlights the effect of grain size, shape and orientation on the indentation response of copper thin films used for semiconductor metallisation. The conditions under which continuum behaviour is observed are discussed and the effect of crystallographic anisotropy on the choice of appropriate design data will be highlighted for copper coatings. The choice of test conditions such as control method and loading protocol required to generate reliable data are also discussed.

## References

- Agdur, B., Boling, G., *et al.* (1963). "Scattering, absorption, and emissions of light by thin metal wires." *Physical Review* 130(3): 996-1001.
- Alam, M. N., Blackman, M. and Pashley, D. W. (1954). "High-angle Kikuchi patterns." *Proceedings of the Royal Society A* 221(1145): 224-242.
- Alexandrov, A., Smirnova L., *et al.* (2005). "UV-initiated growth of gold nanoparticles in PMMA matrix." *Applied Surface Science* 248(1-4): 181-184.
- Anastassakis, E., Pinczuk A., *et al.* (1970). "Effect of static uniaxial-stress on the Raman-spectrum of Silicon" *Solid State Communications* 8: 133-138.
- Anderson, M. S. (2000). "Locally enhanced Raman spectroscopy with an atomic force microscope." *Applied Physics Letters* 76(21): 3130-3132.
- Anderson, M. S. and Pike, W. T. (2002). "A Raman-atomic force microscope for apertureless-near-field spectroscopy and optical trapping." *Review of Scientific Instruments* 73(3): 1198-1203.
- Ashcroft, N. W. and Mermin, N. D. (1988). "Solid State Physics." Saunders College Publishing.
- Becker, M., Sivakov, V., *et al.* (2008). "Nanowires enabling signal-enhanced nanoscale Raman spectroscopy." *Small* 4(4): 398-404.
- Bek, A., De Angelis, F. *et al.* (2011). "Tip enhanced Raman scattering with adiabatic plasmon focusing tips." *Micron* 42: 313-317.
- Berweger, S. and Raschke, M. B. (2009). "Polar phonon mode selection rules in tip-enhanced Raman scattering." *Journal of Raman Spectroscopy* 40(10): 1413-1419.
- Binnig, G., Quate, C. F., *et al.* (1986). "Atomic force microscope." *Physical Review Letters* 56(9): 930-933.
- Bonaccorso, F., Calogero, G., *et al.* (2007). "Fabrication of gold tips by chemical etching in aqua regia." *Review of Scientific Instruments* 78(10).

- Brantley, W. A. (1973). "Calculated elastic-constants for stress problems associated with semiconductor devices." *Journal of Applied Physics* 44(1): 534-535.
- Bridges, W. B., Chester, A. N., Halsted, A. S. and Parker, J. V. (1971). "Ion laser plasmas." *Proceedings of the IEEE* 59(5): 724-737.
- Brown, K. R., Walter, D. G., *et al.* (2000). "Seeding of colloidal Au nanoparticle solutions. 2. Improved control of particle size and shape." *Chemistry of Materials* 12(2): 306-313.
- Cahill, D. G., Watanabe, F., *et al.* (2005). "Thermal conductivity of epitaxial layers of dilute SiGe alloys." *Physical Review B* 71(23).
- Cammarata, R. C. and Sieradzki, K. (1989). "Surface stress effects on the critical film thickness for epitaxy." *Applied Physics Letters* 55(12): 1197-1198.
- Christiansen, S. H., Becker, M., *et al.* (2007). "Signal enhancement in nano-Raman spectroscopy by gold caps on silicon nanowires obtained by vapour-liquid-solid growth." *Nanotechnology* 18(3).
- Collins, L. (2003). "Silicon takes the strain." *IEEE Review* 49(11): 46-49.
- Compton, A. H. (1923). "The Spectrum of Scattered X-Rays." *The Physical Review* 22(5): 409-413.
- Cui, X. D., Zhang, W. H., *et al.* (2007). "Tuning the resonance frequency of Ag-coated dielectric tips." *Optics Express* 15(13): 8309-8316.
- De Wolf, I. (1996). "Micro-Raman spectroscopy to study local mechanical stress in silicon integrated circuits." *Semiconductor Science and Technology* 11: 139-154.
- De Wolf, I. (1999). "Stress measurements in Si microelectronics devices using Raman spectroscopy." *Journal of Raman Spectroscopy* 30(10): 877
- De Wolf, I. (2003). "Raman spectroscopy: about chips and stress." *Spectroscopy Europe* 15(2): 6-13.
- Demming, A. L., Festy, F., *et al.* (2005). "Plasmon resonances on metal tips: Understanding tip-enhanced Raman scattering." *Journal of Chemical Physics* 122(18).

- Diao, J. J., Qiu, F. S., *et al.* (2003). "Surface vertical deposition for gold nanoparticle film." *Journal of Physics D-Applied Physics* 36(3): L25-L27.
- Dietrich, B., Bugiel, E., *et al.* (1993). "Measurement of stress and relaxation in  $\text{Si}_{1-x}\text{Ge}^x$  layers by Raman line shift and x-ray-diffraction." *Journal of Applied Physics* 74(5): 3177-3180.
- Dietrich, B. and Dombrowski, K. F. (1999). "Experimental challenges of stress measurements with resonant micro-Raman spectroscopy." *Journal of Raman Spectroscopy* 30(10): 893-897.
- Dismukes, J. P., Ekstrom, L., and Paff, R. J. (1964). "Lattice parameter and density in germanium-silicon alloys." *The Journal of Physical Chemistry* 68(10): 3021-3027.
- Dobrosz, P. (2006). "Analysis of Strained Si/SiGe Structures by Raman Spectroscopy." School of Chemical Engineering and Advanced Materials. Newcastle upon Tyne, Newcastle University.
- Dodson, B. W. and Tsao, J. Y. (1988). "Non-Newtonian strain relaxation in highly strained SiGe heterostructures." *Applied Physics Letters* 53(25): 2498-2500.
- Dombrowski, K. F., De Wolf, I., *et al.* (1999). "Stress measurements using ultraviolet micro-Raman spectroscopy." *Applied Physics Letters* 75(16): 2450-2451.
- Dombrowski, K. F., Dietrich, B., *et al.* (2001). "Investigation of stress in shallow trench isolation using UV micro-Raman spectroscopy." *Microelectronics Reliability* 41(4): 511-515.
- Edelstein, D., Heidenreich, J., *et al.* (1997). Full copper wiring in a sub-0.25  $\mu\text{m}$  CMOS ULSI technology. New York, Ieee.
- Fischer-Cripps, A. C. (2004). "Nanoindentation", Mechanical Engineering Series, Springer.
- Fleischmann, M., Hendra, P. J. and McQuillan, A. J. (1974). "Raman spectra of pyridine adsorbed at a silver electrode." *Chemical Physics Letters* 26(2): 163-166.

- Georgi, C., Hecker, M., *et al.* (2007). "Raman intensity enhancement in silicon-on-insulator substrates by laser deflection at atomic force microscopy tips and particles." *Applied Physics Letters* 90(17).
- Ghyselen, B., Hartmann, J. M., *et al.* (2004). "Engineering strained silicon on insulator wafers with the Smart Cut (TM) technology." *Solid-State Electronics* 48(8): 1285-1296.
- Glassbrenner, C. J., and Slack, G. A. (1964). "Thermal conductivity of silicon and germanium from 3°K to the melting point." *Physical Review* 134(4): 1058-1069
- Glockler, G. (1943). "The Raman Effect." *Reviews of Modern Physics* 15(2): 111-175.
- Gouadec, G. and Colombari, P. (2007). "Raman spectroscopy of nanostructures and nanosized materials." *Journal of Raman Spectroscopy* 38(6): 598-603.
- Hartschuh, A., Anderson, N., *et al.* (2003). "Near-field Raman spectroscopy using a sharp metal tip." *Journal of Microscopy-Oxford* 210: 234-240.
- Hayazawa, N., Inouye, Y., *et al.* (2000). "Metallized tip amplification of near-field Raman scattering." *Optics Communications* 183(1-4): 333-336.
- Hayazawa, N., Motohashi, M., *et al.* (2007). "Visualization of localized strain of a crystalline thin layer at the nanoscale by tip-enhanced Raman spectroscopy and microscopy." *Journal of Raman Spectroscopy* 38(6): 684-696.
- Hayazawa, N., Motohashi, M., *et al.* (2005). "Highly sensitive strain detection in strained silicon by surface-enhanced Raman spectroscopy." *Applied Physics Letters* 86(26): 263114-263113.
- Hayazawa, N., Saito, Y., *et al.* (2004). "Detection and characterization of longitudinal field for tip-enhanced Raman spectroscopy." *Applied Physics Letters* 85(25): 6239-6241.
- Hecker, M., Zhu, L., *et al.* (2007). "Analytics and Metrology of Strained Silicon Structures by Raman and Nano-Raman Spectroscopy." *AIP Conference Proceedings* 931(1): 435-444.
- Heidenreich, J., Edelstein, D., *et al.* (1998). *Copper dual damascene wiring for sub-0.25 mu m CMOS technology*. New York, Ieee.

- Helseth, L. E. (2005). "Plasma response of nanostructured gradient index materials." *Physics Letters A* 346(1-3): 174-178.
- Himcinschi, C., Radu, I., *et al.* (2006). "Relaxation of strain in patterned strained silicon investigated by UV Raman spectroscopy." *Materials Science and Engineering B-Solid State Materials for Advanced Technology* 135(3): 184-187.
- Hiroaki, H., Nobumitsu, H., *et al.* (2011). "Strain distribution analysis of sputter-formed strained Si by tip-enhanced Raman spectroscopy." *Applied Physics Express* 4(025701): 1-3.
- Horiba Jobin Yvon, [www.horiba.com](http://www.horiba.com), accessed 2007, 2008, 2011
- Hutter, E. and Fendler J. H. (2004). "Exploitation of localized surface plasmon resonance." *Advanced Materials* 16(19): 1685-1706.
- Intel Corporation, [www.intel.com](http://www.intel.com), accessed 2008, 2011
- International Technology Roadmap for Semiconductors, [www.ITRS.net](http://www.ITRS.net), accessed 2011
- Jain, S. C. (2003). "Germanium-silicon strained layers and heterostructures." *Advances in Electronics and Electron Physics*, Supplement 24, Academic Press
- Kacher, J., Landon, C., *et al.* (2009). "Bragg's Law diffraction simulations for electron backscatter diffraction analysis." *Ultramicroscopy* 109(9): 1148-1156.
- Kaiser Optical Systems, [www.kosi.com](http://www.kosi.com), accessed 2007
- Kasper, E. (1995) "Properties of Strained and Relaxed Silicon Germanium." *EMIS Datareviews Series*, Institute of Engineering and Technology
- Keller, R. R., Roshko, A., *et al.* (2004). "EBSD measurement of strains in GaAs due to oxidation of buried AlGaAs layers." *Microelectronic Engineering* 75(1): 96-102.
- Kittel, C. (2005). "introduction to solid state physics." Wiley
- Klar, T., Perner, M., *et al.* (1998). "Surface-plasmon resonances in single metallic nanoparticles." *Physical Review Letters* 80(19): 4249-4252.
- Kneipp, K., Wang, Y., *et al.* (1997). "Single molecule detection using surface-enhanced Raman scattering (SERS)." *Physical Review Letters* 78(9): 1667-1670.

- Krishnan, R. S. (1971). "Historical Introduction." in "The Raman Effect." A. Anderson, Dekker, Inc. Volume 1: Principles.
- Langer, E. and Dabritz S. (2007). Investigation of HOLZ rings in EBSD patterns. *Physica Status Solidi C - Current Topics in Solid State Physics*, 4(6):1867-1872.
- Leff, D. V., Ohara, P. C., *et al.* (1995). "Thermodynamic control of gold nanocrystal size – experiment and theory." *Journal of Physical Chemistry* 99(18): 7036-7041.
- LeGoues, F. K., Copel, M., *et al.* (1989). "Novel strain-induced defect in thin molecular-beam-epitaxy layers." *Physical Review Letters* 63(17): 1826-1829.
- Masuda-Jundo, K., Hung, V. V. and Menon, M. (2009) "Fracture and mechanical properties of nanotubes and nanowires" *Procedia Engineering* 1(1): 163-166
- Martin, O. J. F. and Girard C. (1997). "Controlling and tuning strong optical field gradients at a local probe microscope tip apex." *Applied Physics Letters* 70(6): 705-707.
- Merlen, A., Valmalette, J. C., *et al.* (2009). "Depolarization effects in tip-enhanced Raman spectroscopy." *Journal of Raman Spectroscopy* 40(10): 1361-1370.
- Micic, M., Klymyshyn, N., *et al.* (2003). "Finite element method simulation of the field distribution for AFM tip-enhanced surface-enhanced Raman scanning microscopy." *Journal of Physical Chemistry B* 107(7): 1574-1584.
- Millstone, J. E., Park, S., *et al.* (2005). "Observation of a quadrupole plasmon mode for a colloidal solution of gold nanoprisms." *Journal of the American Chemical Society* 127(15): 5312-5313.
- Milner, R. G. and Richards D. (2001). "The role of tip plasmons in near-field Raman microscopy." *Journal of Microscopy* 202(1): 66-71.
- Mistry, K., Armstrong, M., *et al.* (2004). "Delaying forever: uniaxial strained silicon transistors in 90nm CMOS technology." *VLSI Symposium Technical Digest* 50-51
- Moore, G. E. (1965). "Cramming more components onto integrated circuits (Reprinted from *Electronics*, pg 114-117, April 19, 1965)."
- Moskovits, M. (1985). "Surface-enhanced spectroscopy." *Reviews of Modern Physics* 57(3): 783-826.

- Oliver, W. C. and Pharr, G. M. (1992). "An improved technique for determining hardness and elastic modulus using load and displacement sensing indentation experiments." *Journal of Materials Research* 7(6): 1564-1583.
- Oliver, W. C. and Pharr, G. M. (2004). "Measurement of hardness and elastic modulus by instrumented indentation: Advances in understanding and refinements to methodology." *Journal of Materials Research* 19(1): 3-20
- Olsen, S. H., O'Neill, A. G., *et al.* (2005). "Study of strain relaxation in Si/SiGe metal-oxide-semiconductor field-effect transistors." *Journal of Applied Physics* 97(11).
- O'Neill, A. G., Olsen, S. H., *et al.* (2006). "Strained Silicon Technology." 8th International Conference on Solid-State and Integrated Circuit Technology, 2006: 104 - 107
- Pendry, J. B., Holden, A. J., *et al.* (1996). "Extremely Low Frequency Plasmons in Metallic Mesostructures." *Physical Review Letters* 76(25): 4773.
- Pettinger, B., Tadjeddine, A. and Kolb, D.M. (1979). "Enhancement in Raman intensity by use of surface plasmons." *Chemical Physics Letters* 66(3): 544-548.
- Pettinger, B., Ren, B., *et al.* (2004). "Nanoscale probing of adsorbed species by tip-enhanced Raman spectroscopy." *Physical Review Letters* 92(9).
- Poborchii, V., Tada, T., *et al.* (2005). "Subwavelength-Resolution Raman Microscopy of Si Structures Using Metal-Particle-Topped AFM Probe." *Japanese Journal of Applied Physics* 44: 202-204.
- Poborchii, V., Tada, T., *et al.* (2009). "Optimization of tip material and shape for near-UV TERS in Si structures." *Journal of Raman Spectroscopy* 40(10): 1377-1385.
- Puppels, G. J., A. Huizinga, *et al.* (1990). "A high-throughput Raman notch filter set." *Review of Scientific Instruments* 61(12): 3709-3712.
- Raman, C. V. (1929). "The Raman Effect." *Transcripts of the Faraday Society* 25: 781-792.
- Raman, C. V. and K. S. Krishnan K. S. (1928). "A new type of secondary radiation" *Nature* 121:501-502

- Randle, V. (2008). "Microtexture determination and its applications." Second Edition, Institute of Materials, Minerals and Mining, Maney Publishing
- Rath, S., Hsieh, M., L., *et al.* (2003). "Alloy effects on the Raman spectra of  $\text{Si}_{1-x}\text{Ge}_x$  and calibration protocols for alloy compositions based on polarization measurements." *Semiconductor Science and Technology* 18(6): 566-575.
- Reiche, M., Moutanabbar, O., *et al.* "Strained silicon on wafer level by wafer bonding: materials processing, strain measurements and strain relaxation." *ECS Transaction* 16(8): 311-320
- Reiche, M., Moutanabbir, O., *et al.* (2010). "Strained Silicon Devices." *Solid State Phenomena* 156: 61-68.
- Ren, B., G., *et al.* (2004). "Preparation of gold tips suitable for tip-enhanced Raman spectroscopy and light emission by electrochemical etching." *Review of Scientific Instruments* 75(4): 837-841.
- Rim, K. and Shi, L. (2002). "Strained-Si for sub-100-nm MOSFETs" *VLSI Symposium Technical Digest* 98-99
- Saito, Y., Motohashi, M., *et al.* (2008). "Stress imaging of semiconductor surface by tip-enhanced Raman spectroscopy." *Journal of Microscopy-Oxford* 229(2): 217-222.
- Semwogerere, D. and Weeks, E. R. (2005). "Confocal Microscopy." Retrieved April, 2008.
- Sheppard, C. J. R. and Shotton D. M. (1997). "Confocal Laser Scanning Microscopy", Bios Scientific Publishers.
- Shevchenko, E. V., Talapin, D. V., *et al.* (2006). "Structural diversity in binary nanoparticle superlattices." *Nature* 439(7072): 55-59.
- Shifren, L., Wang, X., *et al.* (2004). "Drive current enhancement in p-type metal-oxide-semiconductor field-effect transistors under shear uniaxial stress." *Applied Physics Letters* 85(25): 6188-6190.
- Schwartz, A. J., Kumar, M., and Adams, B. L. (2000) "Electron backscatter diffraction in materials science." (2000) Springer

Shwartz, G. C. (2006). "Handbook of Semiconductor Interconnection Tehcnology", Taylor and Francis Group.

Smith, E. and Dent G. (2005). "Modern Raman Spectroscopy A Practical Approach." Wiley.

Stanford "<http://www.stanford.edu/group/snl/SEM/OIMIntro.htm>" accessed 2012

Stockle, R. M., Suh, Y. D., *et al.* (2000). "Nanoscale chemical analysis by tip-enhanced Raman spectroscopy." *Chemical Physics Letters* 318(1-3): 131-136.

Tachibana, Y., Kusunoki, K., *et al.* (2003). "Optical properties of multilayers composed of silver and dielectric materials." *Thin Solid Films* 442(1-2): 212-216.

Tarun, A., Hayazawa, N., *et al.* (2008). "Highly efficient tip-enhanced Raman spectroscopy and microscopy of strained silicon." *Review of Scientific Instruments* 79(1).

Tarun, A., Hayazawa, N. and Kawata, A. (2009). "Tip-enhanced Raman spectroscopy for nanoscale strain characterization." *Anal. Bioanal. Chem.* 394: 1775-1785.

Teal, G. K. (1976). "Single-crystals of germanium and silicon – basic to transistor and integrated circuit." *IEEE Transactions on Electron Devices* 23(7): 621-639.

Telford, M. (2004). "Stretching silicon's lifespan." *III-Vs Review: The Advanced Semiconductor Magazine* 17(7): 36-39.

Thompson, S. E., Sun, G., *et al.* (2006). "Uniaxial process induced strained-Si: extending the CMOS roadmap." *IEEE Transactions on Electronic Devices* 53(5); 1010-1020.

Tian, Z. Q., Ren, B., *et al.* (2002). "Surface-enhanced Raman scattering: From noble to transition metals and from rough surfaces to ordered nanostructures." *Journal of Physical Chemistry B* 106(37): 9463-9483.

Tobin, M. C. (1971). "Laser Raman Spectroscopy." Wiley-Interscience.

Vereecken, P. M., Binstead, R. A., *et al.* (2005) "The chemistry of additives and damascene copper plating" *IBM Journal of Reseach and Development* 49(1): 3-18

- Wang, Z. G., Cai, X., *et al.* (2006). "Optical properties of metal-dielectric multilayers in the near UV region." *Vacuum* 80(5): 438-443.
- Webster, S., Batchelder, D. N., *et al.* (1998). "Submicron resolution measurement of stress in silicon by near-field Raman spectroscopy." *Applied Physics Letters* 72(12): 1478-1480.
- Wilkinson, A. J., Meaden, G., *et al.* (2006). "High resolution mapping of strains and rotations using electron backscatter diffraction." *Materials Science and Technology* 22(11): 1271-1278.
- Wilson, C. J. (2009). "Stress Measurements in Deep Submicron Damascene Copper Interconnects." School of Electrical, Electronic and Computer Engineering, Newcastle University, Newcastle upon Tyne.
- Wolf, S. And Tauber, R. N. (2000). "Silicon processing for the VLSI era: Volume 1 Process technology." Second edition, Lattice Press
- Woodward, L. A. (1967). "General Introduction." in "Raman Spectroscopy Theory and Practice." H. A. Szymanski. New York, Plenum Press.
- Yeo, B.-S., Zhang, W., *et al.* (2006). "Enhancement of Raman Signals with Silver-Coated Tips." *Applied Spectroscopy* 60: 1142-1147.
- Zayats, A. V. and Smolyaninov, I. I. (2003). "Near-field photonics: surface plasmon polaritons and localized surface plasmons." *Journal of Optics a-Pure and Applied Optics* 5(4): S16-S50.
- Zhao, B., Biberger, M. A., *et al.* (1997). "Low temperature and low cost planarised aluminium interconnect for sub-half micrometre VLSI circuits." *Electronics Letters* 33(3): 247-248.